Stress- and Deformation Analysis of a Spanner

Group 54b
7th Semester 2009

Mariann Nørgaard Vestergaard
Brian Frydensberg Damgaard
Preben Hannås Haarde
René Sørensen
Jesper Kann

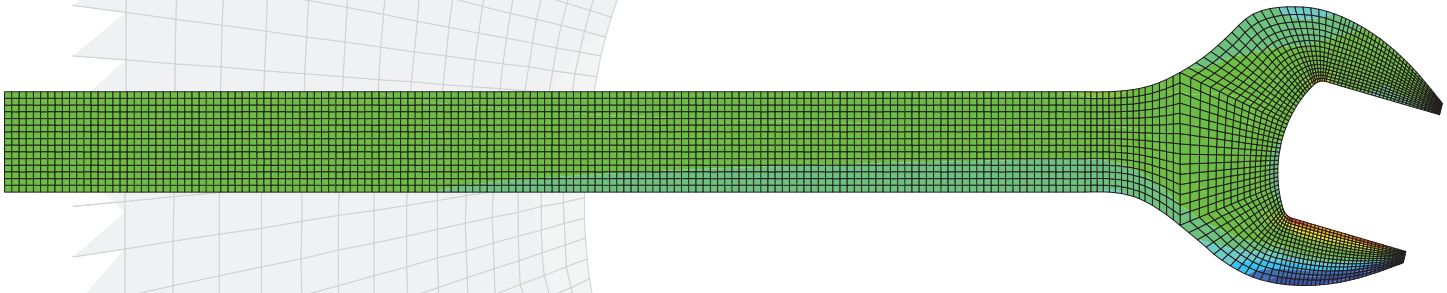

Aalborg University
Departement of Mechanical Engineering

Aalborg University
Department of Mechanical Engineering
Pontoppidanstræde 105
9220 Aalborg Ø
Tel (+45) 9940 9300
Fax (+45) 9815 1675
http://www.me.aau.dk/

Title:

Stress- and Deformation Analysis of a Spanner

Semester theme:

Stress- and deformation analysis of a force transmitting structure

Project period:

The M-sector's 7th semester
September 2nd 2009
– December 18th 2009

Project Group:

54b

Participants:

Mariann Nørgaard Vestergaard
René Sørensen
Brian Frydensberg Damgaard
Preben Hannås Haarde
Jesper Kann

Supervisor:

Jens Andreasen

Copies: 7

Number of Pages: 126

Abstract:

The main focus of this report is to determine the stress and deformations occurring in a loaded spanner. In order to analyse the spanner in detail a model is made where the geometry is simplified to a plane model. Through a design process a new design is sought which meet requirements regarding deformation and geometry. Here four different methods is applied to determine the strains in the spanner model which is subjected to a load of $100N$. These are, estimate calculations, measurements, and a developed finite element program. The estimate calculations consist of classic Bernoulli-Euler beam theory and methods with known solutions from the theory of elasticity. The measurements are performed with the use of strain gauges and digital image correlation. The developed finite element model uses isoparametric Q4 elements with reduced integration and hourglass control. Comparing the results from the finite element model with the measurements reveals a deviation of 12 %. By use of the developed program an intuitive optimisation is conducted with focus on reducing the used amount of material while also satisfying a set of design and load requirements. The result of a new geometric design is that the volume is reduced by 10 % while increasing the strength of the model. In order to meet the load requirements the volume is expanded by 55 % through increasing the thickness. The final result is thus a better geometric design which meets both the design and load requirements.

Mariann Nørgaard Vestergaard

Preben Hannås Haarde

René Sørensen

Jesper Kann

Brian Frydensberg Damgaard

Preface

This report has been composed by Group 54b on the 7th semester of Design of Mechanical Systems at Aalborg University. It presents a comprehensive stress- and deformation analysis of a spanner resulting in an optimisation of the examined subject. The project title is:

Stress- and Deformation Analysis of a Spanner

The project is documented by this main report, an appendix, and a subjoined CD-ROM. The report can be read independently, however, additional supporting information is located in the appendix.
The CD-ROM is located in appendix C and contains the following items:

- A maple-file for determining the stiffness of a frame from the experimental setup.
- Recorded data from strain gauge measurements
- The developed FEA-program DMS7FEA with source-code.
- SolidWorks CAD files for produced parts.
- MatLab routines used for different calculations.
- A copy of this report in PDF format.

Citations are done in accordance with the Vancouver Style in square brackets with references numbered in order of appearance: e.g. [1] or [2, p. 5] for specific page numbers. The numbers refer to the bibliography in the back of the report where information about the sources is found.

Figures and equations are numbered according to the chapter in which they are presented—for instance: *figure 1.2* is the 2nd figure in chapter 1.

Appendices are labeled with capital letters followed by a section number—for instance: *A.1* is the 1st section in appendix A.

The applied gravitational acceleration is: $9.81 m/s^2$.

The following mathematical notation is used throughout the text:

Vectors:	$\vec{q}$
Matrices:	$\bar{\bar{D}}$

Contents

Chapter

1

Introduction

This project treats subjects regarding *Stress- and deformation analysis of a force transmitting structure*. The focus is on using different analytic and experimental methods to determine the stress, strain and displacement conditions in an element subjected to a loading situation. The analytic methods range from classic *Bernoulli-Euler* beam theory and parts from the *Theory of Elasticity* to discrete approximated computer based *Finite Element Analysis*. The associated experimental methods include *Strain Gauge* measurements and the recent commercially available *Digital Image Correlation*(DIC) technology. The results from the different analytical and experimental methods will be compared in order to discover any limitations within each method. This requires that the geometry and loading conditions can be reduced to a plane two dimensional model since less complexity gives more accurate results for the analytical methods. Due to this a spanner has been chosen as subject of analysis because a two dimensional model can be made with minor adjustments. When the stress, strain and displacement conditions of the model have been determined, the model will be optimized so that the least amount of material is used without loss of functionality. The chosen spanner is shown in figure 1.1.

Figure 1.1: *The selected spanner.*

The initial issue for the study is:

How is a spanner designed to satisfy the everyday use so as a practical geometry and sufficient strength is obtained?

Chapter

2

Model Design

To accomodate the demands of everyday use of a spanner, requirements for the geometry and loading are sought by use of the standard DIN 3113 [1]. In order to compare the results from the different analytical calculations and experiments, the geometry of the spanner is reduced to a plane two dimensional model. These simplifications of geometry and load conditions are described in the following.

2.1 Geometry Simplification

The size of the selected spanner is M16, and it is certified according to DIN 3113 [1, p. 160]. The DIN certification ensures that the spanner fulfills some geometrical demands and tolerances. The selected spanner is seen in figure 2.1, and the associated measurements and tolerances are listed in table 2.1.

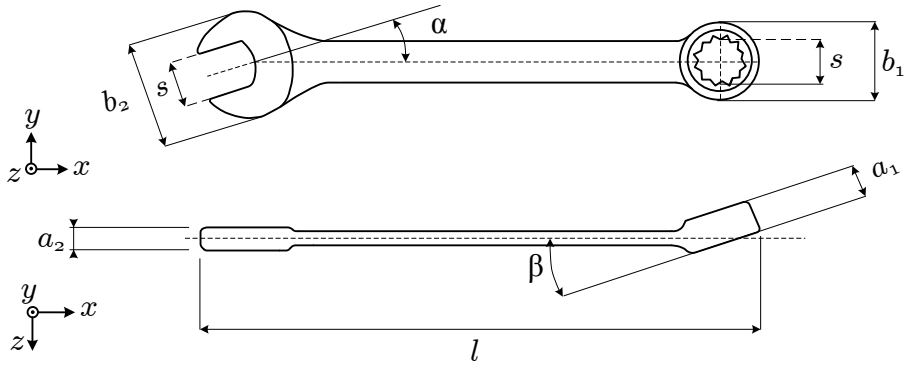

Figure 2.1: *The dimensions of the selected spanner which are prescribed by DIN 894.*

$s\,/mm$	$l\,/mm$	β	α	$a_1\,/mm$	$a_2\,/mm$	$b_1\,/mm$	$b_2\,/mm$
24,06-24,36	min. 265	$10° - 15°$	15°	max. 16	max. 12	max. 38	max. 56

Table 2.1: *Dimensions for a M16 spanner cf. DIN 3113 [1, pp. 157–164], tolerances according to DIN ISO 691 [1, pp. 483–487].*

As seen in figure 2.1, the spanner has got two different ends. One end is an open fork while the other is a closed ring with polygenic inner grip. It can also be seen that the ring end is tilted at an angle β out of the xy-plane, and that the spanner has a non uniform thickness.

The simplified model is shown in figure 2.2, along with the measurements in table 2.2.

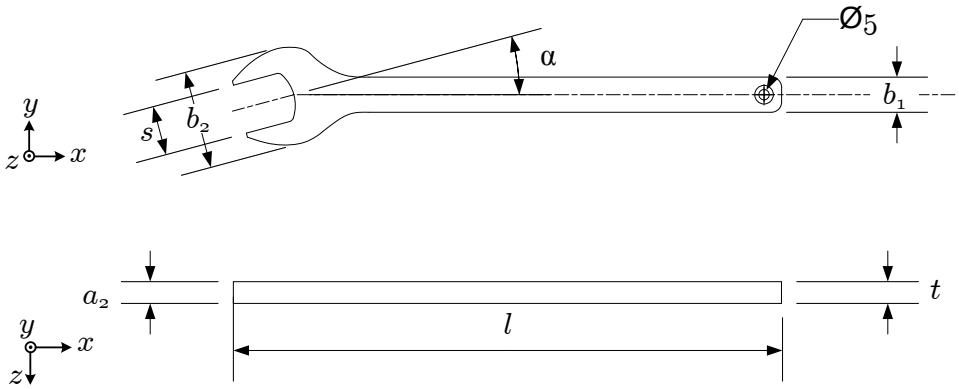

Figure 2.2: *The simplified spanner model has alternated shape and dimensions.*

s / mm	l / mm	α	a_1 / mm	t / mm	b_1 / mm	b_2 / mm
24	265,5	15°	5	5	17	47,1

Table 2.2: *Dimensions of the model.*

As seen in table 2.2 the dimensions of the DIN norm is preserved in the model. The outer contour of the model has been made similar to that of the original spanner. The model has been made with uniform thickness which simplifies the computational analysis. Sharp edges have also been introduced so that it is possible to mount strain gauges on all surfaces. The ring end has been removed so that the whole structure is in plane. This also simplifies the analysis because the loading situation can be defined more accurate in the fork end. The thickness and material of the model have been chosen from available plate material. The material is a ferris steel and the material properties are determined through a tensile test described in section 8.3.

2.2 Load Simplification

The purpose of a spanner is to tighten bolts and nuts. When tightening nuts and bolts the hand will apply a non uniform distributed load, $F(x)$, to the handle of the spanner. This is illustrated in figure 2.3.

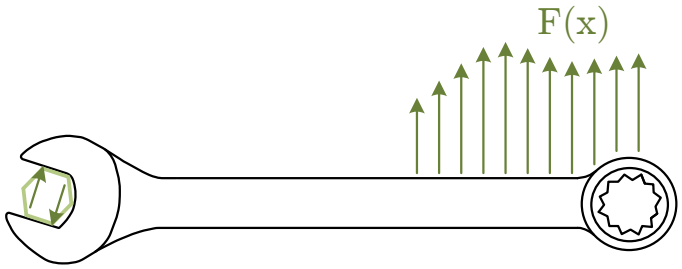

Figure 2.3: *The load distribution will vary upon use.*

The load situation will depend on who and how it is used. In order to do general comparisons, it is important that the loads are well defined and acts in the same way for both the analysis and the different experiments. Because of this the load conditions from the DIN norm have

been chosen for the further work. According to DIN 3113 the spanner must be able to withstand a static torque of minimum 287 Nm without structural deformation resulting in loss of functionality. The applied force resulting in the torque must act perpendicular to the length of the spanner cf. DIN ISO 1711 [1, pp. 495–504]. A pin hole has been made which the test force can be applied through. To ensure that the force is applied in-plane, the pin hole has been chamfered to produce a small contact surface in the centre plane of the spanner. This is shown in figure 2.2.

Chapter

3

Thesis Statement

A spanner design which meets the following requirements is to be designed.

A DIN certified M16 spanner must be able to withstand a static torque of minimum 287 Nm without structural deformation resulting in loss of functionality. The limit where the spanner has a loss of functionality is interpreted as deformation characterised by the following:

- The distance between the jaws two centre points, S_d, exceeds the tolerance limit of 24,36 mm.
- The angel α between the shank and fork centerlines changes more than 1°.

The above situations are illustrated in figure 3.1. In section 2.1 it was stated that a DIN certified

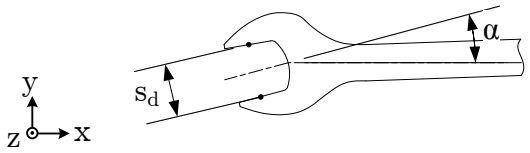

Figure 3.1: *The spanner design must fulfill the given demands for deformation.*

M16 spanner must satisfy a set of design requirements. These must equally be met by the final design. The model is shown in figure 2.2 and the dimensions are repeated in table 3.1.

$s\,/mm$	$l\,/mm$	α	$a_2\,/mm$	$b_1\,/mm$	$b_2\,/mm$
24,06-24,36	min. 265	15°	max. 12	max. 38	max. 56

Table 3.1: *The dimension requirements for the final model.*

The final spanner design must satisfy the above requirements. When the stress and strain condition in the spanner model has been determined an intuitive optimisation of the design is performed to meet the requirements with focus on reducing the used amount of material.

Chapter

4

Design Process

The following chapter consists of a brief presentation of how the design process is implemented in the project. The purpose is to illustrate how the different analytic methods used in the optimisation to ensure that so as a new design meets the requirements from the thesis statement.

4.1 Analysis of Design Process

In figure 4.1 a diagram of the design process is shown. The process consists of three main parts, each performing different tasks.
First part represents the design requirements such as the static torque demand, geometric boundary conditions and optimisation parameters. These requirements form the basis of the design, and must be met in the final design proposal. After the design requirements have been formulated the design analysis can begin on the basis of the old design.

The design analysis consists of three subparts each contributing to the remaining two. The first step is calculating estimated stresses in the old design. These calculations are based on the classic Bernoulli Euler beam theory, and parts from the theory of elasticity.

The results from the calculations are then used as a basis for planning measurements and verifying the results. In the project two techniques are used for measuring strains in the spanner, strain gauges and DIC. If there is a close accordance between the two it is reasonable to believe that the results are credible and can be used in the further analysis.

In the third step of the design analysis, the stress conditions are calculated using the finite element method. If the results from the FE model are close to both the measured and calculated values, then it is reasonable to believe that the model is credible. When the model is verified stresses in more complicated geometric parts of the spanner can be estimated and the optimisation process can begin. Once the design requirements have been met the final design is approved.

In the following chapters the above steps in the design process are shown. First the stresses in the spanner are calculated using beam and elasticity theory. Next the results from measurements are presented, and the uncertainties associated with these. Afterwards the finite element analysis program is presented and verified using results from the previous measurements and calculations. Finally the optimised spanner design is verified according to the previously stated requirements using the FE model.

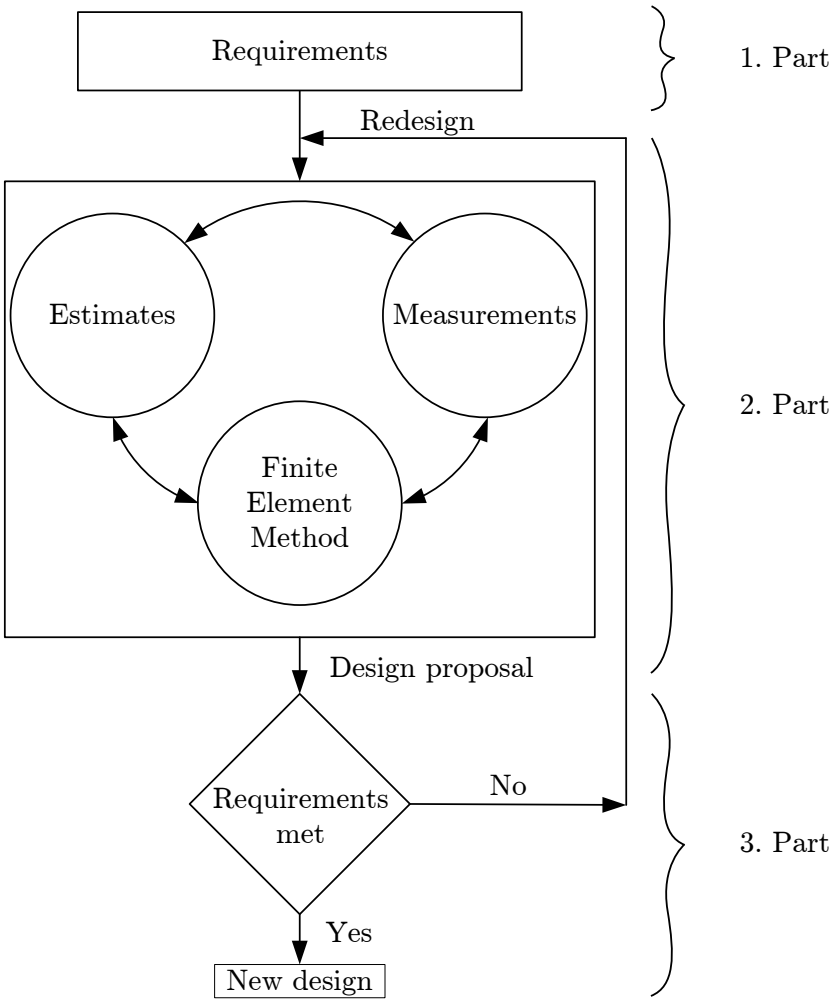

Figure 4.1: *Design diagram for optimisation process.*

Chapter

5

Theory of Elasticity

In order to determine the strains within the spanner due to the subjected loads, a general understanding of the theory of elasticity is required. Due to this requirement, selected topics of the theory of elasticity are derived in the following chapter. The main focus is on determining strains, stresses, and constitutive relations between the two.

In order to reduce the number of mathematical expressions, *Einstein's* index notation is applied throughout the chapter. Here each index refer to a specific coordinate axis in a Cartesian coordinate system, using directions $(X_1, X_2, X_3) \equiv (X, Y, Z)$. The applied theory is mostly based on Kildegaard and Stegmann [2]. The use of other sources are described in the concerned section.

5.1 Strain Condition

In the following Lagrange's strain tensor is derived on the basis of point deformation within a continuum body. Then an interpretation of the elements within the strain tensor is given. Finally Cauchy's strain tensor is introduced.

When a continuous body undergoes a deformation the location of a given point P at x_i changes to P^* at x_i^* in the deformed state. The situation is show in figure 5.1. The displacement from P to P^* is described by the vector v_i which is given by:

$$v_i = x_i^* - x_i \tag{5.1}$$

Considering a line segment composed by two nearby points in the undeformed body P and Q as shown in figure 5.2 the location of Q is given by $x_i + dx_i$ and thus $\overrightarrow{PQ}$ as:

$$\overrightarrow{PQ} = (x_i + dx_i) - x_i \tag{5.2}$$

$$= dx_i \tag{5.3}$$

The distance ds between the two points is described by:

$$ds^2 = dx_i dx_i = dx_1 dx_1 + dx_2 dx_2 + dx_3 dx_3 \tag{5.4}$$

When the body has undergone a deformation, the location of the two points change to P^* and Q^*, where the vector $\overrightarrow{P^*Q^*}$ is given by:

$$\overrightarrow{P^*Q^*} = (x_i^* + dx_i^*) - x_i^* \tag{5.5}$$

$$= dx_i^* \tag{5.6}$$

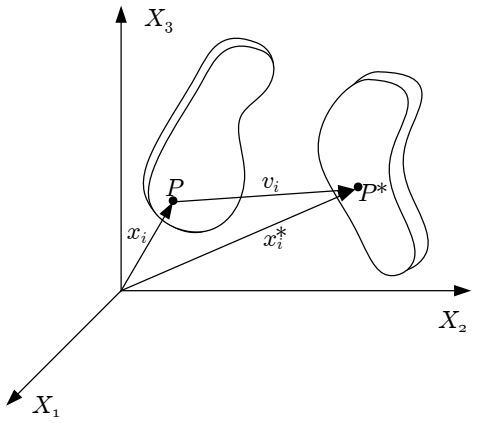

Figure 5.1: *Deformation of a body*

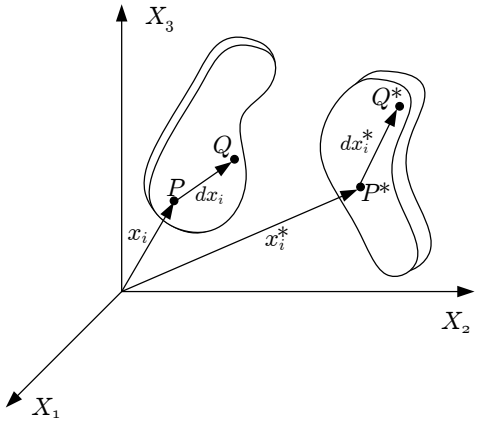

Figure 5.2: *Deformation of a line segment*

The distance ds^* between the two points in the deformed body is described as:

$$(ds^*)^2 = dx_i^* dx_i^* \tag{5.7}$$

The location of the deformed points described by x_i^* is a function of the original positions x_i so as:

$$x_i^* = x_i^*(x_1, x_2, x_3) \tag{5.8}$$

Taking the derivative of x_i^* with respect to x_j leads to the following expression for dx_i^*:

$$\frac{dx_i^*}{dx_j} = \frac{\partial x_i^*}{\partial x_k}\frac{dx_k}{dx_j} \tag{5.9}$$

$$dx_i^* = \frac{\partial x_i^*}{\partial x_k} dx_k \tag{5.10}$$

Substituting the above expression into (5.7) leads to:

$$(ds^*)^2 = dx_i^* dx_i^* \tag{5.11}$$

$$= x_{i,j}^* dx_j x_{i,k}^* dx_k \tag{5.12}$$

$$= x_{k,j}^* dx_j x_{k,i}^* dx_i \tag{5.13}$$

Subtraction of (5.4) from (5.13), gives a measurement of how much the distance between the points P and Q has changed due to the deformation of the body. That is:

$$(ds^*)^2 - ds^2 = x_{k,j}^* dx_j x_{k,i}^* dx_i - dx_i dx_i \tag{5.14}$$

$$= x_{k,j}^* x_{k,i}^* dx_i dx_j - dx_i dx_i \tag{5.15}$$

$$= \left(x_{k,j}^* x_{k,i}^* - \delta_{ij}\right) dx_i dx_j \tag{5.16}$$

Instead of using the coordinates to describe the change in distance between the points P and Q, the displacement vector v_k can be used:

$$v_k = x_k^* - x_k \qquad \Rightarrow \tag{5.17}$$

$$x_k^* = v_k + x_k \tag{5.18}$$

Taking the partial derivative of expression (5.18) with respect to x_i leads to:

$$x^*_{k,i} = v_{k,i} + x_{k,i} \tag{5.19}$$
$$= v_{k,i} + \delta_{ki} \tag{5.20}$$

Substituting the above expression into (5.16) changes the description from coordinates to the displacement vector v_k:

$$(ds^*)^2 - ds^2 = \left(\left(v_{k,j} + \delta_{kj}\right)\left(v_{k,i} + \delta_{ki}\right) - \delta_{ij}\right) dx_i dx_j \tag{5.21}$$
$$= \left(v_{k,j}v_{k,i} + v_{k,j}\delta_{ki} + v_{k,i}\delta_{kj} + \delta_{kj}\delta_{ki} - \delta_{ij}\right) dx_i dx_j \tag{5.22}$$
$$= \left(v_{k,j}v_{k,i} + v_{i,j} + v_{j,i} + \delta_{ij} - \delta_{ij}\right) dx_i dx_j \tag{5.23}$$
$$= \left(v_{k,j}v_{k,i} + v_{i,j} + v_{j,i}\right) dx_i dx_j \tag{5.24}$$
$$= 2\varepsilon_{ij} dx_i dx_j \tag{5.25}$$

The quantity ε_{ij}, shown in (5.25), is called *Lagrange's strain tensor* and is reproduced in explicit form below:

$$\varepsilon_{ij} = \frac{1}{2}\left(v_{k,j}v_{k,i} + v_{i,j} + v_{j,i}\right) \tag{5.26}$$

The strain tensor is of the second order and includes nine elements as shown below:

$$\varepsilon_{ij} = \begin{pmatrix} \varepsilon_{11} & \varepsilon_{12} & \varepsilon_{13} \\ \varepsilon_{21} & \varepsilon_{22} & \varepsilon_{23} \\ \varepsilon_{31} & \varepsilon_{32} & \varepsilon_{33} \end{pmatrix} \tag{5.27}$$

Switching indices i and j in (5.26) reveals that only six of the nine elements are independent due to symmetry as shown below:

$$\varepsilon_{ij} = \frac{1}{2}\left(v_{k,i}v_{k,j} + v_{j,i} + v_{i,j}\right) \tag{5.28}$$
$$\varepsilon_{ji} = \frac{1}{2}\left(v_{k,j}v_{k,i} + v_{i,j} + v_{j,i}\right) \tag{5.29}$$
$$\varepsilon_{ij} = \varepsilon_{ji} \tag{5.30}$$

Thus showing that the following components are equal:

$$\varepsilon_{12} = \varepsilon_{21} \tag{5.31}$$
$$\varepsilon_{23} = \varepsilon_{32} \tag{5.32}$$
$$\varepsilon_{13} = \varepsilon_{31} \tag{5.33}$$

5.1.1 Strain Interpretation

To obtain a better understanding of the physical meaning of Lagrange's strain tensor expression (5.25) is rewritten. The vector between points P and Q, dx_i, can be expressed as $dx_i = n_i ds$:

$$(ds^*)^2 - ds^2 = 2\varepsilon_{ij} dx_i dx_j \quad \Rightarrow \tag{5.34}$$
$$(ds^*)^2 - ds^2 = 2\varepsilon_{ij} n_i n_j ds^2 \quad \Rightarrow \tag{5.35}$$
$$\frac{(ds^*)^2 - ds^2}{2ds^2} = \varepsilon_{ij} n_i n_j \tag{5.36}$$

where: n_i ith component of the unit normal vector n.

n_j jth component of the unit normal vector n.

ds Length of vector dx_i in the undeformed body.

ds^* Length of vector dx_i^* in the deformed body.

Assuming that the line segment only undergoes small deformations, $ds^* \approx ds$, then the left side of expression (5.36) can be rewritten to:

$$\frac{(ds^*)^2 - ds^2}{2ds^2} = \frac{(ds^* + ds)(ds^* - ds)}{2ds^2} \approx \frac{2ds(ds^* - ds)}{2ds^2} = \frac{ds^* - ds}{ds} \tag{5.37}$$

With the assumption that the body only undergoes small deformations the following expression describes the strain of a given line segment in the direction of the unit normal vector n_i:

$$\frac{ds^* - ds}{ds} = \varepsilon_{ij} n_i n_j \tag{5.38}$$

$$\varepsilon = \varepsilon_{ij} n_i n_j \tag{5.39}$$

where: ε Strain on surface perpendicular to direction i and in the direction of j.

Components of the strain tensor with equal indices, $i = j$, are parallel to the X_i axis. These only contribute to volumetric changes of the body, whereas the mixed components, $i \neq j$, are a measure of angular changes between planes within the body. Figure 5.3 shows a body before and after a deformation has occurred. Initially the two line segments $\overrightarrow{PM}$ and $\overrightarrow{PN}$ are at right angles. This angle changes as the two line segments change position due to the deformation. As a consequence the deformed orientation of the line segment is a function of the original alignment, which for $\overset{m}{dx}_i^*$ and $\overset{n}{dx}_i^*$ is expressed below respectively:

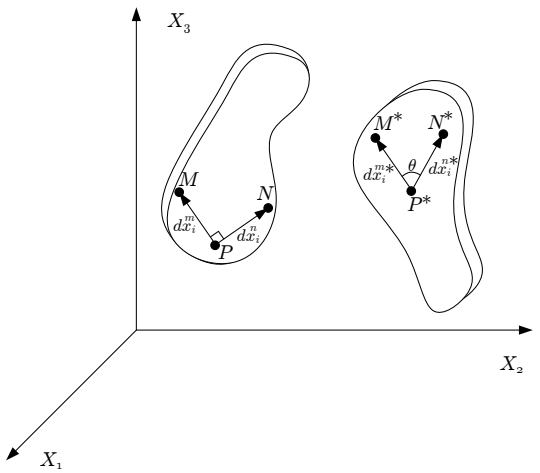

Figure 5.3: *Angular displacement of a plane within a body.*

$$\overrightarrow{P^*M^*} = \overset{m}{dx}_i^* = \overset{m}{dx}_i^* \ (x_1, x_2, x_3) \tag{5.40}$$

$$\overrightarrow{P^*N^*} = \overset{n}{dx}_i^* = \overset{n}{dx}_i^* \ (x_1, x_2, x_3) \tag{5.41}$$

Taking the derivative of $\overset{m}{dx}_i^*$ with respect to $\overset{m}{dx}_j$, and using the chain rule leads to the following:

$$\frac{\overset{m}{dx}_i^*}{\overset{m}{dx}_j} = \frac{\partial \overset{m}{x}_i^*}{\partial \overset{m}{x}_k} \frac{\overset{m}{dx}_k}{\overset{m}{dx}_j} \qquad \Rightarrow \tag{5.42}$$

$$\overset{m}{dx}_i^* = \frac{\partial \overset{m}{x}_i^*}{\partial \overset{m}{x}_k} \overset{m}{dx}_k \tag{5.43}$$

$$= x_{i,k}^* \overset{m}{dx}_k \tag{5.44}$$

Using the same approach for $\overset{n}{dx}_i^*$ leads to a similar expression:

$$\overset{n}{dx}_i^* = x_{i,j}^* \overset{n}{dx}_j \tag{5.45}$$

The angle between the two deformed line segments, θ, is expressed by the dot product of $\overset{m}{dx}_i^*$ and $\overset{n}{dx}_i^*$:

$$\left(\overset{m}{d}_s^*\right)\left(\overset{n}{d}_s^*\right) \cos(\theta) = \overset{m}{dx}_i^* \overset{n}{dx}_i^* \tag{5.46}$$

$$= x_{i,k}^* x_{i,j}^* \overset{m}{dx}_k \overset{n}{dx}_j \tag{5.47}$$

Using (5.16) and (5.25) $x_{i,k}^* x_{i,j}^*$ is rewritten to the following:

$$\left(x_{i,k}^* x_{i,j}^* - \delta_{kj}\right) dx_k dx_j = 2\varepsilon_{kj} dx_k dx_j \qquad \Rightarrow \tag{5.48}$$

$$x_{i,k}^* x_{i,j}^* = 2\varepsilon_{kj} + \delta_{kj} \tag{5.49}$$

Substitution of (5.49) into (5.47) leads to:

$$\left(\overset{m}{d}_s^*\right)\left(\overset{n}{d}_s^*\right) \cos(\theta) = \left(2\varepsilon_{kj} + \delta_{kj}\right) \overset{m}{dx}_k \overset{n}{dx}_j \tag{5.50}$$

$$= 2\varepsilon_{kj} \overset{m}{dx}_k \overset{n}{dx}_j + \overset{m}{dx}_k \overset{n}{dx}_k \tag{5.51}$$

$$= 2\varepsilon_{kj} \overset{m}{dx}_k \overset{n}{dx}_j \tag{5.52}$$

$$= 2\varepsilon_{kj} \overset{m}{ds}\, m_k \overset{n}{ds}\, n_j \qquad \Rightarrow \tag{5.53}$$

$$\cos(\theta) = 2\varepsilon_{kj} m_k n_j \frac{\overset{m}{ds}}{\left(\overset{m}{d}_s^*\right)} \frac{\overset{n}{ds}}{\left(\overset{n}{d}_s^*\right)} \qquad \Rightarrow \tag{5.54}$$

$$\frac{\cos(\theta)}{2} = \varepsilon_{kj} m_k n_j \frac{\overset{m}{ds}}{\left(\overset{m}{d}_s^*\right)} \frac{\overset{n}{ds}}{\left(\overset{n}{d}_s^*\right)} \tag{5.55}$$

In expression (5.37) it is assumed that the body is only subjected to small deformations which for the angular deflection can be expressed by $\frac{\overset{m}{ds}}{\left(\overset{m}{d}_s^*\right)} \frac{\overset{n}{ds}}{\left(\overset{n}{d}_s^*\right)} \approx 1$. The effect of this assumption is seen in the following expression:

$$\frac{\cos(\theta)}{2} = \frac{\sin\left(\frac{\pi}{2} - \theta\right)}{2} = \frac{\sin(\gamma)}{2} \approx \varepsilon_{kj} m_k n_j \tag{5.56}$$

When the angular deflection is assumed to be small, $\gamma \ll 1$, then expression (5.56) can be rewritten to:

$$\frac{\sin(\gamma)}{2} \approx \frac{\gamma}{2} = \varepsilon_{kj} m_k n_j \tag{5.57}$$

The quantity $\frac{\gamma}{2}$ is called the shear strain, which is also expressed by ψ. Equation (5.57) then leads to (5.58) where ψ is interpreted as half the angular change between two line segments:

$$\psi = \varepsilon_{ij} n_i m_j \tag{5.58}$$

On the basis of the above explanations, the elements of the strain tensor, ε_{ij}, have been specified. The equal components, $i = j$, represent the normal strains and the mixed components, $i \neq j$, represent the change of right angles within a deformed body. The mixed components are also referred to as shear strains. The only condition for this interpretation of the strain tensor is that the body is only subjected to small deformations.

Reviewing Lagrange's expression of the strain tensor (5.26) it may be assumed that the derivatives of the displacements may be small. With this assumption the product term $v_{k,i} v_{k,j}$ is small of higher order and may then be disregarded. Doing so leads to a linear expression of the strain tensor, which is referred to as Cauchy's strain tensor:

$$\varepsilon_{ij} = \frac{1}{2}\left(v_{i,j} + v_{j,i}\right) \tag{5.59}$$

5.2 Compatibility Equations

In section 5.1 the strain tensor was derived on the basis of point displacements within a continuum. Using Cauchy's formulation stated in (5.59), the three displacement equations provided six uniquely determined strains. The inverse problem of determining three unique displacements, from integration of the six partial differential equations describing the strains, cannot be solved directly. In order to solve this problem, additional restrictions have to be formulated to ensure a single-valued and continuous solution for a simply connected body. These restrictions are referred to as the compatibility equations. The following derivation of these equations is based on Shames and Cozzarelli [3, pp. 90–93].
Using Cauchy's formulation for the strain tensor shown in (5.59) the following derivatives can be formulated:

$$\varepsilon_{ij,kl} = \frac{1}{2}\left(v_{i,jkl} + v_{j,ikl}\right) \tag{5.60}$$

$$\varepsilon_{kl,ij} = \frac{1}{2}\left(v_{k,lij} + v_{l,kij}\right) \tag{5.61}$$

$$\varepsilon_{lj,ki} = \frac{1}{2}\left(v_{l,jki} + v_{j,lki}\right) \tag{5.62}$$

$$\varepsilon_{ki,lj} = \frac{1}{2}\left(v_{k,ijl} + v_{i,klj}\right) \tag{5.63}$$

Adding expressions (5.60) and (5.61) while subtracting (5.62) and (5.63) eliminates the displace-

ments and presents a formulation involving only the strains:

$$\begin{aligned}\varepsilon_{ij,kl}+\varepsilon_{kl,ij}-\varepsilon_{lj,ki}-\varepsilon_{ki,lj} =& \frac{1}{2}\left(v_{i,jkl}+v_{j,ikl}\right)+\frac{1}{2}\left(v_{k,lij}+v_{l,kij}\right)\\ &-\frac{1}{2}\left(v_{l,jki}+v_{j,lki}\right)-\frac{1}{2}\left(v_{k,ijl}+v_{i,klj}\right) \qquad (5.64)\\ =& \frac{1}{2}\left(v_{i,jkl}+v_{j,ikl}\right)+\frac{1}{2}\left(v_{k,lij}+v_{l,kij}\right)\\ &-\frac{1}{2}\left(v_{l,kij}+v_{j,ikl}\right)-\frac{1}{2}\left(v_{k,lij}+v_{i,jkl}\right) \qquad \Rightarrow \qquad (5.65)\\ \varepsilon_{ij,kl}+\varepsilon_{kl,ij}-\varepsilon_{lj,ki}-\varepsilon_{ki,lj} =& 0 \qquad (5.66)\end{aligned}$$

The rearrangement of the order of differentiation from equation (5.64) to (5.65) is valid due to the fact that v_i must be a continuous function. The final expression (5.66) consist of 81 equations, which restrict the strain equations so a unique and continuous solution can be obtained for the displacements. However, since expression (5.66) is described using four indices, each able to represent three different values e.g. $i = 1,2,3$, two of the four indices always represent the same value. The result of this condition is shown in the equation below:

$$\varepsilon_{(i)(i),kl}+\varepsilon_{kl,(i)(i)}-\varepsilon_{l(i),k(i)}-\varepsilon_{k(i),l(i)} = 0 \qquad (5.67)$$

Here the enclosed indices are regarded as free indices i.e. no summation of the repeated indices. This reduces the number of equations to 27 nonidentical. Furthermore, if two of the remaining indices equal each other, i.e. $k = i$ or $l = i$, then expression (5.67) leads to the trivial solution, $0 = 0$. This condition reduces the number of equations from 27 to 12 nontrivial. These 12 equations can further be reduced, due to the symmetry of the strain tensor e.g. $\varepsilon_{ij} = \varepsilon_{ji}$. This reduces the number of equations to six linearly independent relations. These equations are referred to as the compatibility equations. In compact form the equations can be expressed as shown in equation (5.68):

$$S_{pq} = e_{pkm}\, e_{qln}\, \varepsilon_{kl,mn} \qquad (5.68)$$

where: e The alternating symbol.

In explicit form, the compatibility equations are as follows:

$$\begin{aligned} i=1, k=l=2: \quad & S_{33} = \varepsilon_{11,22}+\varepsilon_{22,11}-2\varepsilon_{12,12} = 0 && (5.69)\\ i=2, k=l=3: \quad & S_{11} = \varepsilon_{22,33}+\varepsilon_{33,22}-2\varepsilon_{23,23} = 0 && (5.70)\\ i=3, k=l=1: \quad & S_{22} = \varepsilon_{33,11}+\varepsilon_{11,33}-2\varepsilon_{31,31} = 0 && (5.71)\end{aligned}$$

$$\begin{aligned} i=1, k=2, l=3: \quad & S_{23} = -\varepsilon_{11,23}-\varepsilon_{23,11}+\varepsilon_{31,12}+\varepsilon_{12,13} = 0 && (5.72)\\ i=2, k=3, l=1: \quad & S_{31} = -\varepsilon_{22,31}-\varepsilon_{31,22}+\varepsilon_{12,23}+\varepsilon_{23,21} = 0 && (5.73)\\ i=3, k=1, l=2: \quad & S_{12} = -\varepsilon_{33,12}-\varepsilon_{12,33}+\varepsilon_{23,31}+\varepsilon_{31,32} = 0 && (5.74)\end{aligned}$$

Remembering that six independent strains exist and only three independent displacements, the six compatibility equations do not provide an adequate degree of restriction for solving the problem of mapping the strains to the displacements. Further restrictions to the compatibility equations are required in order to obtain a valid solution. The last restrictions come from the Bianchi conditions:

$$\frac{\partial S_{pq}}{\partial x_q} = 0 \qquad (5.75)$$

Introducing this extra differentiation to the compatibility equations creates a dependence, reducing the number of independent conditions to three. Thus creating a means for ensuring a unique and continuous solution for the problem of expressing the displacements from a given strain field for a simply connected body. If the problem can be reduced to plane strain, the compatibility equations reduce to equation (5.69), which is a necessary condition to ensure a unique and continuous solution.
During the derivation of the three compatibility equations, differentiation of the elements in Cauchy's strain tensor have been done three times. A consequence of this is that the functions describing the strain field has to be at least C_3 continues, so as the trivial solution is avoided. During each differentiation, information within the strain functions is lost. The physical consequence of this loss of information is not treated in this text, and validity of the compatibility equations is assumed.

5.3 Stress Condition

In the following stresses within a continuum are defined and the stress tensor is determined at an arbitrary intersection. The equations of equilibrium are derived afterwards and the stress tensor is proven symmetric. Finally calculations and properties of the principle stresses and directions are shown.

Stresses are defined as internal forces of a continuum, and arise when external forces are applied to it. Two types of external forces are defined, body and traction forces. Body forces, B_i, act on every mass or volume element of the continuum, whereas the traction forces, T_i, only act on the surface(s) of the continuum. The body force vector, B_i is defined as the limit value of the load, p_i, acting on the volume element ΔV, when ΔV approaches zero:

$$B_i = \lim_{\Delta V \to 0} \left(\frac{p_i}{\Delta V} \right) \tag{5.76}$$

where: B_i Body force vector.
p_i Volume load.
ΔV Volume element subjected to volume load.

The traction vector T_i can be defined on an imaginary cut through the body, by making a cut in the body and collecting all the resultant forces and moments which are transferred across an area in a force vector, K_i, and a moment vector M_i, as shown in figure 5.5. Taking the limit value of K_i as the area ΔA approaches zero defines T_i:

$$T_i = \lim_{\Delta A \to 0} \left(\frac{K_i}{\Delta A} \right) \tag{5.77}$$

where: T_i Traction vector.
K_i Resultant force vector.
ΔA Area of imaginary cut.

Taking the limit value for the resultant moment M_i equates to zero when the area ΔA approaches zero, . This is because the moment arm approaches a length of zero, as the area

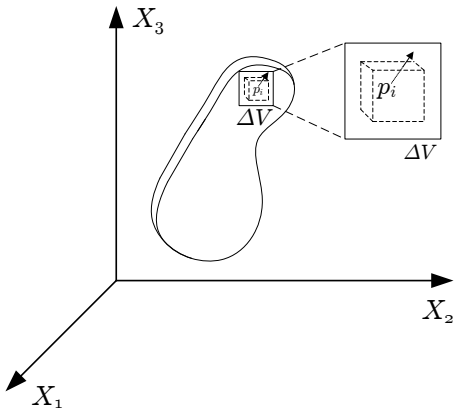

Figure 5.4: *Continuum body with applied volume loads.*

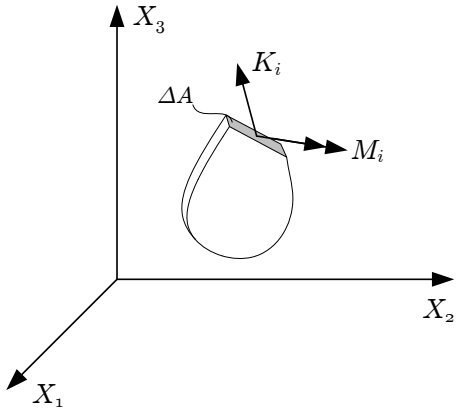

Figure 5.5: *Imaginary cut through the continuum body with resultant force and moment.*

becomes small:

$$\lim_{\Delta A \to 0} \left(\frac{M_i}{\Delta A} \right) = 0 \tag{5.78}$$

where: M_i Resultant moment vector.

The stresses at a given point P on the imaginary cut surface is defined by the components of the traction vector T_i, as shown in figure 5.6.

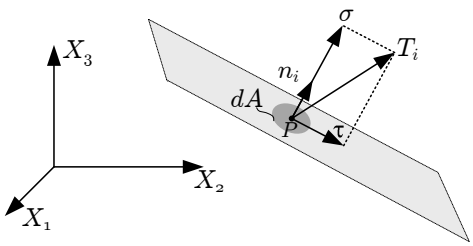

Figure 5.6: *Imaginary cut surface through point P.*

Projecting T_i on to a unit normal vector n_i perpendicular to the cut surface defines the normal stress σ:

$$\sigma = T_i n_i \tag{5.79}$$

The component parallel to the cut surface, τ, or shear stresses, are defined as:

$$\tau^2 = T_i T_i - \sigma^2 \tag{5.80}$$

The magnitude of both σ and τ thus depends on the orientation of the unit normal vector n_i and thus the cut surface.

5.3.1 Stresses in an Arbitrarily Chosen Intersection

The stress in a given point varies depending on the orientation of the cut surface. The explicit connection between the orientation of the surface and the components of the traction T_i can be explained by examining an infinitesimal tetrahedron as shown in figure 5.7.

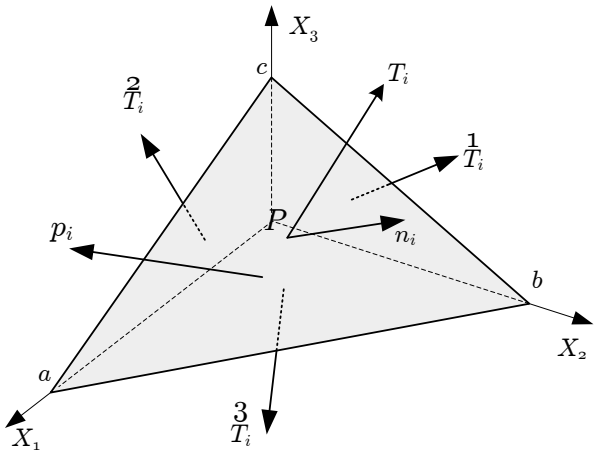

Figure 5.7: *Tetrahedron with infinitesimal dimensions and sides parallel to the coordinate planes.*

The orientation of the surface abc is uniquely defined by its unit normal $n_i = (n_1, n_2, n_3)$ while the other sides of the tetrahedron are coincident with the coordinate planes. The area of the inclined surface abc, denoted dA, is assumed adequately small for a homogeneous state of stress to exist within the tetrahedron. The area of the remaining sides of the tetrahedron can be determined by projecting the area dA onto the coordinate planes. This can be done by multiplying dA with the respective component of the unit normal n_i. If the tetrahedron is assumed to be in static equilibrium, the sum of forces acting on the element must equate to zero:

$$T_i dA + \overset{1}{T}_i \, n_1 \, dA + \overset{2}{T}_i \, n_2 \, dA + \overset{3}{T}_i \, n_3 \, dA + \frac{1}{3} dh \, dA \, p_i = 0 \tag{5.81}$$

where: dh The perpendicular height from the surface abc to point P.

$\overset{j}{T}_i$ Traction on surface with unit normal n_j.

Since the height dh is assumed very small, the term including the body force is small of higher order and is then neglected. Applying this assumption and rearranging the terms leads to:

$$T_i = -\left(\overset{1}{T}_i \, n_1 + \overset{2}{T}_i \, n_2 + \overset{3}{T}_i \, n_3 \right) \tag{5.82}$$

$$= \sigma_{1i} \, n_1 + \sigma_{2i} \, n_2 + \sigma_{3i} \, n_3 \tag{5.83}$$

$$= \sigma_{ji} \, n_j \tag{5.84}$$

The above expression is referred to in general as *Cauchy's formula.* This states that the stress at any point is uniquely defined by the stress tensor σ_{ji}. Substituting this expression into the definition of the normal stress σ from (5.79), leads to the following definition of the normal stress σ:

$$\sigma = \sigma_{ji} \, n_j \, n_i \tag{5.85}$$

Using the above formulation for σ and T_i then τ can be reformulated using only the stress

tensor σ_{ji}. Substituting (5.85) and (5.84) into equation (5.80):

$$T_i T_i = \tau^2 + \sigma^2 \qquad \Rightarrow \tag{5.86}$$

$$\tau^2 = T_i T_i - \sigma^2 \tag{5.87}$$

$$= \left(\sigma_{ji}\, n_j\right)\left(\sigma_{kl}\, n_k\right) - \left(\sigma_{ji}\, n_j\, n_i\right)\left(\sigma_{kl}\, n_k\, n_l\right) \tag{5.88}$$

$$\tag{5.89}$$

Selecting a unit normal parallel with the first coordinate axis, $n_i = (1,0,0)$, shows which elements of the stress tensor τ consists of that particular plane:

$$\tau^2 = \left(\sigma_{ji}\, n_j\right)\left(\sigma_{kl}\, n_k\right) - \left(\sigma_{ji}\, n_j\, n_i\right)\left(\sigma_{kl}\, n_k\, n_l\right) \qquad \Rightarrow \tag{5.90}$$

$$\tau_1^2 = \begin{bmatrix}\sigma_{11}\\ \sigma_{12}\\ \sigma_{13}\end{bmatrix}\begin{bmatrix}\sigma_{11}\\ \sigma_{12}\\ \sigma_{13}\end{bmatrix} - \begin{bmatrix}\sigma_{11}\\ 0\\ 0\end{bmatrix}\begin{bmatrix}\sigma_{11}\\ 0\\ 0\end{bmatrix} \tag{5.91}$$

$$= \sigma_{11}^2 + \sigma_{12}^2 + \sigma_{13}^2 - \sigma_{11}^2 \tag{5.92}$$

$$= \sigma_{12}^2 + \sigma_{13}^2 \tag{5.93}$$

Using the same approach for unit normals parallel with the remaining two coordinate axes gives the following:

$$\tau_2^2 = \sigma_{21}^2 + \sigma_{23}^2 \tag{5.94}$$

$$\tau_3^2 = \sigma_{31}^2 + \sigma_{32}^2 \tag{5.95}$$

The above formulations show that τ consists of two components within the given plane of interest. These components are referred to as shear stresses. Thus the stress tensor σ_{ij} consists of nine elements, three normal stresses and six shear stresses, which is shown below in explicit form:

$$\sigma_{ij} = \begin{pmatrix}\sigma_{11} & \sigma_{12} & \sigma_{13}\\ \sigma_{21} & \sigma_{22} & \sigma_{23}\\ \sigma_{31} & \sigma_{32} & \sigma_{33}\end{pmatrix} \tag{5.96}$$

$$\tag{5.97}$$

5.3.2 Equations of Equilibrium

The stress condition inside a continuous body changes when traction and body forces are applied. Assuming that the associated deformation is small which is explicit described by the formulation of Cauchy's strain tensor in section 5.1, the equilibrium condition can be described by studying an undeformed parallelepiped, as shown in figure 5.8. The following derivation is based on Olhoff [4, pp. 6–8]. The parallelepiped is affected by a body force in the centre and stress components at each sides. In structural mechanics the most common body force is gravity. Since this type of force acts on every volume element the net force can in the case of the parallelepiped be considered as an average value. The variation of stresses over the entire length of the parallelepiped can be described by a Taylor series:

$$\sigma'_{ij} = \sigma_{ij} + \frac{1}{1!}\sigma_{ij,k}\, dx_k + \frac{1}{2!}\sigma_{ij,kl}\, dx_k\, dx_l + \ldots \tag{5.98}$$

If a parallelepiped is assumed infinitesimal in size, the higher order terms become negligible and can be disregarded. Thus a linear expression for the change in stress along the length is obtained:

$$\sigma'_{ij} = \sigma_{ij} + \sigma_{ij,k} \cdot dx_k \tag{5.99}$$

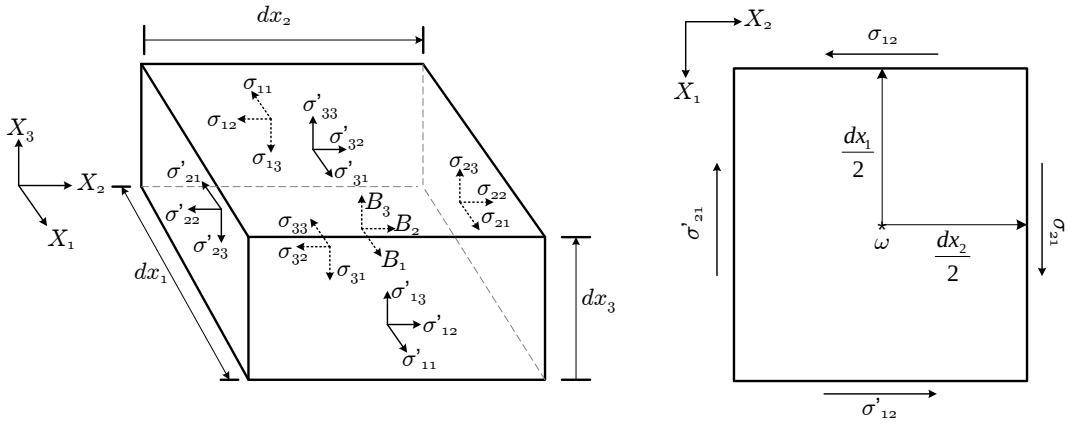

Figure 5.8: *Infinitesimal parallelepiped with sides parallel to the axes of the coordinate system.*

where: dx_k The length, width, or height of the infinitesimal parallelepiped.

σ_{ij} The stress tensor.

The equilibrium for the parallelepiped in the direction of the axis X_1 is given as:

$$(\sigma_{11}+\sigma_{11,1}dx_1)dx_2dx_3-\sigma_{11}dx_2dx_3+(\sigma_{21}+\sigma_{21,2}dx_2)dx_1dx_3-\sigma_{21}dx_1dx_3 \\ +(\sigma_{31}+\sigma_{31,3}dx_3)dx_1dx_2-\sigma_{31}dx_1dx_2+B_1dx_1dx_2dx_3=0 \quad \Rightarrow \quad (5.100)$$

$$(\sigma_{11}+\sigma_{11,1}dx_1-\sigma_{11})dx_2dx_3+(\sigma_{21}+\sigma_{21,2}dx_2-\sigma_{21})dx_1dx_3 \\ +(\sigma_{31}+\sigma_{31,3}dx_3-\sigma_{31})dx_1dx_2+B_1dx_1dx_2dx_3=0 \quad \Rightarrow \quad (5.101)$$

$$\sigma_{11,1}dx_1dx_2dx_3+\sigma_{21,2}dx_2dx_1dx_3+\sigma_{31,3}dx_3dx_1dx_2+B_1dx_1dx_2dx_3=0 \quad \Rightarrow \quad (5.102)$$

$$\sigma_{11,1}+\sigma_{21,2}+\sigma_{31,3}+B_1=0 \quad (5.103)$$

Using the same approach for the remaining directions yields similar results. Thus the familiar expression for the equation of equilibrium is obtained:

$$\sigma_{ij,i}+B_j=0 \quad (5.104)$$

where: B_j The body force.

Formulating the equilibrium of torque about the centre for the infinitesimal parallelepiped, and assuming that the net force from the stresses act in the centre of the surface in question, it is possible to show that the stress tensor is symmetric. The situation is illustrated for the equilibrium about the X_3 axis in figure 5.8. The equilibrium is formulated as:

$$\sum M_\omega=0 \quad \Rightarrow \quad (5.105)$$

$$\sigma_{12}dx_2dx_3\frac{dx_1}{2}-\sigma_{21}dx_1dx_3\frac{dx_2}{2}+\sigma'_{12}dx_2dx_3\frac{dx_1}{2}-\sigma'_{21}dx_1dx_3\frac{dx_2}{2}=0 \quad \Rightarrow \quad (5.106)$$

$$\frac{1}{2}\sigma_{12}-\frac{1}{2}\sigma_{21}+\frac{1}{2}(\sigma_{12}+\sigma_{12,1}dx_1)-\frac{1}{2}(\sigma_{21}+\sigma_{21,2}dx_2)=0 \quad \Rightarrow \quad (5.107)$$

$$2\sigma_{12}-2\sigma_{21}+\sigma_{12,1}dx_1-\sigma_{21,2}dx_2=0 \quad \Rightarrow \quad (5.108)$$

$$\sigma_{12,1}\frac{dx_1}{2}-\sigma_{21,2}\frac{dx_2}{2}+\sigma_{12}-\sigma_{21}=0 \quad (5.109)$$

The product terms in (5.109) can be neglected due to the infinitesimal size of the parallelepiped, which yields the following result:

$$\sigma_{12} = \sigma_{21} \tag{5.110}$$

Formulating the torque equilibrium for the remaining directions yields similar expressions as equation (5.110). Thus a general expression can be formulated as:

$$\sigma_{ij} = \sigma_{ji} \tag{5.111}$$

The above equation proves that the stress tensor is symmetric.

5.3.3 Principal Stresses and Directions

The intensity of stress components varies depending on the orientation of the intersection in question. The intersection is defined by a unit normal n_i. The stress component σ can be defined as the function:

$$f(n_1, n_2, n_3) = \sigma_{ij} n_i n_j \tag{5.112}$$

For each point there exist an intersection with a direction where the stresses are maximum and minimum. Determining the extremes corresponds to calculating the partial derivatives regarding to the unit normals with respect to zero. The solution must satisfy the length of the unit normals, as formulated through the following interrelation:

$$n_i n_i - 1 = 0 \tag{5.113}$$

It is possible to determine a solution which obeys the condition by using the *Lagrange Multiplier Method*. Multiplying the interrelation with the Lagrange multiplier λ and subtracting the result from (5.112), yields a new function where the stress components now also depend on λ. Mathematically this corresponds to subtracting the value of zero from (5.112):

$$H(n_1, n_2, n_3, \lambda) = \sigma_{ij} n_i n_j - \lambda(n_i n_i - 1) \tag{5.114}$$

where: λ Lagrange multiplier.

Calculating the partial derivative of (5.114) with respect to λ, shows that the new function obeys the interrelation of the unit normal, when searching for extreme values of σ:

$$\frac{\partial H(n_1, n_2, n_3, \lambda)}{\partial \lambda} = -(n_i n_i - 1) = 0 \tag{5.115}$$

The extremes are determined by taking the partial derivative of (5.114) with respect to n_k:

$$\frac{\partial H(n_1, n_2, n_3, \lambda)}{\partial n_k} = \sigma_{ij}\left(\frac{\partial n_i}{\partial n_k} n_j + \frac{\partial n_j}{\partial n_k} n_i\right) - 2\lambda\left(\frac{\partial n_i}{\partial n_k} n_i\right) = 0 \quad \Rightarrow \tag{5.116}$$

$$\frac{\partial H(n_1, n_2, n_3, \lambda)}{\partial n_k} = \sigma_{ij}\left(\delta_{ik} n_j + \delta_{jk} n_i\right) - 2\lambda\left(\delta_{ik} n_i\right) = 0 \quad \Rightarrow \tag{5.117}$$

$$\sigma_{kj} n_j + \sigma_{ik} n_i - 2\lambda \delta_{ik} n_i = 0 \quad \Rightarrow \tag{5.118}$$

$$2(\sigma_{kj} - \lambda \delta_{kj}) n_j = 0 \quad \Rightarrow \tag{5.119}$$

$$(\sigma_{ij} - \lambda \delta_{ij}) n_j = 0 \tag{5.120}$$

The interrelation in expression (5.113) eliminates $n_j = 0$. Thus a non trivial solution for (5.120) is obtained by calculating the determinant:

$$det(\sigma_{ij} - \lambda\delta_{ij}) = \begin{vmatrix} \sigma_{11}-\lambda & \sigma_{12} & \sigma_{13} \\ \sigma_{21} & \sigma_{22}-\lambda & \sigma_{23} \\ \sigma_{31} & \sigma_{32} & \sigma_{33}-\lambda \end{vmatrix} = 0 \qquad \Rightarrow \tag{5.121}$$

$$-\lambda^3 + \zeta_1\lambda^2 - \zeta_2\lambda + \zeta_3 = 0 \tag{5.122}$$

The coefficients ζ are given in (5.123)-(5.125). These coefficients are also known as the invariants for the general stress field, and are not influenced if the field is transformed to another coordinate system:

$$\zeta_1 = \sigma_{11} + \sigma_{22} + \sigma_{33} \tag{5.123}$$

$$\zeta_2 = \sigma_{22}\sigma_{33} + \sigma_{11}\sigma_{22} + \sigma_{11}\sigma_{33} - \sigma_{31}^2 - \sigma_{23}^2 - \sigma_{12}^2 \tag{5.124}$$

$$\zeta_3 = \sigma_{11}\sigma_{22}\sigma_{33} + 2\sigma_{12}\sigma_{32}\sigma_{31} - \sigma_{11}\sigma_{23}^2 - \sigma_{22}\sigma_{31}^2\sigma_{33}\sigma_{12}^2 \tag{5.125}$$

The solution of equation (5.122) gives three roots λ_1,λ_2 and λ_3. Each of the values correspond to one of the directions where the stress is extreme. Multiplying expression (5.120) by the direction of λ yields:

$$(\sigma_{ij} - \lambda\delta_{ij})n_j n_i = 0 \qquad \Rightarrow \tag{5.126}$$

$$\lambda = \sigma_{ij} n_i n_j \tag{5.127}$$

Equation (5.127) shows that each root λ gives an extreme stress value in the direction of the corresponding n_i. The problem of determining principal stresses is now recognised as an eigenvalue problem. Thus λ is an eigenvalue and the eigenvectors are equal to the unit normal vector pointing in the principal direction. Since eigenvectors are linearly independent, the three eigenvectors corresponding to the three values of λ must be perpendicular to one another.
The shear stresses between the directions are zero. It can be be shown by taking two principal stresses, σ_m and σ_n, with directions m_i and n_i. Since $\sigma_m \neq \sigma_n$ the to directions must be perpendicular, so $m_i n_i = 0$. Substituting the conditions into equation (5.126), and sum the equations, shows that the shear stresses are zero:

$$(\sigma_{ij} - \sigma_m\delta_{ij})m_j n_i + (\sigma_{ij} - \sigma_n\delta_{ij})n_j m_i = 0 \qquad \Rightarrow \tag{5.128}$$

$$\sigma_{ij}m_j n_i + \sigma_{ij}n_j m_i - \sigma_m\delta_{ij}m_j n_i - \sigma_n\delta_{ij}n_j m_i = 0 \qquad \Rightarrow \tag{5.129}$$

$$\sigma_{ij}m_j n_i + \sigma_{ij}n_j m_i - \sigma_m m_i n_i - \sigma_n n_i m_i = 0 \qquad \Rightarrow \tag{5.130}$$

$$\sigma_{ij}n_i m_j = 0 \tag{5.131}$$

The above derivation of the principal stresses and directions can be applied to any second order tensor.

5.4 Hooke's Generalised Law

Hooke's generalised law states that for a linear elastic material there has to be a linear connection between stress and strain. Many commonly used materials can with good approximation be regarded as linear elastic within a limit. For metal the linear limit is normally just below the materials yield strength, where the material will exhibit plastic deformation. Hooke's generalised law consists of a stress tensor, a strain tensor, and an elasticity constant tensor given by the following relation:

$$\sigma_{ij} = C_{ijkl}\varepsilon_{kl} \tag{5.132}$$

The elasticity constants are represented by the fourth order tensor C_{ijkl} and contains 81 elements. To make practical applicability of Hooke's generalised law it is desirable to reduce the expression. As proven in section 5.1 and 5.3 the strain tensor and the stress tensor are both symmetric, cf. (5.30) and (5.111). Since a symmetric tensor multiplied with the elasticity constant tensor equals to another symmetric tensor, C_{ijkl} has to be symmetric too. This reduces the number of independent elements in the tensor down to 36. The tensor can further be reduced to 21 elements due to thermodynamic principles which will not be presented here. These 21 elements are in general the minimum number of elasticity constants needed to calculate the behavior of a three dimensional body that is linear elastic.

It is possible to consider most metals as isotropic. This means that the elastic properties are the same in every direction within the material in contrast to e.g. wood and fiber based materials. An isotropic tensor of fourth order can be derived by applying the operator Kronecker's delta:

$$C_{ijkl} = \alpha\delta_{ij}\delta_{kl} + \beta\delta_{ik}\delta_{jl} + \gamma\delta_{il}\delta_{jk} \tag{5.133}$$

where: α, β, γ Constants.

Hooke's generalised law for an isotropic material is:

$$\begin{aligned}
\sigma_{ij} &= (\alpha\delta_{ij}\delta_{kl} + \beta\delta_{ik}\delta_{jl} + \gamma\delta_{il}\delta_{jk})\varepsilon_{kl} && (5.134)\\
&= \alpha\delta_{ij}\varepsilon_{kk} + \beta\varepsilon_{ij} + \gamma\varepsilon_{ij} && (5.135)\\
&= (\beta+\gamma)\varepsilon_{ij} + \alpha\delta_{ij}\varepsilon_{kk} && (5.136)
\end{aligned}$$

It is possible to further reduce the number of constants down to two by introducing Lame's constants μ and λ. These are defined as $2\mu = \beta + \gamma$ and $\lambda = \alpha$. Substituting these into equation (5.136) yields:

$$\sigma_{ij} = 2\mu\varepsilon_{ij} + \lambda\delta_{ij}\varepsilon_{kk} \tag{5.137}$$

By multiplying (5.137) with δ_{ij} the tensor ε_{kk} can be found. This makes equation (5.137) resolvable for ε_{ij} as shown below:

$$\begin{aligned}
\sigma_{ij}\delta_{ij} &= 2\mu\varepsilon_{ij}\delta_{ij} + \lambda\delta_{ij}\delta_{ij}\varepsilon_{kk} && \Rightarrow && (5.138)\\
\sigma_{ii} &= 2\mu\varepsilon_{ii} + 3\lambda\varepsilon_{kk} && && (5.139)\\
&= (2\mu+3\lambda)\varepsilon_{kk} && \Rightarrow && (5.140)\\
\varepsilon_{kk} &= \frac{\sigma_{ii}}{2\mu+3\lambda} && && (5.141)
\end{aligned}$$

When (5.141) is put into (5.137) and σ_{ii} is renamed as σ_{kk} equation (5.137) will become:

$$\begin{aligned}
\sigma_{ij} &= 2\mu\varepsilon_{ij} + \frac{\lambda}{2\mu+3\lambda}\delta_{ij}\sigma_{kk} && \Rightarrow && (5.142)\\
2\mu\varepsilon_{ij} &= \sigma_{ij} - \frac{\lambda}{2\mu+3\lambda}\delta_{ij}\sigma_{kk} && && (5.143)
\end{aligned}$$

At this point it is practical to replace Lame's constants with some constants that are easier to work with. Poisson's ratio, ν, and Young's modulus, E, are both possible to measure trough

single-axial loading of standardized test specimens, which makes them quite easy to determine. In a single-axial stress situation the stress tensor will have only one component:

$$\sigma_{ij} = \begin{pmatrix} \sigma & 0 & 0 \\ 0 & 0 & 0 \\ 0 & 0 & 0 \end{pmatrix} \tag{5.144}$$

Based on (5.144) Young's modulus and Poisson's ratio will be defined as:

$$E = \frac{\sigma_{11}}{\varepsilon_{11}} \tag{5.145}$$

$$\nu = -\frac{\varepsilon_{22}}{\varepsilon_{11}} = -\frac{\varepsilon_{33}}{\varepsilon_{11}} \tag{5.146}$$

In this single-axial stress situation ($i = j = 1$) equation (5.143) becomes:

$$2\mu\varepsilon_{11} = \sigma_{11} - \frac{\lambda}{2\mu + 3\lambda}\sigma_{11} \tag{5.147}$$

$$= \frac{2(\mu+\lambda)}{2\mu+3\lambda}\sigma_{11} \qquad \Rightarrow \tag{5.148}$$

$$E = \frac{\mu(2\mu+3\lambda)}{\mu+\lambda} \qquad \Rightarrow \tag{5.149}$$

$$\mu = \frac{E}{2(1+\nu)} \tag{5.150}$$

In a perpendicular direction ($i = j = 2$ or $i = j = 3$) there will not be any stress components for the same stress situation, but the strain tensor will have a component in each direction. As shown in (5.146) ν becomes the same in both direction 2 and direction 3, so ν is put into one of them:

$$2\mu\varepsilon_{22} = -\frac{\lambda}{2\mu+3\lambda}\sigma_{11} \qquad \Rightarrow \tag{5.151}$$

$$\nu = -\frac{(\frac{-\lambda}{2\mu+3\lambda})}{(\frac{2(\mu+\lambda)}{2\mu+3\lambda})} \tag{5.152}$$

$$= \frac{\lambda}{2(\mu+\lambda)} \qquad \Rightarrow \tag{5.153}$$

$$\lambda = \frac{E\nu}{(1+\nu)(1-2\nu)} \tag{5.154}$$

The equations (5.150) and (5.154) can be put into (5.137) and (5.143). From an engineers perspective this constitutes Hooke's generalised law in its most usable form. This is shown in the general equation with respect to stress and with respect to strain as:

$$\sigma_{ij} = \frac{E}{1+\nu}\left(\varepsilon_{ij} + \frac{\nu}{1-2\nu}\delta_{ij}\varepsilon_{kk}\right) \tag{5.155}$$

$$\varepsilon_{ij} = \frac{1}{E}\left((1+\nu)\sigma_{ij} - \nu\delta_{ij}\sigma_{kk}\right) \tag{5.156}$$

Hooke's generalised law (5.155) includes tensor expressions. This means it actually consists of six independant equations. They are usually solved with respect to σ or ε. The complete set of

equations for stress and strain look like:

$$\left.\begin{aligned}
\sigma_{11} &= \tfrac{E}{1+\nu}(\varepsilon_{11} + \tfrac{\nu}{1-2\nu}(\varepsilon_{11}+\varepsilon_{22}+\varepsilon_{33})) \\
\sigma_{22} &= \tfrac{E}{1+\nu}(\varepsilon_{22} + \tfrac{\nu}{1-2\nu}(\varepsilon_{11}+\varepsilon_{22}+\varepsilon_{33})) \\
\sigma_{33} &= \tfrac{E}{1+\nu}(\varepsilon_{33} + \tfrac{\nu}{1-2\nu}(\varepsilon_{11}+\varepsilon_{22}+\varepsilon_{33})) \\
\sigma_{12} &= \tfrac{E}{1+\nu}\varepsilon_{12} \\
\sigma_{13} &= \tfrac{E}{1+\nu}\varepsilon_{13} \\
\sigma_{23} &= \tfrac{E}{1+\nu}\varepsilon_{23}
\end{aligned}\right\} \tag{5.157}$$

$$\left.\begin{aligned}
\varepsilon_{11} &= \tfrac{1}{E}(\sigma_{11} - \nu(\sigma_{22}+\sigma_{33})) \\
\varepsilon_{22} &= \tfrac{1}{E}(\sigma_{22} - \nu(\sigma_{11}+\sigma_{33})) \\
\varepsilon_{33} &= \tfrac{1}{E}(\sigma_{33} - \nu(\sigma_{11}+\sigma_{22})) \\
\varepsilon_{12} &= \tfrac{1+\nu}{E}\sigma_{12} \\
\varepsilon_{13} &= \tfrac{1+\nu}{E}\sigma_{13} \\
\varepsilon_{23} &= \tfrac{1+\nu}{E}\sigma_{23}
\end{aligned}\right\} \tag{5.158}$$

5.4.1 Plane stress and plane strain

There are two case specific versions of Hooke's generalised law for plane stress and plane strain. By applying these simplifications for appropriate problems, the computational difficulty can be reduced, while maintaining a large degree of accuracy. However, if the required assumptions are not met the obtained results can be useless.

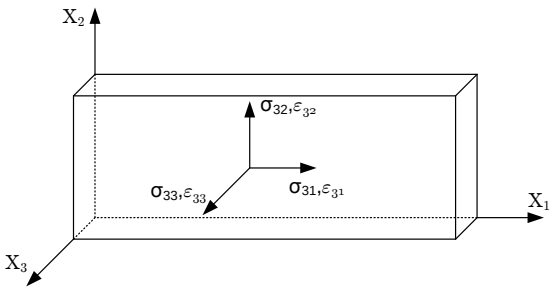

Figure 5.9: *A free surface in a plane stress situation.*

5.4.1.1 Plane stress

If an object has a surface that is not directly exposed to any forces or pressure it is possible to assume that there is a plane stress situation. As long as a system is static, every stress component has got to have an equal stress component in the opposite direction. Consequently, a surface that is not exposed to any force or pressure does not have any stress component. If a body has a so called free surface in the X_1- X_2-plane, the surface would be free from any stress: $\sigma_{33} = \sigma_{31} = \sigma_{32} = 0$. When this assumption is put into the equations in (5.158) they are reduced to the equations in (5.159). The assumptions above, and the equations below, should always be used in situations where the distance between the two surfaces in the X_1- X_2-plane is small compared to the other dimensions. That is because plane stress usually is assumed to apply all the way through the body, which is a good assumption for a thin object such a plate, or the

wind sails on a boat:

$$\left.\begin{aligned}
\varepsilon_{11} &= \tfrac{1}{E}(\sigma_{11} - \nu\sigma_{22}) \\
\varepsilon_{22} &= \tfrac{1}{E}(\sigma_{22} - \nu\sigma_{11}) \\
\varepsilon_{33} &= -\tfrac{\nu}{E}(\sigma_{11} + \sigma_{22}) \\
\varepsilon_{12} &= \tfrac{1+\nu}{E}\sigma_{12} \\
\varepsilon_{13} &= \tfrac{1+\nu}{E}\sigma_{13} = 0 \\
\varepsilon_{23} &= \tfrac{1+\nu}{E}\sigma_{23} = 0
\end{aligned}\right\} \tag{5.159}$$

The plane stress equations can also be expressed with respect to stresses:

$$\left.\begin{aligned}
\sigma_{11} &= \tfrac{E}{1-\nu^2}(\varepsilon_{11} + \nu\varepsilon_{22}) \\
\sigma_{22} &= \tfrac{E}{1-\nu^2}(\varepsilon_{22} + \nu\varepsilon_{11}) \\
\sigma_{33} &= 0 \\
\sigma_{12} &= \tfrac{E}{1+\nu}\varepsilon_{12} \\
\sigma_{13} &= 0 \\
\sigma_{23} &= 0
\end{aligned}\right\} \tag{5.160}$$

As can be observed from expression (5.159), all the strain components are non trivial due to Poisson's effect. Thus determining the displacement field on the account of the strains still requires the use of the three compatibility equations discussed in section 5.2.

5.4.1.2 Plane Strain

For bodies that stretch over a large area relative to the thickness, and are exposed to forces perpendicular to the wide surface, it is possible to assume plane strain. The classic example is that of a dam, which is very wide relative its thickness. In the same X_1- X_2-plane that were exemplified for plane stress the situation would be the opposite. Thus the surface exposed to forces or pressures, but the strain components are set to be zero ($\varepsilon_{33} = \varepsilon_{31} = \varepsilon_{32} = 0$). If these conditions are applied equations in (5.157) become:

$$\left.\begin{aligned}
\sigma_{11} &= \tfrac{E}{1+\nu^2}(\varepsilon_{11} + \tfrac{\nu}{1-2\nu}\varepsilon_{11} + \varepsilon_{22}) \\
\sigma_{22} &= \tfrac{E}{1+\nu^2}(\varepsilon_{22} + \tfrac{\nu}{1-2\nu}\varepsilon_{11} + \varepsilon_{22}) \\
\sigma_{33} &= \tfrac{E\nu}{(1+\nu)(1-2\nu)}(\varepsilon_{11} + \varepsilon_{22}) \\
\sigma_{12} &= \tfrac{E}{1+\nu}\varepsilon_{12} \\
\sigma_{13} &= \tfrac{E}{1+\nu}\varepsilon_{13} = 0 \\
\sigma_{23} &= \tfrac{E}{1+\nu}\varepsilon_{23} = 0
\end{aligned}\right\} \tag{5.161}$$

$$\left.\begin{aligned}
\varepsilon_{11} &= \tfrac{1-\nu^2}{E}(\sigma_{11} - \tfrac{\nu}{1-\nu}\sigma_{22}) \\
\varepsilon_{22} &= \tfrac{1-\nu^2}{E}(\sigma_{22} - \tfrac{\nu}{1-\nu}\sigma_{11}) \\
\varepsilon_{33} &= 0 \\
\varepsilon_{12} &= \tfrac{1+\nu}{E}\sigma_{12} \\
\varepsilon_{13} &= \tfrac{1+\nu}{E}\sigma_{13} = 0 \\
\varepsilon_{23} &= \tfrac{1+\nu}{E}\sigma_{23} = 0
\end{aligned}\right\} \tag{5.162}$$

Applying these expressions yield more accurate results than if the equations in (5.157) and (5.160) are used. Therefore, in situations where plane strain can be assumed, the equations in (5.161) and (5.162) should always be used. Because the strains $\varepsilon_{33}, \varepsilon_{31}$, and ε_{32} all have zero values the compatibility equations for plane strain are reduced to one equation as:

$$\varepsilon_{11,22} + \varepsilon_{22,11} - 2\varepsilon_{12,12} = 0 \tag{5.163}$$

5.5 Airy's Stress Function

The governing equations for the elastic problem is reduced to eight coupled partial differential equations for plain strain. These are reproduced in the following. The eight equations consist of three equations for relating displacements to strains, two equations of equilibrium and finally three constitutive equations relating strains to stresses:

$$\varepsilon_{11} = \frac{1}{2}\left(v_{1,1} + v_{1,1}\right) \tag{5.164}$$

$$\varepsilon_{12} = \frac{1}{2}\left(v_{1,2} + v_{2,1}\right) \tag{5.165}$$

$$\varepsilon_{22} = \frac{1}{2}\left(v_{2,2} + v_{2,2}\right) \tag{5.166}$$

$$\tag{5.167}$$

$$\sigma_{11,1} + \sigma_{21,2} + B_1 = 0 \tag{5.168}$$

$$\sigma_{22,2} + \sigma_{12,1} + B_2 = 0 \tag{5.169}$$

$$\tag{5.170}$$

$$\varepsilon_{11} = \frac{1-\nu^2}{E}\left(\sigma_{11} - \frac{\nu}{1-\nu}\sigma_{22}\right) \tag{5.171}$$

$$\varepsilon_{12} = \frac{1+\nu}{E}\sigma_{12} \tag{5.172}$$

$$\varepsilon_{22} = \frac{1-\nu^2}{E}\left(\sigma_{22} - \frac{\nu}{1-\nu}\sigma_{11}\right) \tag{5.173}$$

Instead of solving the above eight equations, while also ensuring compatibility for the given solution, the equations may be rewritten so only one equation has to be solved. This rewritten equation is known as the biharmonic equation and it satisfies compatibility and ensures equilibrium. In the following the biharmonic equation is derived. The theory used is based upon Ugural and Fenster [5, pp.97–103]. In section 5.4.1.2 it is showed that the equations of compatibility can be reduced to the following expression for a plane strain problem:

$$\varepsilon_{11,22} + \varepsilon_{22,11} - 2\,\varepsilon_{12,12} = 0 \tag{5.174}$$

Rewriting the compatibility equation in terms of stresses expressed in equation (5.171) to (5.173) leads to expression:

$$\frac{1-\nu^2}{E}\left(\sigma_{11,22} - \frac{\nu}{1-\nu}\sigma_{22,22}\right) + \frac{1-\nu^2}{E}\left(\sigma_{22,11} - \frac{\nu}{1-\nu}\sigma_{11,11}\right) - 2\,\frac{1+\nu}{E}\sigma_{12,12} = 0 \quad \Rightarrow \tag{5.175}$$

$$(1-\nu)\,\sigma_{11,22} - \nu\,\sigma_{22,22} + (1-\nu)\,\sigma_{22,11} - \nu\,\sigma_{11,11} = 2\sigma_{12,12} \tag{5.176}$$

Expression (5.176) is further rewritten in the following. Differentiating the equilibrium equations (5.168) and (5.169) with respect to x and y, respectively, and adding them together leads to:

$$\sigma_{11,11} + \sigma_{21,21} + B_{1,1} + \sigma_{22,22} + \sigma_{12,12} + B_{2,2} = 0 \quad \Rightarrow \tag{5.177}$$

$$-\left(\sigma_{11,11} + \sigma_{22,22}\right) - \left(B_{1,1} + B_{2,2}\right) = 2\,\sigma_{12,12} \tag{5.178}$$

Combining equations (5.176) and (5.178) leads to the following expression:

$$(1-\nu)\,\sigma_{11,22} - \nu\,\sigma_{22,22} + (1-\nu)\,\sigma_{22,11} - \nu\,\sigma_{11,11} = -\left(\sigma_{11,11} + \sigma_{22,22}\right) - \left(B_{1,1} + B_{2,2}\right) \quad \Rightarrow \tag{5.179}$$

$$(\sigma_{11,22} + \sigma_{22,11}) + (\sigma_{11,11} + \sigma_{22,22}) = \frac{-1}{(1-\nu)}\left(B_{1,1} + B_{2,2}\right) \tag{5.180}$$

Expression (5.180) represents the compatibility equation for plane strain in terms of stresses. Introducing the stress function $\Phi(x, y)$ first presented by G.B. Airy, from which the stresses in two dimension is defined by:

$$\sigma_{11} = \frac{\partial^2 \Phi}{\partial x_2^2} \tag{5.181}$$

$$\sigma_{22} = \frac{\partial^2 \Phi}{\partial x_1^2} \tag{5.182}$$

$$\sigma_{12} = -\frac{\partial^2 \Phi}{\partial x_1 \partial x_2} \tag{5.183}$$

The body forces can be neglected when assuming they are small in magnitude or of constant value. Then the equilibrium equations (5.168) and (5.169) and the compatibility equation (5.180) can be reduced to:

$$\sigma_{11,1} + \sigma_{21,2} = 0 \tag{5.184}$$

$$\sigma_{22,2} + \sigma_{12,1} = 0 \tag{5.185}$$

$$(\sigma_{11,22} + \sigma_{22,11}) + (\sigma_{11,11} + \sigma_{22,22}) = 0 \tag{5.186}$$

Substituting Airy's stress definitions into the equilibrium equation (5.184) and (5.185) reveals that the stress definitions identically satisfy the equilibrium conditions. Substituting the stress definitions into the equation of compatibility leads to the desired biharmonic equation:

$$\frac{\partial^4 \Phi}{\partial x_1^4} + 2\frac{\partial^4 \Phi}{\partial x_1^2 \partial x_2^2} + \frac{\partial^4 \Phi}{\partial x_2^4} = \nabla^4 \Phi = 0 \tag{5.187}$$

The biharmonic equation can be solved for a given plane strain problem together with suitable boundary conditions where body forces are absent, guaranteeing a solution with a compatible stress field which satisfies the equilibrium conditions.
For plane stress problems, where ε_{33} may have a nontrivial value, due to the dependence of σ_{11} and σ_{22}, a solution of (5.187) is only of approximate character. This is do to the fact that the equations of compatibility do not reduce to one single condition, as for plane strain, but consists of three additional conditions, reproduced below:

$$\varepsilon_{33,22} = 0 \tag{5.188}$$

$$\varepsilon_{33,11} = 0 \tag{5.189}$$

$$\varepsilon_{33,12} = 0 \tag{5.190}$$

These additional conditions are not fulfilled by the use of (5.187). According to Ugural and Fenster, the error introduced by the use of (5.187) is negligibly small for thin elements, thus justifying the use of the biharmonic equation for plane stress problems [5, p.102].

5.6 Closure

Selected topics of the general theory of elasticity have been derived in the above. In the following a brief exposition of the derived equations is made.

The derived theory can be divided into three categories, each containing a set of equations and unknowns. This is illustrated in figure 5.10.

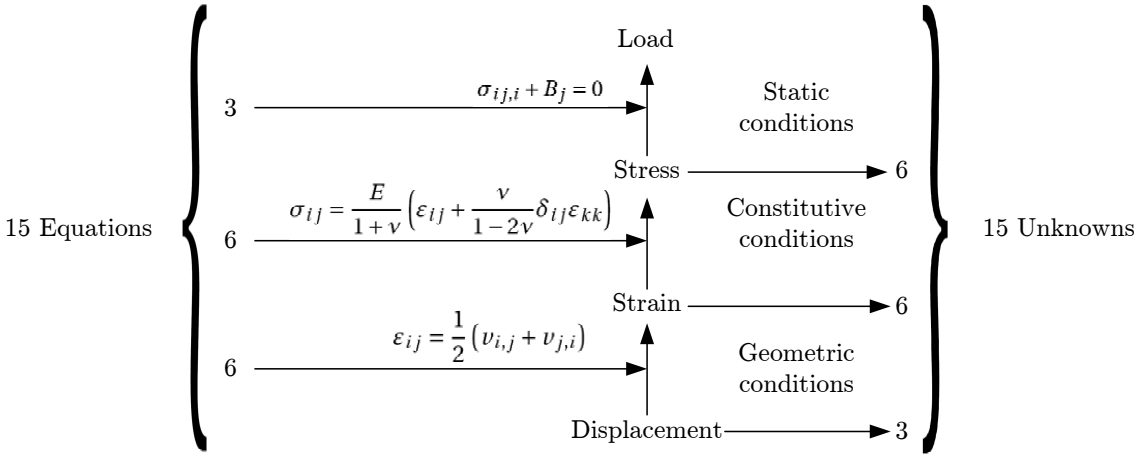

Figure 5.10: *Graphical representation of the linear theory of elasticity.*

The first category is the geometric conditions which are formulated by Cauchy's strain tensor. Here six equations are expressed on the basis of three displacements. There are two assumptions associated with Cauchy's formulation of the strain tensor. Small deformations, $ds \approx ds^*$, and small displacements, $v_{i,j}\, v_{j,i} \approx 0$.

The second category connects the strains to the stresses, which are formulated by Hooke's law. Here six equations describe six unknowns, either in the form of stresses or strains. Such relations between two physical quantities are generally referred to as constitutive conditions.

The third category consists of the equations of equilibrium, and are thus referred to as the static conditions. Here three equations connect the six stress components and body forces such that the point of interests is in equilibrium.

In total the linear theory of elasticity comprises 15 partial differential equations and 15 unknowns. Thus making it possible to solve a given problem for either forces or displacements. Although, solving for displacements on the basis of a strain field requires some restrictions in the form of the compatibility equations, as explained in section 5.2. In order to obtain a solution for the boundary value problem, the boundary conditions have to be prescribed. Here the condition of every point on the boundary is defined by either a known displacement, traction, or a combination of the two. Solving a practical problem by the use of the above formulations proves to be a tardy process, even by the use of simplified considerations, such as plane stress. Here the use of the biharmonic equation, described in section 5.5 can be used to simplify the process. Although solutions have mostly been archived for simple problems, such as the classic example of an infinite plate with a circular hole in the middle. These exact solutions are of great importance, because they can be used to verify results obtained by approximate calculation methods, such as the Finite Element Method.

Chapter

6

Estimation of Stresses in The Spanner Model

In the following the stress distribution in the spanner is estimated. As mentioned in section 4 the purpose of these estimates is to provide plausible results for evaluating results from measurements and FE analysis. It also provides an overview of areas which could be of interest in order to ensure the correctness of experimental results.

Figure 6.1 illustrates how the model is divided into four elements. Elements 1, 2, and 4 are selected for stress estimation and element 3 is black boxed since there is no adequate analytical solution method for such a geometry. The division of the model into these four elements is based on considerations about which areas are of most interest and where the analytical solution methods are best suited.

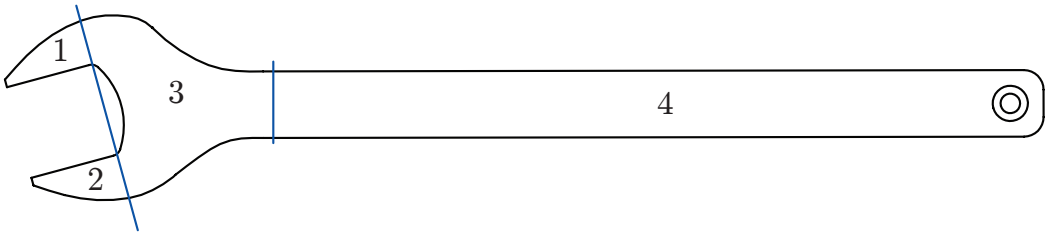

Figure 6.1: *The division of the spanner into four elements. Elements 1, 2, and 4 are selected for stress estimation analysis.*

The stress distribution in the shank, element 4, is estimated by means of Bernoulli-Euler beam theory. The jaws, elements 1 and 2, are treated by theory of elasticity due to the complex geometry.

6.1 Estimated Stresses in The Shank

The shank can be considered a long slender beam and therefore the Bernoulli-Euler beam theory applies. The expressions used in this section are adopted from Gere [6].
Figure 6.2 shows relevant points and dimensions of the spanner. Table 6.1 shows the associated dimensions. Assuming that the nut and sections 1,2, and 3 from figure 6.1 can be treated as a

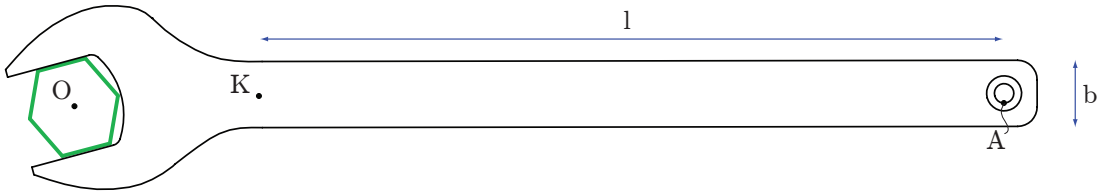

Figure 6.2: *Relevant points and dimensions of the spanner.*

l	b	w	
191	17	5	mm

Table 6.1: *Selected dimensions of the spanner.*

rigid body with no relative movement, the shank of the spanner can be modelled as a cantilever beam. This is sketched in figure 6.3.
The cantilever beam is assumed to start at point K. As stated in section 4 the spanner is subjected to a force of $100N$. The force P does not act at the centerline, but at the point A. It is assumed that P acts perpendicularly to the centerline. A free body diagram of the cantilever is also given in figure 6.3.

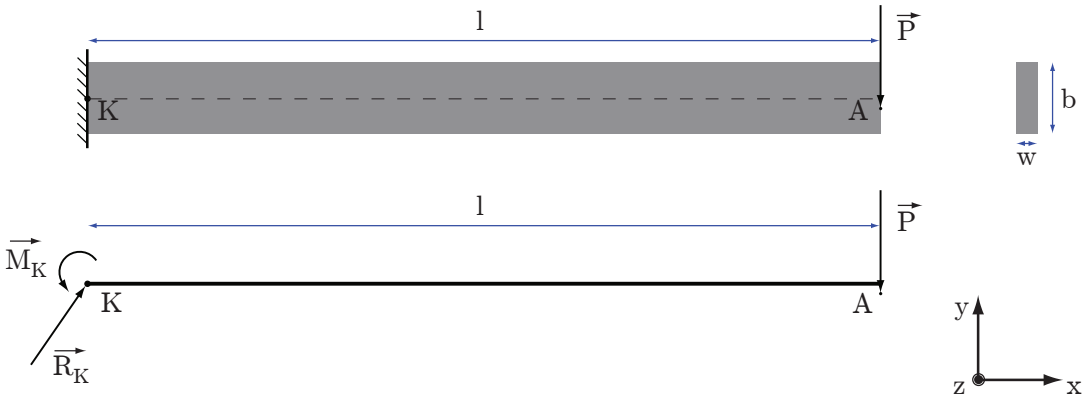

Figure 6.3: *Uppermost the beam model. Underneath the free body diagram.*

The equilibrium equations give the following reactions

$$\sum \vec{F} = \overrightarrow{R_K} + \overrightarrow{P} = \vec{0} \qquad \Rightarrow \tag{6.1}$$

$$\overrightarrow{R_K} = -\overrightarrow{P} = -\begin{bmatrix} 0 \\ -P_y \end{bmatrix} \tag{6.2}$$

$$\sum M = M_K + \overrightarrow{r} \rtimes \overrightarrow{P} = 0 \qquad \Rightarrow \tag{6.3}$$

$$M_K = -\overrightarrow{r} \rtimes \overrightarrow{P} = lP_y \tag{6.4}$$

where: $\rtimes$ The planar cross product operator. $\vec{a} \rtimes \vec{b} \equiv \left([\vec{a}^T, 0]^T \times [\vec{b}^T, 0]^T\right) \cdot [0,0,1]^T \ \forall \ \vec{a}, \vec{b} \in \mathbb{R}^2$.

The internal forces are determined by use of figure 6.4

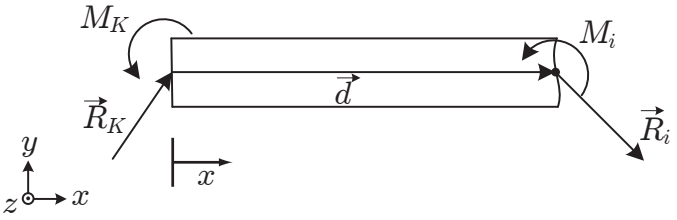

Figure 6.4: *Section cut of the cantilever beam.*

$$\sum \vec{F} = \vec{F}_i + \vec{R}_K = \vec{0} \quad \Rightarrow \tag{6.5}$$

$$\vec{F}_i = -\vec{R}_K = \begin{bmatrix} 0 \\ -P_y \end{bmatrix} \tag{6.6}$$

$$\sum M = M_i + M_K - \vec{d} \times \vec{R}_K = 0 \quad \Rightarrow \tag{6.7}$$

$$M_i = -M_K + \vec{d} \times \vec{R}_K = -lP_y + xR_{Ky} \tag{6.8}$$

where: R_{Ky} The y-component of $\vec{R}_K$.

As seen by equations (6.6) and (6.8) the transverse loading induces shear- and bending stresses in the shank. The bending moment varies linearly along the length of the spanner and the transverse loading is constant from point A to K. It is thus favourable to place strain gauges near the end of the shank, in order to get a higher read out from the gauges. Three sections on the shank have been selected as suitable locations, these are illustrated in figure 6.5, and the associated dimensions are listed in table 6.2.

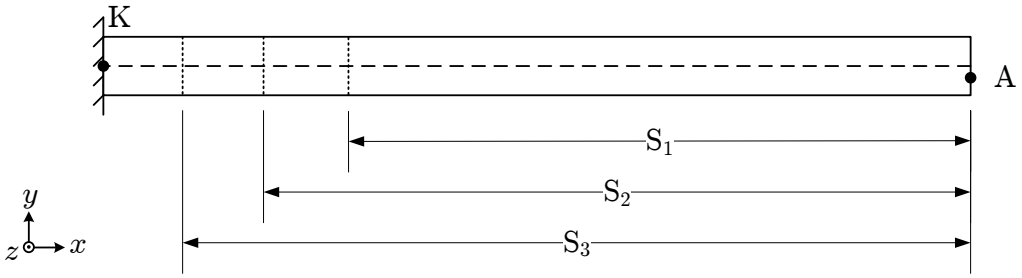

Figure 6.5: *Location of strain gauge sections on shank.*

S_1	S_2	S_3	
141.5	161.5	181.5	mm

Table 6.2: *Distances to strain gauge section from point A.*

From equations (6.6) and (6.8) the bending moment and shear force are determined at the strain gauge sections. The results are listed in table 6.3.

	K	S_1	S_2	S_3	
F_{iy}	100	100	100	100	N
M_i	19100	14150	16150	18150	Nmm

Table 6.3: *Bending moment and shear load at differen cross section.*

6.1.1 Stress Distribution

In the following the stress distribution for the section at point K is determined. The distributions of sections S_1, S_2, and S_3 calculated equivalently and are thus listed at the end of the section.
In accordance with the elementary beam theory the shear stresses can be calculated as

$$\tau_{xy} = \frac{F_{iy} Q}{I_z w} \tag{6.9}$$

where: Q The moment area. For a rectangular cross section $Q = \frac{w}{2}\left(\frac{b^2}{4} - y^2\right)$.

I_z The moment of inertia about the z-axis. For a rectangular cross section $I_z = \frac{b^3 w}{12}$.

For a rectangular cross section the shear stresses become

$$\tau_{xy} = \frac{F_{iy}}{2I_z}\left(\frac{b^2}{4} - y^2\right) \tag{6.10}$$

Figure 6.6 shows the shear stress distribution over the cross section of the beam. As expected the shear stresses vary parabolically over the cross section with the largest stresses in the centre of the cross section. Because the transverse loading is constant throughout the length of the shank, the shear stress are equal in every cross section.

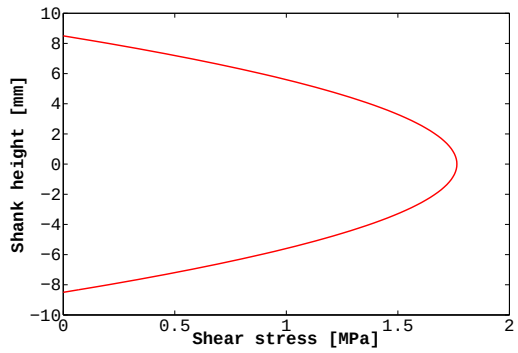

Figure 6.6: *Shear stress distribution at an arbitrary cross section of the shank.*

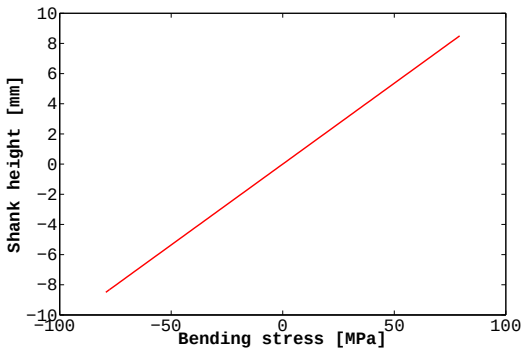

Figure 6.7: *Bending stress at cross section K.*

The bending stresses are calculated as

$$\sigma_x = -\frac{M_i y}{I_z} \tag{6.11}$$

Since the cross section of the beam does not vary the largest bending stresses must occur at cross section K. Figure 6.7 illustrates the distribution of bending stresses over the cross section K. The bending stresses vary linearly over the cross section as expected, with the largest stresses at the outer fibres.
The stress tensor for cross section K can thus be expressed as

$$\sigma_{ij}(y) = \begin{pmatrix} \sigma_x(y) & \tau_{xy}(y) & 0 \\ \tau_{xy}(y) & 0 & 0 \\ 0 & 0 & 0 \end{pmatrix} = \begin{pmatrix} \frac{-M_i y}{I_z} & \left(\frac{F_{iy}}{2I_z}\left(\frac{b^2}{4} - y^2\right)\right) & 0 \\ \left(\frac{F_{iy}}{2I_z}\left(\frac{b^2}{4} - y^2\right)\right) & 0 & 0 \\ 0 & 0 & 0 \end{pmatrix} \tag{6.12}$$

For comparison purposes the von Mises stress is calculated, which for cross section K is given as

$$\sigma' = \sqrt{{\sigma_x}^2 + {\sigma_y}^2 - \sigma_x\sigma_y + 3\tau_{xy}^2} \tag{6.13}$$

$$= \sqrt{{\sigma_x}^2 + 3\tau_{xy}^2} \tag{6.14}$$

This gives a distribution as shown in figure 6.8.

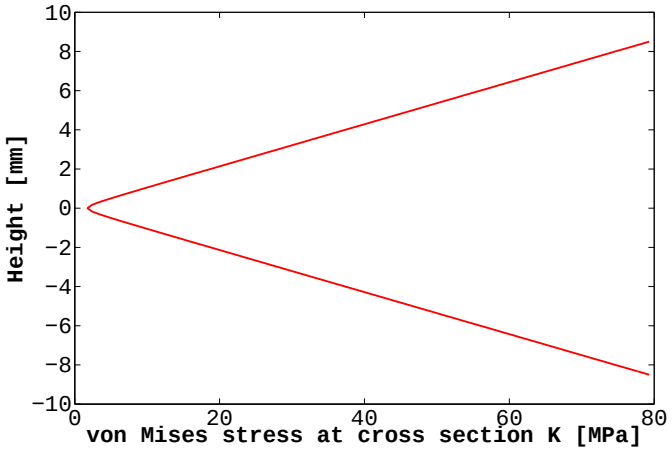

Figure 6.8: *Von Mises stresses at cross section K.*

	K	S1	S2	S3	
σ_x	79.3	58.8	67.1	75.4	MPa
τ_{xy}	1.8	1.8	1.8	1.8	MPa

Table 6.4: *Bending- and shear stresses at different cross sections of the shank.*

6.2 Estimated Stresses in The Jaws

As the geometry of the jaws does not correspond to a long slender beam, stresses found the Bernoulli-Euler beam theory is not expected to be accurate. Instead application of methods from theory of elasticity is used to give a satisfactory estimate of the stress distribution.
First the boundary conditions are examined. These are seen in figure 6.9. The figure consists of two illustrations. The upper part shows the applied force P and how the spanner is supported and in the lower part the free body diagrams are shown. The upper jaw is assumed to be simply supported whereas the lower jaw is assumed to have a frictionless simple support.
It is assumed that $\vec{F}_1$ acts perpendicularly to the surface though it is not modelled as a frictionless support. The nature of the support does, however, induce a friction component $\vec{R_{P,x_2}}$ due

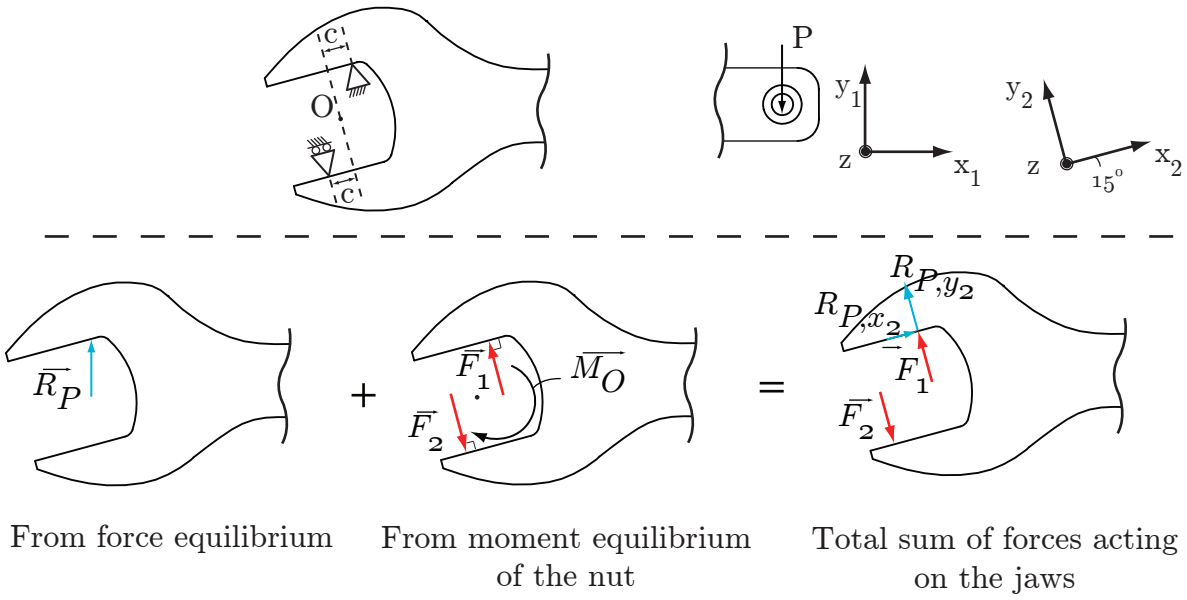

Figure 6.9: *The free body diagram for the jaws.*

to the force equilibrium and its normal component $R_{\vec{P},y_2}$. Force equilibrium gives:

$$\sum \vec{F} = \vec{R_P} + \vec{P} = \vec{0} \quad \Rightarrow \quad (6.15)$$

$$\vec{R_P} = -\vec{P} \quad \Rightarrow \quad (6.16)$$

$$\vec{R_{P,2}} = \begin{bmatrix} R_{P,x_2} \\ R_{P,y_2} \end{bmatrix} = \begin{bmatrix} R_P \cdot \sin(15°) \\ R_P \cdot \cos(15°) \end{bmatrix} \quad (6.17)$$

The moment about point O is determined as:

$$\sum M = M_O + \overrightarrow{OA} \times \vec{P} = 0 \quad \Rightarrow \quad (6.18)$$

$$M_O = -\overrightarrow{OA} \times \vec{P} \quad \Rightarrow \quad (6.19)$$

$$|\vec{F}_1| = \frac{M_O}{2c} \quad (6.20)$$

where: $|\vec{F}_1|$ The length of vector $\vec{F}_1$ from figure 6.9.

The perpendicular distance to point O from the contact point of both $\vec{F}_1$ and $\vec{F}_2$ is assumed to be c as seen in figure 6.9 and so $\vec{F}_1 = \vec{F}_2$. In reality some variation due to geometrical deviation and tolerances may occur. However, this is neglected. The force pair $\vec{F}_1$ and $\vec{F}_2$ are thus given as:

$$\vec{F}_1 = \begin{bmatrix} F_1 \cdot \cos(15° + 90°) \\ F_1 \cdot \sin(15° + 90°) \end{bmatrix}, \vec{F}_2 = \begin{bmatrix} F_1 \cdot \cos(15° - 90°) \\ F_1 \cdot \sin(15° - 90°) \end{bmatrix} \quad (6.21)$$

The geometry of the jaws can by good approximation be compared to that of a wedge. In the theory of elasticity there are solutions for the case of concentrated loads on a semi-infinite wedge with unit thickness. These can be found by use of Airy's stress function as described in section 5.5 applying the semi-inverse method. Finding solutions by the semi-inverse method requires a partial solution, a stress function, where only constant coefficients need to be determined. The stress functions are assumed from earlier known solutions of plane stress. As the thickness of the spanner is small and the loads in-plane the assumptions of plane stress are

assumed to be reasonable. The approach of solution is that the the unknown constant coefficients must ensure equilibrium. Furthermore, the stress function must satisfy the biharmonic equation in order to ensure compatibility. As described in section 5.5 the biharmonic equation does not completely ensure compability for plane stress, but as the thickness of the spanner is small the error is believed to be insignificant. The geometry of a wedge can with advantage be described by polar coordinates. The biharmonic equation in polar coordinates is given by Ugural and Fenster as [5, p.116]:

$$\nabla^4\Phi = \left(\frac{\partial^2}{\partial r^2} + \frac{1}{r}\frac{\partial}{\partial r} + \frac{1}{r^2}\frac{\partial^2}{\partial\theta^2}\right)\left(\nabla^2\Phi\right) = 0 \tag{6.22}$$

Figure 6.11 shows the convention of polar coordinates on the wedge.
The equations of equilibrium in polar coordinates can be found by considering the basic relations between polar coordinates and Cartesian coordinates and then expressing derivatives with respect to x and y in polar coordinates applying the chain rule. The equilibrium equations in polar coordinates will then yield [5, p.113]:

$$\frac{\partial\sigma_r}{\partial r} + \frac{1}{r}\frac{\partial\tau_{r\theta}}{\partial\theta} + \frac{\sigma_r - \sigma_\theta}{r} + F_r = 0 \tag{6.23}$$

$$\frac{1}{r}\frac{\partial\sigma_\theta}{\partial\theta} + \frac{\partial\tau_{r\theta}}{\partial r} + \frac{2\tau_{r\theta}}{r} + F_\theta = 0 \tag{6.24}$$

In the absence of body forces equation (6.23) and (6.24) are satisfied by a stress function $\Phi(r,\theta)$ analogous to what is described in 5.5 and the stress components in radial and tangential directions are given as:

$$\sigma_r = \frac{1}{r}\frac{\partial\Phi}{\partial r} + \frac{1}{r^2}\frac{\partial^2\Phi}{\partial\theta^2} \tag{6.25}$$

$$\sigma_\theta = \frac{\partial^2\Phi}{\partial r^2} \tag{6.26}$$

$$\tau_{r\theta} = \frac{1}{r^2}\frac{\partial\Phi}{\partial\theta} - \frac{1}{r}\frac{\partial^2\Phi}{\partial r\partial\theta} \tag{6.27}$$

These radial and tangential stresses can be transformed into stresses expressed in Cartesian coordinates using the transformation equations:

$$\sigma_x = \sigma_r\cos^2(\theta) + \sigma_\theta\sin^2(\theta) - 2\tau_{r\theta}\sin(\theta)\cos(\theta) \tag{6.28}$$

$$\sigma_y = \sigma_r\sin^2(\theta) + \sigma_\theta\cos^2(\theta) + 2\tau_{r\theta}\sin(\theta)\cos(\theta) \tag{6.29}$$

$$\tau_{xy} = (\sigma_r - \sigma_\theta)\sin(\theta)\cos(\theta) + \tau_{r\theta}(\cos^2(\theta) - \sin^2(\theta)) \tag{6.30}$$

6.2.1 Stresses in The Lower Jaw

The approach in the following for determination of the stress distribution is adopted from Ugural and Fenster [5]. Initially the jaw is modelled as a wedge and the loading is transformed into statically equivalent scenarios for which analytical solutions exist. Figure 6.10 shows how this is been done. The load is moved to the tip of the wedge and in doing so a moment needs to be applied about the tip. This moment must be:

$$M_{tip} = -\vec{s}_{tip} \times \vec{F}_2 \tag{6.31}$$

where: $\vec{s}_{tip}$ The vector $[s_{tip}, 0, 0]^T$.

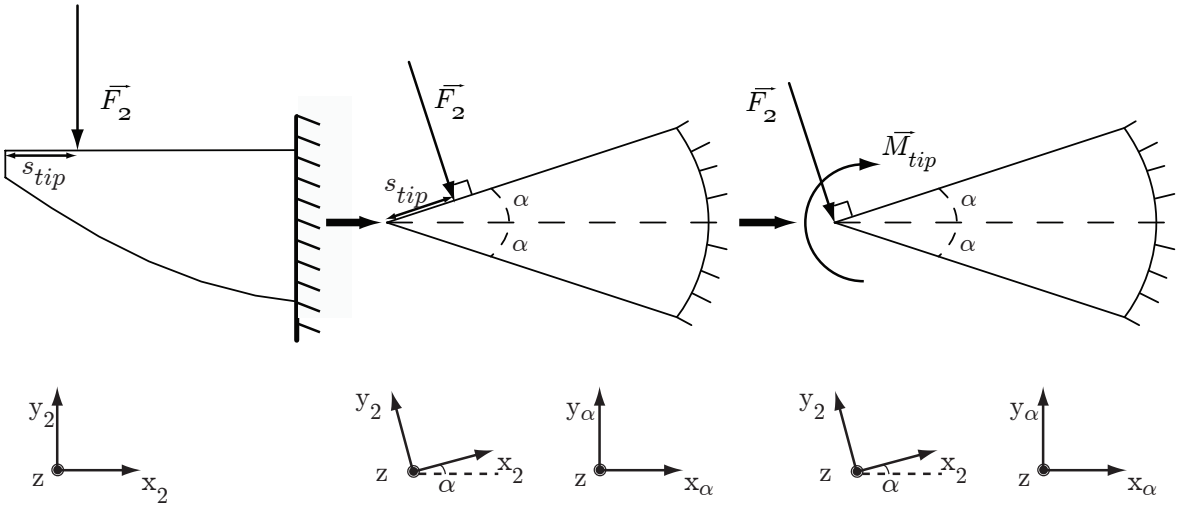

Figure 6.10: *The jaw modelled as a wedge. The loading is transformed to a statically equivalent scenario for which known solutions exist.*

s_{tip} is determined in section 7.1.3 to be $0.5mm$ for the lower jaw and $12mm$ for the upper jaw.
In the theory of elasticity there are known stress functions for the cases of a wedge in compression, bending, or pure bending. Thus the loading shown in figure 6.10 is divided into these three scenarios as shown in figure 6.11.

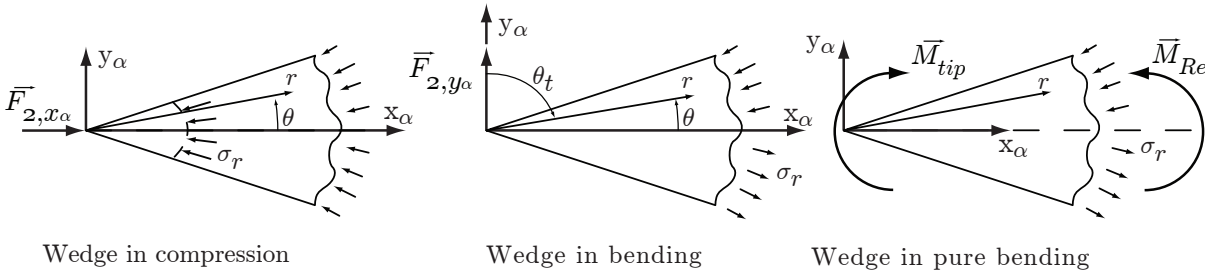

Figure 6.11: *The three scenarios compression, bending, and pure bending for which known stress functions exist. It is important to note that F_{2,x_α} and F_{2,y_α} are per unit thickness forces.*

6.2.1.1 Wedge In Compression

In the case of compression the following stress function is assumed [5, p.118]:

$$\Phi = cF_{2,x_\alpha} r\theta \sin(\theta) \tag{6.32}$$

where: F_{2,x_α} The x_α-component of $\vec{F}_2$. Note that the forces are per unit thickness.

From the equilibrium equations (6.25), (6.26), and (6.27) the stresses in radial and tangential directions are:

$$\sigma_r = 2cF_{2,x_\alpha}\frac{\cos(\theta)}{r} \quad , \quad \sigma_\theta = \tau_{r\theta} = 0 \tag{6.33}$$

The constant c is determined by use of the boundary conditions $\sigma_\theta(\theta = \pm\alpha) = \tau_{r\theta}(\theta = \pm\alpha) = 0$ and force equilibrium. $\sigma_\theta(\theta = \pm\alpha) = 0$ and $\tau_{r\theta}(\theta = \pm\alpha) = 0$ are already satisfied by (6.33).

Force equilibrium must be satisfied in every cross section of the wedge. This yields:

$$-F_{x_\alpha} = \sigma_r \cdot C_r \qquad \Rightarrow \tag{6.34}$$

$$-F_{x_\alpha} = 2\int_0^\alpha (\sigma_r \cos(\theta))\, r\, d\theta \tag{6.35}$$

where: C_r The length of the polar cross section line at radius r.

Substituting the expression for σ_r into the equilibrium equation (6.35) yields:

$$-F_{x_\alpha} = 4cF_{x_\alpha}\int_0^\alpha \cos^2(\theta)\, d\theta \tag{6.36}$$

$$= 4cF_{x_\alpha}\left(\frac{\sin(\alpha)\cos(\alpha)}{2} - \frac{\sin(0)\cos(0)}{2} + \frac{\alpha}{2} - \frac{0}{2}\right) \tag{6.37}$$

$$= 4cF_{x_\alpha}\left(\frac{1}{4}\sin(2\alpha) + \frac{\alpha}{2}\right) \tag{6.38}$$

$$= cF_{x_\alpha}\sin(2\alpha) + 2\alpha \qquad \Rightarrow \tag{6.39}$$

$$c = \frac{-1}{\sin(2\alpha) + 2\alpha} \tag{6.40}$$

Substituting equation (6.40) into the equilibrium equation (6.33) yields:

$$\sigma_{r,comp} = -\frac{F_{2,x_\alpha}\cos(\theta)}{r(\frac{1}{2}\sin(2\alpha) + \alpha)} \quad , \quad \sigma_{\theta,comp} = \tau_{r\theta,comp} = 0 \tag{6.41}$$

From equation (6.41) it is seen that the largest radial stress in any cross section occur at the centerline because the term $\cos(\theta)$ has its maximum at $\theta = 0$. It is also seen that σ_r goes to infinity as r approaches zero. From this it follows that the solution is incorrect close to the tip where the load is inserted.

6.2.1.2 Bending of Wedge Due to Transverse Loading

In the following the same stress function (6.32) as for compression is assumed but the angle used is changed to $\theta_t = \frac{\pi}{2} - \theta$ see figure 6.11. The constant c is determined using the same boundary conditions $\sigma_\theta(\theta = \pm\alpha) = \tau_{r\theta}(\theta = \pm\alpha) = 0$ where the only condition not already satisfied is the force equilibrium.
The equilibrium equation is described as:

$$-F_{y_\alpha} = \int_{\frac{\pi}{2}-\alpha}^{\frac{\pi}{2}+\alpha} (\sigma_r \cos(\theta_t))\, r\, d\theta_t \tag{6.42}$$

$$= 2cF_{y_\alpha}\int_{\frac{\pi}{2}-\alpha}^{\frac{\pi}{2}+\alpha} \cos^2(\theta_t)\, d\theta_t \qquad \Rightarrow \tag{6.43}$$

$$c = \frac{-1}{2\alpha - \sin(2\alpha)} \tag{6.44}$$

The stress function and the expression $\theta_t = \frac{\pi}{2} - \theta$ gives the following stress components:

$$\tau_{r\theta,trans} = \sigma_{\theta,trans} = 0\,, \qquad \text{and} \tag{6.45}$$

$$\sigma_{r,trans} = -\frac{F_{y_\alpha}\cos(\theta_t)}{r(2\alpha - \frac{1}{2}\sin(2\alpha))} = -\frac{F_{y_\alpha}\sin(\theta)}{r(2\alpha - \frac{1}{2}\sin(2\alpha))} \tag{6.46}$$

From equation (6.46) it is seen that the largest radial stresses occur at $\theta = \alpha$. The expression also shows that if $\theta_t > \frac{\pi}{2}$ the expression becomes positive thus tension exist in the upper half of the wedge and compression in the lower half.

6.2.1.3 Pure Bending of Wedge

For the case of pure bending the following stress function is assumed [5, p. 141]:

$$\Phi = -\frac{1}{2}\frac{M_{tip}(\sin(\theta) - 2\theta\cos(2\alpha))}{\sin(2\alpha) - 2\alpha\cos(2\alpha)} \tag{6.47}$$

Equation (6.47) satisfies the biharmonic equation $\nabla^4\Phi = 0$ and thus ensures compatibility. The approach used is the inverse method. Hence no coefficients are to be determined. From the equilibrium equations (6.25), (6.26), and (6.27) the stresses in radial and tangential directions are:

$$\sigma_{r,bend} = \frac{2M_{tip}\sin(2\theta)}{r^2(\sin(2\alpha) - 2\alpha\cos(2\alpha))} \tag{6.48}$$

$$\tau_{r\theta,bend} = \frac{M_{tip}(2\cos(2\theta) - 2\cos(2\alpha))}{r^2(\sin(2\alpha) - 2\alpha\cos(2\alpha))} \tag{6.49}$$

$$\sigma_{\theta,bend} = 0 \tag{6.50}$$

The boundary conditions are implicitly satisfied by equations (6.48) through (6.50).

6.2.1.4 Superposition of the Three General Scenarios

The total distribution of stresses in the wedge can now be found by superposing the polar stresses determined for each of the three scenarios. That is:

$$\sigma_{r,tot}(r,\theta) = \sigma_{r,comp} + \sigma_{r,trans} + \sigma_{r,bend} \tag{6.51}$$

$$= -\frac{F_{2,x_\alpha}\cos(\theta)}{r(\frac{1}{2}\sin(2\alpha) + \alpha)} - \frac{F_{y_\alpha}\sin(\theta)}{r(2\alpha - \frac{1}{2}\sin(2\alpha))} + \frac{2M_{tip}\sin(2\theta)}{r^2(\sin(2\alpha) - 2\alpha\cos(2\alpha))} \tag{6.52}$$

$$\tau_{r\theta,tot}(r,\theta) = \tau_{r\theta,comp} + \tau_{r\theta,trans} + \sigma_{r\theta,bend} \tag{6.53}$$

$$= 0 + 0 + \frac{M_{tip}(2\cos(2\theta) - 2\cos(2\alpha))}{r^2(\sin(2\alpha) - 2\alpha\cos(2\alpha))} \tag{6.54}$$

$$\sigma_{\theta,tot}(r,\theta) = \tau_{\theta,comp} + \tau_{\theta,trans} + \tau_{\theta,bend} \tag{6.55}$$

$$= 0 + 0 + 0 \tag{6.56}$$

These stresses are now transformed into cartesian coordinates (x_α, y_α) using equations (6.28) through (6.30). Next, the stresses are rotated back into the (x_2, y_2) coordinate system. This is done using the equations for rotation of a tensor:

$$\sigma_{x,2} = \frac{(\sigma_{x,\alpha} + \sigma_{y,\alpha})}{2} + \frac{(\sigma_{x,\alpha} - \sigma_{y,\alpha})}{2\cos(2\alpha)} + \tau_{xy,\alpha}\sin(2\alpha) \tag{6.57}$$

$$\sigma_{y,2} = \frac{(\sigma_{x,\alpha} + \sigma_{y,\alpha})}{2} - \frac{(\sigma_{x,\alpha} - \sigma_{y,\alpha})}{2\cos(2\alpha)} - \tau_{xy,\alpha}\sin(2\alpha) \tag{6.58}$$

$$\tau_{xy,2} = -\frac{(\sigma_{x,\alpha} - \sigma_{y,\alpha})}{2\sin(2\alpha)} + \tau_{xy,\alpha}\cos(2\alpha) \tag{6.59}$$

By use of the above calculations and transformations the stresses can be calculated for a wedge subjected to the three loading scenarios. However, as seen in figure 6.10 the geometry of the jaws have some deviations from the geometry of a triangular wedge. In order to give a better estimation of the stress state in the jaw, the geometry is divided into a series of wedges of different sizes. The principle is illustrated in figure 6.12. The curved geometry of the jaw is fitted to a polynomial using natural cubic splines. Each wedge is described by a circular cross section

with constant radius ranging from the straight face to the curved face. The stresses are now evaluated at the end of each wedge. As the radii increases, with each new wedge in the series, the obtained results is assumed to describe the specific cross section of the jaw.
Numerically the points in which the stress state is evaluated are defined by the concept sketched in figure 6.13, where each cross denotes a point. The precision of the total result thus depends on the number of points in the net.

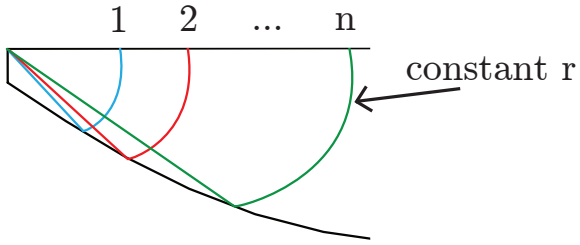

Figure 6.12: *The principle of how the jaw is formed by a series of wedges.*

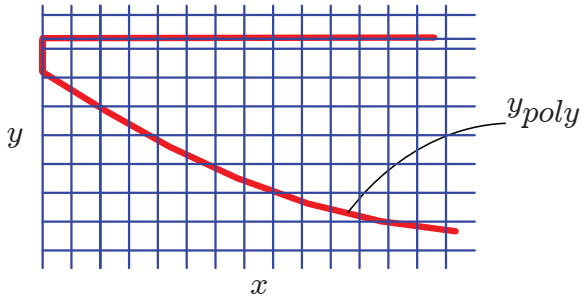

Figure 6.13: *The principle of how the stresses are calculated in the jaw.*

In order to give a view of the normal stresses along the edge of the geometry, the $\sigma_{x,2}$ and $\sigma_{y,2}$-stresses are presented in the following by plots produced in the manner described above. Complementary to this the $\tau_{xy,2}$ stresses are plotted. The magnitudes on the axes are expressed in mm for x and MPa for y in for stresses. As shown in equation (6.41) the stress distribution is incorrect near the tip of the wedge and therefore the plots do not show the tip of the jaw where the load is inserted. The stress distribution for σ_{x2} is illustrated in figure 6.14. The stresses

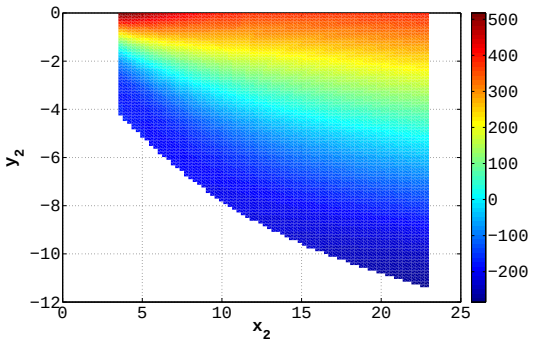

Figure 6.14: *The stress distribution for $\sigma_{x,2}$.*

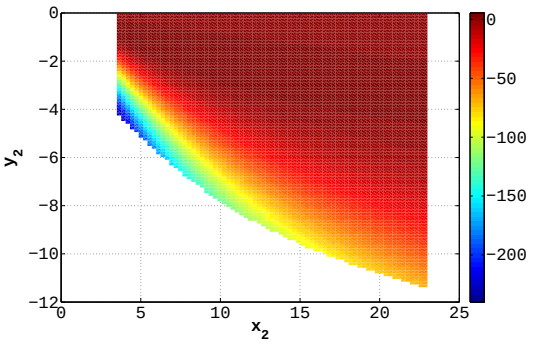

Figure 6.15: *The stress distribution for $\sigma_{y,2}$.*

range from compressive stresses of approximately $-280\,MPa$ on one edge to tensile stresses of approximately $500\,MPa$ on the other edge. Although stresses are not symmetric in size, the graph show that they are closely symmetric around the centerline of the jaw, which was expected. Figure 6.15 shows the $\sigma_{y,2}$ stresses. These should not exist, however, the plot shows that the outer edge of the jaw is in compression, while large parts of the top of the jaw are zero, as expected. The τ_{xy} distribution is shown in figure 6.16. The τ_{xy} shear stresses range from -37 to 200 MPa. As can be seen from the figure, stress distribution does not reassemble the familiar parabolic shape known from the classic Bernoulli-Euler beam theory. Due to this the results does not seam credible, and results obtained from other methods are not expected to show this tendency.

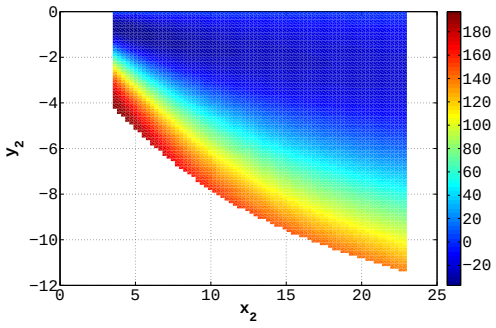

Figure 6.16: *The stress distribution for $\tau_{xy,2}$.*

Because only the $\sigma_{x,2}$ stresses gave expected results, while $\sigma_{y,2}$ had some parts with the correct values, and $\tau_{xy,2}$ gave unexpected results, it is desired to compare these solutions with analytical solutions from elementary beam theory.

6.2.1.5 Solution by Bernoulli-Euler Beam Theory

Figure 6.17 shows how the jaw is modelled as a triangular beam exerted to a transverse loading and pure bending. The triangle is made such that it has the same hight as the actual jaw at the support end, and where the loads attack. Because of this, the tip of the complete triangle extends the geometry of the jaw. The tip is marked with the dashed lines. The part of the triangle which is subjected to the loads is marked with gray. The contour of the actual jaw is marked with the spaced dashed line. The case of transverse loading give the following bending

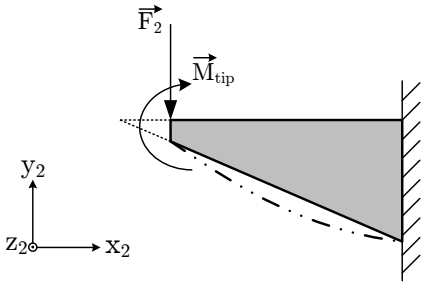

Figure 6.17: *The jaw modelled as a triangular beam.*

stresses:

$$\sigma_{x,2,t} = \frac{-M_t \cdot y_{tri}(x_2)}{I_z(x_2)} \tag{6.60}$$

where:

$\sigma_{x,2,t}$	The normal bending stresses from the transverse loading.
M_t	The internal moment due to the transverse loading.
$y_{tri}(x_2)$	The vertical distance from the centerline of the triangle to the point of stress calculation.
$I_z(x_2)$	The moment of inertia about the z-axis for a given x_2-coordinate.

The moment of inertia is calculated over given heights of the triangle corresponding to a x_2-coordinate. That is:

$$I_z(x_2) = \frac{b \cdot h(x_2)^3}{12} \tag{6.61}$$

where: b The width of the triangle.

$h(x_2)$ The given height of the triangle at a given x_2-coordinate.

The shear stresses due to the transverse loading are given as:

$$\tau_{xy,2,t} = \frac{V_t \cdot Q(x_2)}{I_z(x_2) \cdot b} \tag{6.62}$$

where: V_t The internal shear force due to the transverse loading.

$Q(x_2)$ The first moment of the triangle for a given x_2-coordinate.

The first moment $Q(x_2)$ is calculated using the same approach as for $I_z(x_2)$. That is [6, p. 350]:

$$Q(x_2) = \frac{b}{2} \cdot \left(\frac{h(x_2)^2}{4} - y_{tri}(x_2)^2 \right) \tag{6.63}$$

The bending stresses due to the pure bending scenario $\sigma_{x,2,b}$ are calculated as $\sigma_{x,2,t}$ using expression (6.60). Figure 6.18 illustrates the sum of bending stresses $\sigma_{x,2,b}$+$\sigma_{x,2,t}$ over the triangles geometry. The tip of the triangle is not shown in the figure since the stress distribution here is not considered plausible.

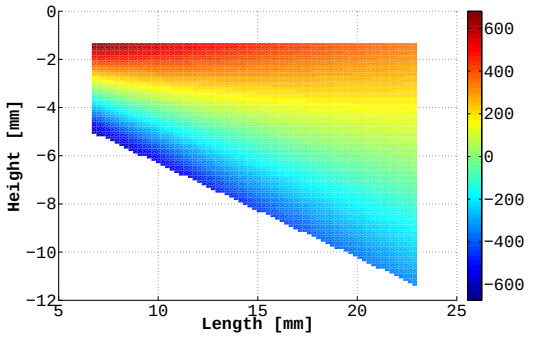

Figure 6.18: *The distribution of the bending stresses in the triangle.*

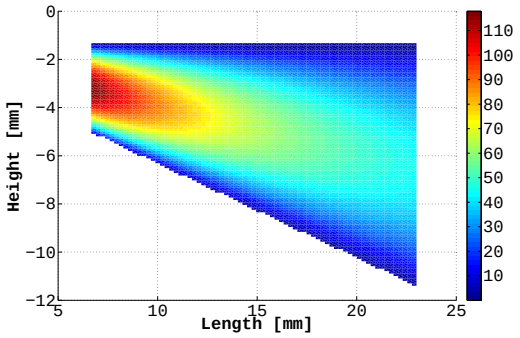

Figure 6.19: *The stress distribution for the shear stress $\tau_{xy,2,t}$ in the triangle.*

From figure 6.18 it is seen that the bending stresses vary linearly in every cross section as expected. The bending stresses vary from approximately $-670\,MPa$ to $670\,MPa$. The shear stress in the triangle is shown in figure 6.19. The shear stresses vary parabolically over the cross sections of the triangle as expected and vary from zero to $118\,MPa$.

6.2.1.6 Summarising The Results For the Lower Jaw

If normal stresses along the edge are compared for the two methods of stress determination, that is, if $\sigma_{x,2}$-stresses from the theory of elasticity are compared to $\sigma_{x,2}$-stresses from the

Bernoulli-Euler beam theory, a clear resemblance is seen. The two distributions both vary (approximately) linear along a cross section giving tension on one side and compression on the other side. The $\sigma_{x,2}$ stresses in tension obtained by the Bernoulli-Euler beam theory are approximately 25% higher the of the stresses obtained by theory of elasticity. Whereas the difference in compression of approximately 60 %. The differences are explained by larger dimensions of the cross sections of the wedge models. Thus the lower values obtained by the wedge models seem reasonable.
Comparing the shear stresses obtained from the two approachers, it can be concluded that the results obtained from beam theory have the correct parabolic distribution. The results obtained from the wedge models have a different distribution, and the values are off by a factor of two. Also the wedge models give negative stresses, which are not present in the results from the beam theory.
As a result the normal stresses obtained from the from theory of elasticity approach are believed to be the most accurate of the two methods. Where as the $\sigma_{y,2}$ and shear stresses have unreasonable values, and are thus neglected. Thus the shear stress distribution from the elementary beam theory is to be used when comparing results from the finite element model.

6.2.2 Stresses in The Upper Jaw

The stresses in the upper jaw are calculated using the same approach as for the lower jaw. The only difference is the superposing of transverse and compressive forces, as the difference shown in figure 6.9 is present. Therefore, no expressions of the stresses are derived in the following as these are similar to that of the lower jaw. However, the results are presented in the form of the von Mises stress distribution, see figure 6.20. The stresses are only plotted from the point of force insertion.

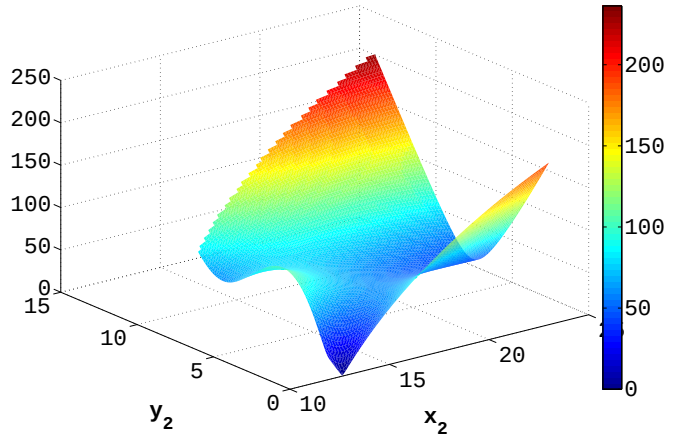

Figure 6.20: *The von Mises stress distribution over the upper jaw.*

Since the forces on the upper jaw do not act close to the tip, the wedge model is less accurate. As a consequence the results are considered less accurate. I.e. the verification and comparison with results from experiments and FEA are not expected to have as great value and importance as the results for the lower jaw.

Chapter

7

Introduction to Measurements

In order to verify the estimated stresses in the spanner and to be able to establish a foundation that can serve as verification of the FE analysis, quantitative measurements need to be carried out. As described in chapter 4, the methods used for the measurements are Strain Gauges and Digital Image Correlation. The associated theory and results are presented in chapter 8 and chapter 9, respectively.

In chapter 6 the stresses in the spanner were estimated using an analytical approach with an applied force of 100 N. During the measurements 100 N is set as the maximum load for comparison reasons. In the following chapter, the experimental setup is presented.

7.1 Measurement Setup

The equipment used to conduct the measurements has to fulfil certain specification requirements, in order to secure that the load insertions in the experiments are correspondent with those modelled in the analytical stress calculations described in sections 6.1 and 6.2.
The requirements for the equipment are:

- The setup must be able to replicate the analytical boundary conditions.
- The setup has to be rigid enough to ensure that the load angle is maintained throughout the experiment.
- The setup must ensure that the load is inserted in-plane on the spanner such that a plane stress situation is obtained.

The experimental setup consists of four main parts, a frame, load unit, fixture, and a model nut. In figure 7.1 the setup is shown with component highlighting. Figure 7.2 shows the setup in isometric view. In the following the parts are described along with how they ensure that the above requirements are met.

7.1.1 Frame

The frame serves as the base, on which the load unit and fixture with the model nut can be mounted. It consists of eight steel angle profiles, which are tightened together to form two upright sides, a top, and a bottom piece. The dimension of the angle profiles are $50 \cdot 50 \cdot 5mm$.

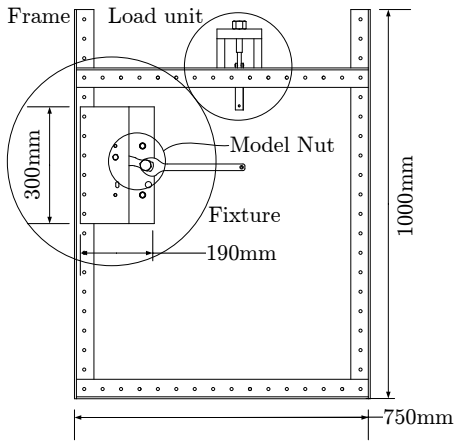

Figure 7.1: *The experimental setup consists of four main components.*

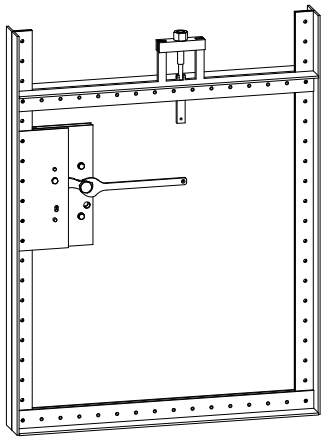

Figure 7.2: *Isometric view of experimental setup.*

Figure 7.1 shows the dimensions of the frame. The deflection of the frame during measurements influences the load angle on the spanner. If the top elements are modelled as a set of simply supported beams, as shown in figure 7.3, the maximum deflection and angular rotation at point S can be obtained by using Castigliano's second theorem [7, p.148]

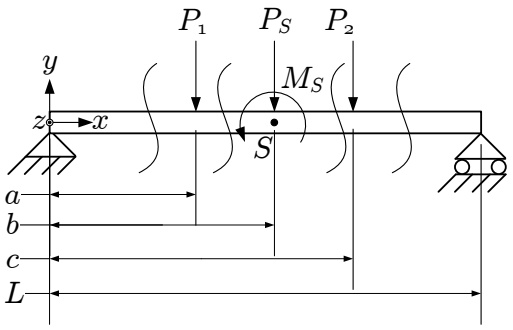

$a = 377.5mm$
$b = 424mm$
$c = 472.5mm$
$L = 750mm$
$P_1 = 50N$
$P_2 = 50N$
Fictionous force, $P_S = 0N$
Fictionous moment, $M_S = 0Nm$

Figure 7.3: *The top part of the frame can be analysed as a simply supported beam.*

$$\Delta_i = \frac{\partial U^*}{\partial Q_i} \tag{7.1}$$

where: Δ_i Generalised displacement.
U^* Total complementary energy.
Q_i System of loads at point i.

The total complementary energy for the system is determined by

$$U^* = \int \frac{(M(x))^2}{2EI}\, dx \tag{7.2}$$

Where $M(x)$ is the internal moment reaction of the structure. The structure is cut according to

figure 7.3. The moment function for the different cut sections are:

$$M_1(x) = R_0 x \qquad 0 \le x \le a \tag{7.3}$$
$$M_2(x) = R_0 x - P_1(x-a) \qquad a \le x \le b \tag{7.4}$$
$$M_3(x) = R_0 x - P_1(x-a) - P_s(x-b) - M_s \qquad b \le x \le c \tag{7.5}$$
$$M_4(x) = R_0 x - P_1(x-a) - P_s(x-b) - M_s - P_2(x-c) \qquad c \le x \le L \tag{7.6}$$

where: R_0 Reaction force at x equal to zero.

Using the above expressions the total complementary energy for the system is formulated as

$$U^* = \int_0^a \frac{(M_1(x))^2}{2E2I}\,dx + \int_a^b \frac{(M_2(x))^2}{2E2I}\,dx + \int_b^c \frac{(M_3(x))^2}{2E2I}\,dx + \int_c^L \frac{(M_4(x))^2}{2E2I}\,dx \tag{7.7}$$

where: E Young's modulus, $E = 210GPa$.

I Area moment of inertia for one angle profile, $I = 194740mm^4$.

From (7.7) the deflection and angular rotation can be obtained. The complete calculation can be found as a Maple-file in appendix C.1.

$$\Delta_S = \frac{\partial U^*}{\partial P_s} = 0.0030mm \tag{7.8}$$
$$\alpha_S = \frac{\partial U^*}{\partial M_s} = 0.00041^\circ \tag{7.9}$$

From equations (7.8) and (7.9) it can be concluded that the applied load to the top part of the frame has negligible influence. Since this part of the frame is considered to have the most influence on the angle of which the force acts on the spanner, the deformation of the remaining components are assumed to have negligible influence.

7.1.2 Fixture

The fixture serves as a mount for the model nut. It is mounted to the frame via a series of M8 nuts and bolts. It consists of three $3mm$ thick and two $15mm$ thick steel plates which are bolted together. The fixture is shown in figure 7.4 and 7.5. The design has been chosen to ensure that the fixture is rigid enough to withstand the applied load. No confirmation of the constructions capability to endure the load has been made. The construction is assumed to be oversized and more than sufficient for its purpose. The fixture is constructed such that it is possible to adjust the angle of the model nut. This has been done to ensure that the applied load on the spanner is at the right angle. The adjustment is made by loosening nuts one and two, shown in figure 7.5, and sliding nut two up or down in the curved cut out, indicated by the dashed lines.

7.1.3 Model Nut

The model nut has been made such that it replicates the function of an actual nut, though its shape is quite different. The model nut is shown in figure 7.6.
Due to the tolerances associated with manufacturing the spanner and model nut it is possible that the two contacting surfaces have different slopes as shown in figure 7.7. In order to compensate for this possible source of error the model nut has been made with one curved face as shown in figure 7.6 and 7.8. The adjustments are made during the measurements, where it is possible to detect if the spanner is subjected to torsion by means of strain gauges.

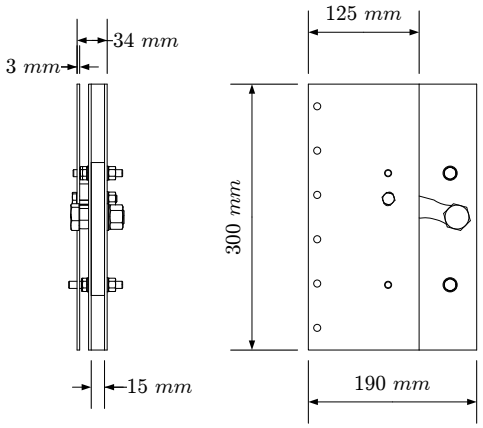

Figure 7.4: *The fixture consists of a three thick steel plates tightened together with possibility for adjusting the position of the nut.*

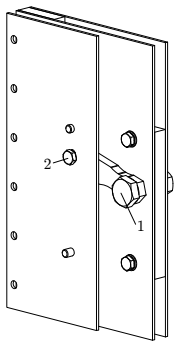

Figure 7.5: *Isometric view of the fixture.*

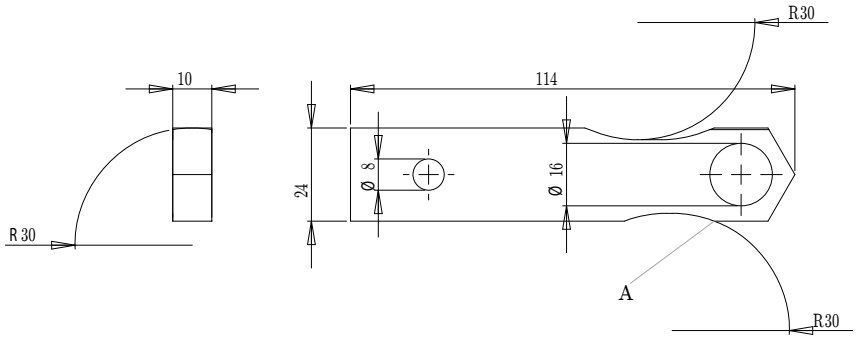

Figure 7.6: *Two curved cut outs have been made to minimise loss of strength in the body while securing the shape of a real nut where it is needed. Dimensions are in millimetres. The model nut is shown upside down.*

The two curved surfaces along the length of the model with radius $30mm$ have been made in order to reduce local stress concentrations, while maintaining the desired length of the two contact surfaces as shown in figure 7.6. During the measurements the jaws of the spanner have been aligned with edge A seen in figure 7.6.
In order to determine the location of the contact surface, the surfaces have been coloured with a permanent marker. After the measurements the coloured surfaces have been inspected. As seen in figures 7.9 and 7.10, some of the paint has been worn off during the measurements. The line of contact is then defined as the mean of the two lines enclosing the worn area. The principal is shown in figure 7.11. Table 7.1 shows the distance from the tip of the upper and lower jaw to the contact line.

Upper jaw	Lower jaw
12 mm	0.5 mm

Table 7.1: *The distance from jaw tip to contact line for both jaws.*

The contact areas have been incorporated into the analytic- and FE analysis.

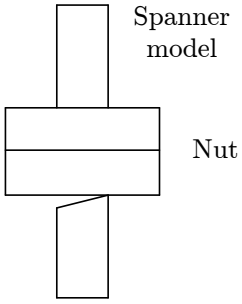

Figure 7.7: *A crooked spanner will experience torsion when applying a moment to a nut.*

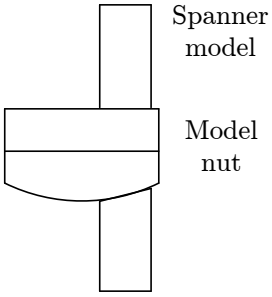

Figure 7.8: *A test nut with one rounded edge will make it possible to adjust the setup in order to decrease torsional effects.*

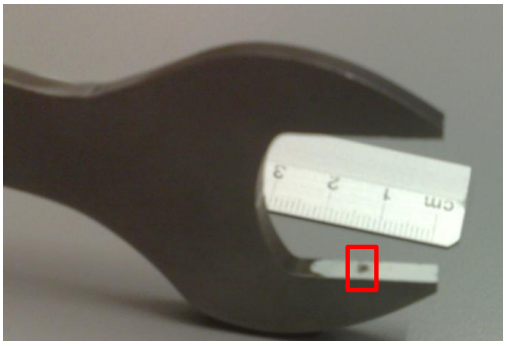

Figure 7.9: *The contact surface for the upper jaw is* $12mm$ *from the outer edge.*

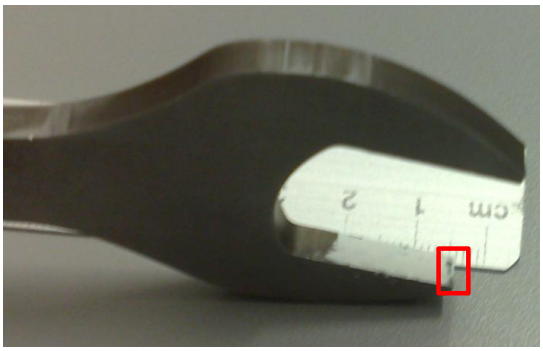

Figure 7.10: *The contact surface for the lower jaw is* $0.5mm$ *from the outer edge.*

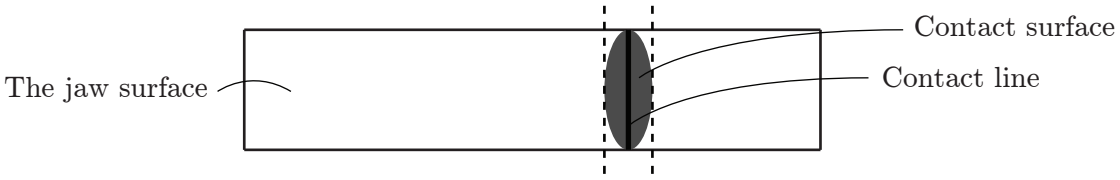

Figure 7.11: *The contact lines are defined as the mean of the two lines enclosing the contact area.*

7.1.4 Load Unit

The load unit consists of three main bar elements, a screw, and a nut. The main bars are held together with pins, as are the connecting bar and screw. The unit is shown in figure 7.12.
The unit is mounted to the frame via two M8 bolts. The previously described fixture is designed such that the load unit and spanner can be aligned directly above one another. Between the load unit and spanner is a load transducer, which can measure the force applied to the spanner. When the nut is turned, the screw and connecting bar are raised. The frame was shown to be oversized for the current experiment. Without further calculations the load unit is assumed to be oversized too. It is thus assumed that the elastic deformation of the load unit has no influence on the load angle.

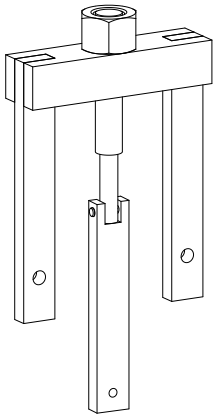

Figure 7.12: *The top nut is turned to apply load to the spanner model.*

7.1.5 Closure

Based on the above assumptions it is presumed that the measurement setup is rigid enough to ensure that the load angle can be maintained throughout the measurements. Thus the only component that compromises the load angle is the deflection of the spanner. The requirement of in-plane loading is assumed to be met due to the design of the fixture, placement of the load unit, and design of the spanner model. The boundary conditions in section 6.2 on the jaws are expected to be representative of the true loading scenario. However since in reality there is no such thing as a frictionless support it is important to be aware if the boundary conditions are met. In order to come as close as possible to the boundary conditions, both spanner jaws and model nut are lubricated during the measurements. The effects of friction can compromise the assumptions regarding the model, so attentiveness is necessary when interpreting the collected data.

Chapter

8

Strain Gauge Measurements

The following chapter consists of four parts. Section 8.1 and 8.2 derive the basic theory of strain gauges and the Wheatstone bridge. Next, the use of strain gauges on a tensile test to give material data is described in section 8.3. Afterwards the theory of strain gauges is in section 8.4 used to approach the practical measurements on the spanner model. At last the data gained from the strain gauge measurements on the spanner are processed in section 8.5 to give new information about the stress state of the spanner.
The theory used in this chapter in general is based on Hoffmann, Mouritsen, and National Instruments [8], [9], [10].

8.1 Strain Gauges

A strain gauge is a measuring tool which is widely used to determine strains in an object. Based on the results of strain gauge measurements it is possible to calculate other parameters of interest e.g. stresses and deformations. Although there are different kinds of strain gauges, the following presents the basic principles of metallic resistive strain gauges together with the most common way to use them. The focus will be on the combination where metallic strain gauges are set up in a Wheatstone bridge. This is also the configuration that has been used for the practical measurements.
There are several kinds of strain gauges e.g. resistive, capacitive, and mechanical strain gauges, and their main purpose is to measure deformations in a material. A resistive strain gauge consists of a thin wire, which is usually glued to the test specimen. The basic principle of a resistive strain gauge is that the electrical resistance in the wire changes as deformation of a test specimen occurs. This change can be measured by putting on a constant current and supply voltage, and calculating the resistance based an an output voltage. In metallic resistive strain gauges the metal wire, which can also be a thin foil, is arranged in a pattern of parallel lines as seen in figure 8.1. The wire pattern makes the strain gauge less exposed to Poisson- and shear strains, but it also contributes to more accurate results than if there was only a single short wire. This is because a longer wire will make the resistance, and hence the change in resistance, larger and thus easier to measure. This is clarified by the mathematical expressions shown later in this section. To prevent electrical disturbances from metal bodies, and to ease the attachment to the test specimen, the wire is bonded to a non-conductive carrier. The centre of the wire pattern is marked on the four sides of the carrier to ease an accurate alignment of the strain gauge onto the specimen.
When a metal strain gauge is exposed to deformation the wire will be thinner and longer if the area of measure is stretched as exemplified in figure 8.2.

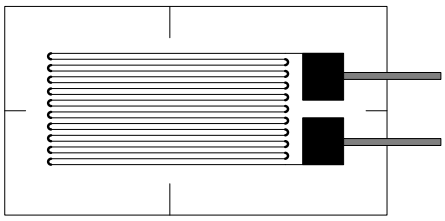

Figure 8.1: *The wire of a resistive metal strain gauge is mounted on a carrier with alignment lines.*

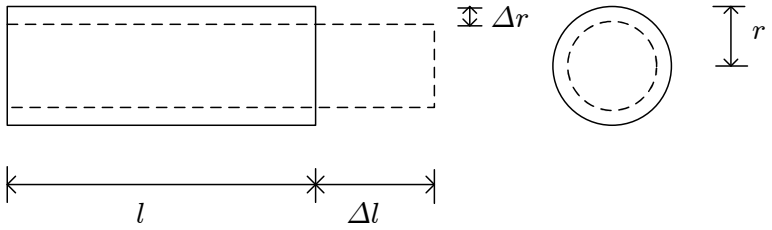

Figure 8.2: *The length and cross section of the wire in a strain gauge is deformed during measurements. The length of the wire is l, and the radius is r.*

When the wire is stretched, the electrical resistance in the wire increases, and the output becomes a positive strain. Negative strain is obtained in the opposite case, where the measured area is compressed and the wire becomes thicker and shorter. In the last case the resistance in the wire decreases. Due to microstructural rearrangements caused by the change in length and cross section area, the resistivity in the wire is slightly changed also. The definition of resistance is

$$R = \rho \frac{l}{A} \tag{8.1}$$

where: R Electrical resistance.
ρ Resistivity.
l Length of wire.
A Cross section area of wire.

The change in resistance depends on changes in length, area (Poisson effect) and resistivity. Applying the chain rule to equation (8.1) yields all the changes as

$$\Delta R = \frac{\rho}{A}\Delta l - \frac{\rho l}{A^2}\Delta A + \frac{l}{A}\Delta\rho \quad \Rightarrow \tag{8.2}$$

$$\frac{\Delta R}{R_0} = \frac{\Delta l}{l} - \frac{\Delta A}{A} + \frac{\Delta\rho}{\rho} \tag{8.3}$$

where: R_0 Initial resistance.

The change in cross section area is dependent on the radius of the wire. The radial strain in a linear elastic material is determined by the strain in the load direction and Poisson's ratio. The change in cross section area can in this case be expressed with respect to strain in the length

direction as

$$\varepsilon_r = \frac{\Delta r}{r} = -\nu\frac{\Delta l}{l} = -\nu\varepsilon \qquad \Rightarrow \tag{8.4}$$

$$\frac{\Delta A}{A} = \frac{2\pi r\Delta r}{\pi r^2} = 2\frac{\Delta r}{r} = 2\varepsilon_r = -2\nu\varepsilon = -2\nu\frac{\Delta l}{l} \tag{8.5}$$

When (8.5) is put into (8.3) it yields the commonly used relation between change in electrical resistance, strain and resistivity in a metal strain gauge

$$\frac{\Delta R}{R_0} = \frac{\Delta l}{l} + 2\nu\frac{\Delta l}{l} + \frac{\Delta\rho}{\rho} \qquad \Rightarrow \tag{8.6}$$

$$\frac{\Delta R}{R_0} = \varepsilon(1+2\nu) + \frac{\Delta\rho}{\rho} \tag{8.7}$$

The most commonly used metal strain gauges have a nominal resistance between 120Ω and 1000Ω. The exact Poisson's ratio and resistivity can vary between different strain gauges because of some changes in material quality and small deviations during production. To minimise these errors the manufacturers measure a statistic average value for Poisson's ratio and the resistivity for a number of gauges of every batch that leaves the factory. This is presented on each package of strain gauges in form of a gauge factor k. When the gauge factor is put into (8.6) it becomes

$$k = \frac{\frac{\Delta R}{R_0}}{\frac{\Delta l}{l}} = \frac{\frac{\Delta R}{R_0}}{\varepsilon} \qquad \Rightarrow \tag{8.8}$$

$$\varepsilon = \frac{\frac{\Delta R}{R_0}}{k} \tag{8.9}$$

For metallic strain gauges k is normally somewhere around 2.
Typical inaccuracies associated with strain gauge measurements is a result of long connecting wires, transverse sensitivity, orientation of the strain gauge, and temperature variations. The wires connecting the strain gauge to the measuring equipment also contribute to the total resistance of the particular strain gauge circuit. If these connecting wires are too long the increase in resistance results in a decrease of the measured strains. The wires used in the project are no longer than two metres and the associated errors are thus neglected. If a strain gauge is elongated or shortened perpendicular to the measurement direction, the result is an in- or decrease of the total measured strain. This type of inaccuracy can for small errors be corrected mathematically with the use of the transverse sensitivity factor, which is supplied by the manufacturer. If the orientation of a strain gauge is not as intended, the results has to be corrected in order to obtain valid results. If a strain gauge is mounted on a metal rod, which is free to expand, and the rod is exposed to a change in temperature, the difference in thermal expansion of the strain gauge and metal rod results in a change in the measured strain. This change in strain is not associated with a change in the stress distribution and the result can thus be misleading. This can be compensated for by coupling strain gauges together in certain bridge configurations.

8.2 The Wheatstone Bridge

The deformations, which are measured by a strain gauge, are normally in the order of a few millistrain. A common 120Ω strain gauge with $k = 2$ subjected to a deformation of 700μ yields the following change in resistance for equation (8.9).

$$\Delta R = 700\cdot 10^{-6}\cdot 2\cdot 120\Omega = 0.168\Omega \tag{8.10}$$

The measuring procedure can be seen as a system with an input, signal processing and an output. Equation (8.10) shows a small change in resistance which implies the need of an amplification of the measured signal. Combined with the above mentioned temperature compensation the measuring system should have an amplifier and a bridge configuration between the input signal from the strain gauge(s) and the output signal on e.g. a computer. A bridge configuration can also exploit different amplifications of signals within the circuit. A principal illustration of a measuring system can be seen in figure 8.3.

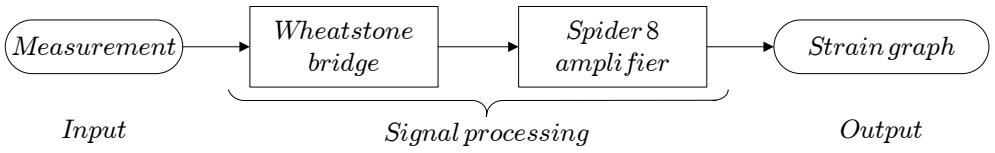

Figure 8.3: *The basic principle of the measurement system. The change in resistance in the strain gauge is processed in the Wheatstone bridge and the Spider* 8 *amplifier before the result is plotted as a graph on the computer.*

The input to the system is the deformation of the strain gauge which gives a change in electrical resistance. In the experiments the Wheatstone bridge and a Spider 8 amplifier have been used. These combined with the computer do the signal processing, and the Spider 8 also works as a power supply. The output is in form of data collection and a graph on a computer where information about applied force and strain as a function of time is gathered.

The Wheatstone bridge is illustrated in figure 8.4. It consists of a supply voltage, four resistances, where one, two or four of them should be a strain gauge depending on wanted configuration and output voltage.

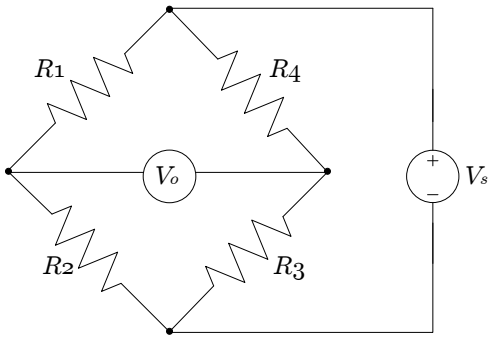

Figure 8.4: *In the Wheatstone bridge one, two or four of the resistances should be replaced with a strain gauge.*

There are several ways to set up a Wheatstone bridge. By analysing the circuit of the Wheatstone bridge and applying Ohm's law can be set up

$$V_o = V_s\left(\frac{R_1}{R_1+R_2} - \frac{R_3}{R_3+R_4}\right) \tag{8.11}$$

where: V_o Output voltage.

V_s Supply voltage.

From this it is seen that if all the resistances are equal the output voltage is zero because the

resistances balance each other out. This also makes sense because equation (8.9) yields that no change in electrical resistance gives no strain. It is thereby correct that there is no output voltage when there are no deformations. To get as precise measurements as possible all measurements should start with a balanced bridge. This is achieved when the initial resistance is equal within the resistance pairs on each side as

$$R_1 = R_2 \quad \text{and} \quad R_3 = R_4 \tag{8.12}$$

When the stain gauges are subjected to deformation (8.11) gives the following equation independent of the number of connected strain gauges between one and four

$$V_o = V_s\left(\frac{R_1+\Delta R_1}{2R_1+\Delta R_1+\Delta R_2} - \frac{R_4+\Delta R_4}{2R_3+\Delta R_3+\Delta R_4}\right) \quad \Rightarrow \tag{8.13}$$

$$V_o = V_s\left(\frac{(R_1+\Delta R_1)(2R_3+\Delta R_3+\Delta R_4)-(R_4+\Delta R_4)(2R_1+\Delta R_1+\Delta R_2)}{(2R_1+\Delta R_1+\Delta R_2)(2R_3+\Delta R_3+\Delta R_4)}\right) \tag{8.14}$$

This is the generalised Wheatstone-equation. However, the many sums and products of the different resistances makes it quite confusing to use. Hence a simplification is desired.
When the multiplications in equation (8.14) are made, it is possible to make a simplification. The terms of $\Delta R_a \cdot \Delta R_b$ can be neglected because they are very small compared to the other terms. The result is

$$V_o = V_s\left(\frac{R_1(\Delta R_3+\Delta R_4)-R_4(\Delta R_1+\Delta R_2)+2R_3\Delta R_1-2R_1\Delta R_4}{4R_1R_3+2R_1\Delta R_3+2R_1\Delta R_4+2R_3\Delta R_1+2R_3\Delta R_2}\right) \tag{8.15}$$

In the denominator it is possible to make further simplifications, due to the first term being much larger than the rest. As a numerical example, a full bridge with 120Ω strain gauges with a strain of 50μ yields:

$$4R_1R_3 = 57600\Omega^2 \quad \text{compared to} \quad 2R_3\Delta R_2 = 2.88\Omega^2 \tag{8.16}$$

As seen in the example (8.16) the small denominator terms can with good approximation be neglected. Equation (8.15) can then be divided into several fraction expressions and be shortened down in agreement with equation (8.12). The result is

$$\frac{V_o}{V_s} = \frac{R_1\Delta R_3}{4R_1R_3} + \frac{R_1\Delta R_4}{4R_1R_3} - \frac{R_4\Delta R_1}{4R_1R_3} - \frac{R_4\Delta R_2}{4R_1R_3} + \frac{2R_3\Delta R_1}{4R_1R_3} - \frac{2R_1\Delta R_4}{4R_1R_3} \Rightarrow \tag{8.17}$$

$$\frac{V_o}{V_s} = \frac{\Delta R_3}{4R_3} + \frac{\Delta R_4}{4R_3} - \frac{\Delta R_1}{4R_1} - \frac{\Delta R_2}{4R_1} + \frac{\Delta R_1}{2R_1} - \frac{\Delta R_4}{2R_3} \Rightarrow \tag{8.18}$$

$$\frac{V_o}{V_s} = \frac{1}{4}\left(\frac{\Delta R_1}{R_1} - \frac{\Delta R_2}{R_2} + \frac{\Delta R_3}{R_3} - \frac{\Delta R_4}{R_4}\right) \tag{8.19}$$

This is the linearised Wheatstone equation.
Equation (8.9) states that $\frac{\Delta R}{R}$ is equal to the strain times the gauge factor. When this is implemented in (8.19) it yields the main equation for the Wheatstone bridge.

$$\frac{V_o}{V_s} = \frac{k}{4}(\varepsilon_1 - \varepsilon_2 + \varepsilon_3 - \varepsilon_4) \tag{8.20}$$

As mentioned above the equation assumes that there is strain gauges in all four spaces, and that they are all subjected to deformation. However, if the initial resistance is the same in the strain gauge(s) and resistance(s) on each side of the bridge as stated in (8.12), the respective ε becomes zero if it is not a deformed strain gauge.

The output of the measuring system, which is shown on the computer is the calculated total strain. The strains in equation (8.20) is, in other words, measured through the gauge factor and the voltage difference and calculated into total strain. This indicated strain can be used to make a more practical equation to calculate the total strain in the different strain gauge setups. The indicated strain will basically be the same as the strain shown in the output of the measuring system, and is

$$\varepsilon_i = \frac{V_0}{V_s}\frac{4}{k} \qquad \Rightarrow \tag{8.21}$$

$$\varepsilon_i = \varepsilon_1 - \varepsilon_2 + \varepsilon_3 - \varepsilon_4 \tag{8.22}$$

The theory and equations presented in these two sections (8.1 and 8.2) makes the foundation for the strain gauge calculations used in the postprocessing of the experimental data.

8.3 Tensile Test

In order to determine the material properties Young's modulus and Poisson's ratio of the spanner model a tensile test is performed. In the following a brief documentation of the experimental setup is given succeeded by presentation of the test results. Finally the uncertainties of the tensile test results are addressed.

8.3.1 Experimental Setup

The test is carried out on a 20kN tension test system which is powered by hydraulics providing the desired force. The tensile specimen is fixated by friction between two jaws. The tensile specimen is dimensioned in accordance to DS 10110 D [11]. The dimensions are seen in figure 8.5. There are three strain gauges attached on the test specimen. On side A a strain gauge SG

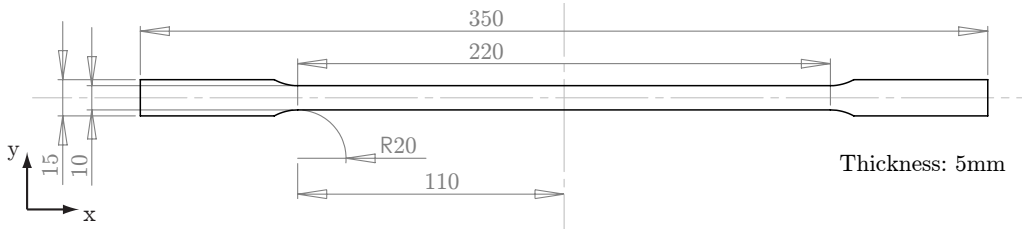

Figure 8.5: *The dimensions of the tensile specimen. Dimensions are in mm.*

1 is attached in the x-directionas shown in figure 8.6. On the opposite side is attached a so called *angle strain gauge* consisting of SG 2 and SG 3 where two strain gauges are positioned perpendicular to each other on one carrier.

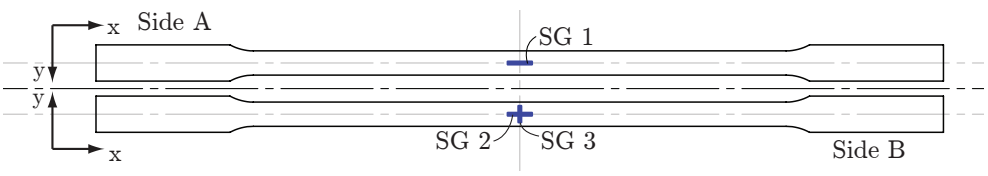

Figure 8.6: *The attached strain gauges.*

SG 2 is aligned in the x-direction and SG 3 in the y-direction. The purpose of the two strain gauges in the x-direction is to measure the elongation independently and the strain gauge in the y-direction measures the contraction due to the Poisson effect. The strain gauges are positioned where the centerlines of the test specimen intersect. The gauges are connected to a Spider8 multi channel amplifier in three quarter bridges. The data from the amplifier is handled by the software Catman Easy using a computer. This enables recording of data realtime from the strain gauges. A load cell is connected to the tension test machine. This load cell is also connected to the Spider8 amplifier and the applied force is gathered in Catman Easy in realtime.

8.3.2 Results and Data Processing

The graph in figure 8.7 shows the stress strain curve for the tensile test of the test specimen. The data for the strain is the averaged strain $\overline{\varepsilon} = \frac{\varepsilon_{SG1}+\varepsilon_{SG2}}{2}$. This data is fitted in the sense that a straight line is drawn in the best possible conformity with all the sampling points. Some unexplainable noise occurred during the test where the force showed large sudden deviations at a few measuring points. These sudden deviations are sorted out of the data set.

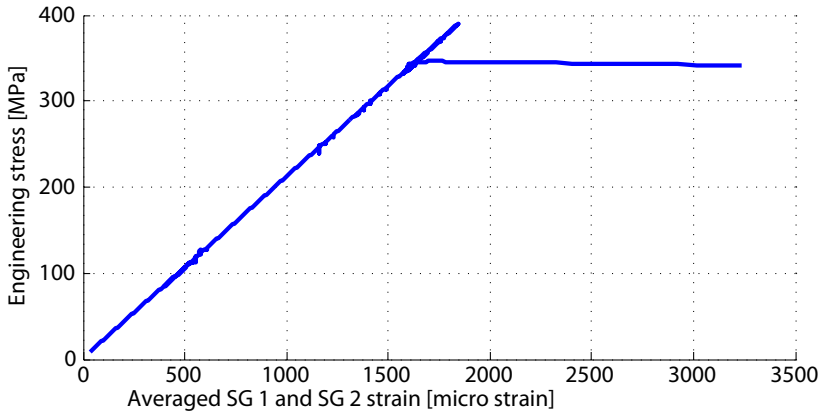

Figure 8.7: *The stress strain curve for the tensile test.*

Figure 8.7 shows a linear tendency up to approximately 1500 μ strain. For strains larger than 1500 μ strain the curve shows the expected tendency for a steel which yields and then deforms plastically. However the values of the the strain gauge measurements at strains above 2500μ can not be considered valid since they only perform reliably below this limit. In order to determine the modulus of elasticity E of the material a linear data fit is made for the loading as a function of $\overline{\varepsilon}$. This is illustrated in figure 8.8.
The measuring equipment for the experiment was reset when one end of the test specimen was free, which resulted in a small deformation when the other end was mounted. Figure 8.8 shows that in the beginning of the test SG 1 and SG 2 indicate a small amount of compression and extension, respectively. This is not an optimal situation, but because of the linear fit function the result is still credible. To determine the Poisson's ratio ν for the material a linear data fit is made for the strains measured by SG 3 as a function of the strains measured by SG 2. This is shown in figure 8.9.
The modulus of elasticity E is determined from the slope of the linear data fit in figure 8.8 as:

$$E = \frac{a}{A_s} = \frac{0.0105 \cdot 10^9 N}{50 mm^2} = 209\, GPa \tag{8.23}$$

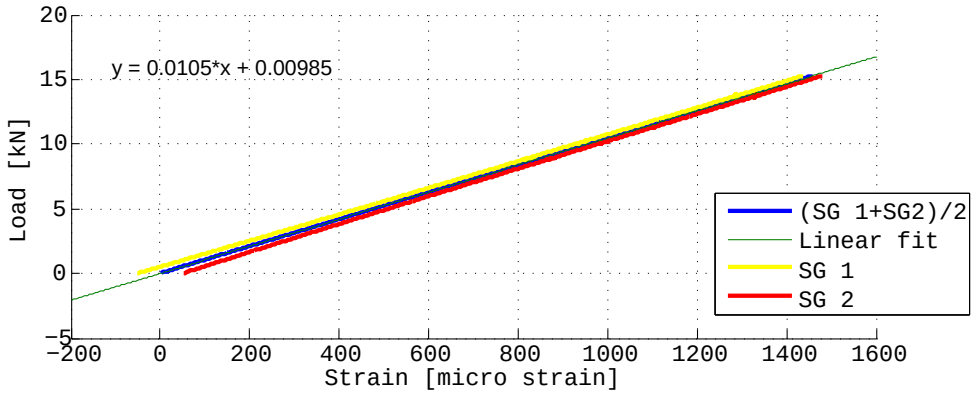

Figure 8.8: *The loading as a function of the strains with a data fit for* $\overline{\varepsilon}$.

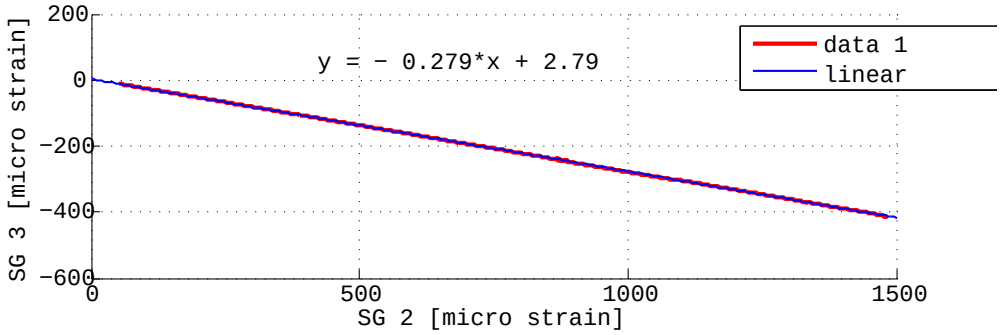

Figure 8.9: *The Poisson's ratio* ν *is the absolute value of the slope of the curve.*

where: a The slope of the linear data fit in figure 8.8. $a = 0.0105 \cdot 10^9 N$.

A_s The cross sectional area of the test specimen.

The Poisson's ratio is given directly from the linear data fit in figure 8.9 and is found to be:

$$\nu = 0.2795 \simeq 0.28 \tag{8.24}$$

8.3.3 Determination of Uncertainty of E and ν

With the experimental determination of E and ν there are uncertainties tied to the values. These uncertainties will be treated and a complete uncertainty and standard deviation will be associated with E and ν. The methodical approach is adopted from Ole Ø. Mouritsen [12]. The sources of uncertainties that contribute to the complete uncertainty are listed in table 8.1 together with their relative uncertainty $\frac{s(x)}{x}$ in percentage.

Source	Relative uncertainty in %
Linear data fit for E	$7 \cdot 10^{-5}$
Linear data fit for ν	$3 \cdot 10^{-4}$
k-factor	0.5
Load transducer	0.5
Strain gauge amplifier - Spider8	0.05
Specimen width	0.1
Specimen height	0.4

Table 8.1: *The table summarises the sources of uncertainty and their relative uncertainty.*

The class term for the load transducer is 1 and the class term for the Spider8 amplifier is 0.1. The k-factor is 2.1 for SG 1 and 2.12 for SG 2 and SG 3 and the uncertainty on the k-factors are ±1 %. The tolerances on the dimensions of the specimen have been determined using a micrometre screw. The tolerance for the width is 0.01 mm and for the thickness 0.02 mm. The sample standard deviation for the linear data fit of the load L, which is used for determining the relative uncertainty of E, is found by:

$$s(L)_{lin} = \sqrt{\frac{\sum (X_{dataset} - X_{line})^2}{n-1}} = 7.3\,N \tag{8.25}$$

where:
- $X_{dataset}$ The values measured and recorded in the experiment.
- X_{line} The values from the linear data fit.
- n The number of samples.
- $s(L)_{lin}$ The sample standard deviation on the load fit.

For ν, the corresponding equation gives $s(\nu) = 0.84$. Using the law of accumulation for uncertainties the relative uncertainty of the Youngs Modulus E can be determined:

$$s(X) = \sqrt{\left(\frac{\partial X}{\partial x} s(x)\right)^2 + \left(\frac{\partial X}{\partial y} s(y)\right)^2 + \left(\frac{\partial X}{\partial z} s(z)\right)^2 + \ldots} \tag{8.26}$$

$$s_r(E) = \sqrt{(s_r(L)_{lin})^2 + 2 \cdot (\tfrac{1}{2} s_r(k))^2 + (s_r(L))^2 + (s_r(A))^2 + (s_r(w))^2 + (s_r(h))^2} = 0.74\,\% \tag{8.27}$$

where:
- $s_r(L)_{lin}$ The relative uncertainty for the linear data fit of the load.
- $s_r(k)$ The relative uncertainty of the k-factor.
- $s_r(L)$ The relative uncertainty from the load transducer.
- $s_r(A)$ The relative uncertainty from the strain gauge amplifier - Spider8.
- $s_r(w)$ The relative uncertainty of the specimen width.
- $s_r(h)$ The relative uncertainty of the specimen height.

The sample standard deviation of E is then found by:

$$s(E) = s_r(E) \cdot E = 1.6\,GPa \tag{8.28}$$

The relative uncertainty for ν can similarly be found as:

$$s_r(\nu) = \sqrt{(s_r(\nu)_{lin})^2 + 2 \cdot (s_r(k))^2 + 2 \cdot (s_r(A))^2} = 0.68\,\% \tag{8.29}$$

The sample standard deviation of ν is then found by:

$$s(\nu) = s_r(\nu) \cdot \nu = 0.0019 \tag{8.30}$$

A total of five tensile tests have been conducted and the sample standard deviation is found to be $0.78\,GPa$ for E and 0.0017 for ν. These values lie within the sample standard deviations found in (8.28) and (8.30) and thereby substantiating the uncertainties found for E and ν.

8.4 Strain Gauge Measurements on the Spanner

In order to get a better estimation of the actual strains and stresses in the spanner during operation, strain gauge experiments have been conducted. A number of strain gauges are attached to the produced spanner in order to measure strains which, in coherence with some basic assumptions, can be used to determine stresses in the examined points.

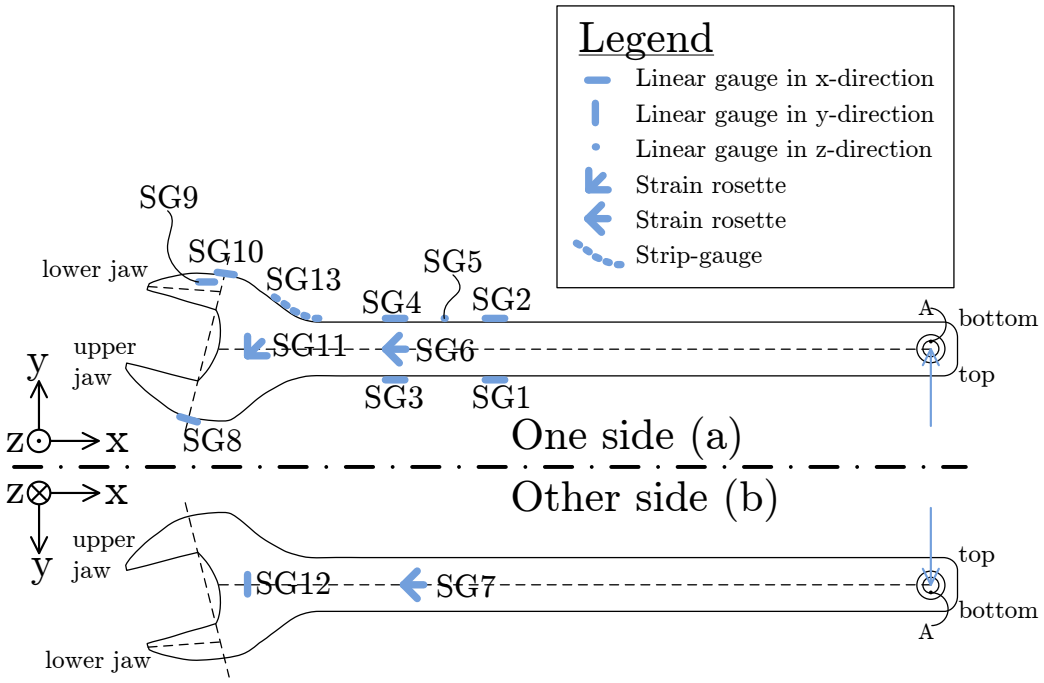

Figure 8.10: *Overview of the spanner with the attached strain gauges. Strain gauges that are visible from both sides are only shown on side a.*

When planning the strain gauge experiment, the overall idea is to have some strain gauges which are used mainly to control the loading scenario, i.e. reproduce well-known information, and some which are used for getting new information. An overview of the spanner with all the attached strain gauges is shown in figure 8.10. The exact location of each strain gauge is given in appendix A. As seen in the figure thirteen strain gauges are employed. The use of the strain gauges can be divided into four subsidiary objectives:

1. Controlling the nominal loads, i.e. ensuring that the voltage read from the strain gauges correspond to a well-known strain determined from the applied load.
2. Ensuring that the basic assumptions about the loading scenario are true; or at least close to true.

3. Determination of stresses in the jaws. This gives new information and can be compared to results from the analytic solutions.

4. Determining the stresses at a point in the unknown section (3) from figure 6.1. This gives new information and can be compared to the Finite Element Analysis.

Each of these four objectives will be sought achieved by the use of a number of the strain gauges in figure 8.10. The objectives will be examined in the following subsections.

8.4.1 Objective 1: Controlling the Nominal Loads

As noted in section 7.1.4 the applied force is measured with a load transducer. This force causes normal stresses in the top and bottom of the shank due to the moment, as described in section 6. Hereby SG3 and SG4 stretches and contracts, respectively. By coupling these two strain gauges in a Wheatstone-bridge the readout-signal can be doubled, reducing the uncertainties' impact on the result. SG3 and SG4 are coupled as resistances R1 and R2 in a Wheatstone-bridge, which are substituted into equation 8.22 to give the following indicated strain:

$$\varepsilon_i = \varepsilon_{SG3} - \varepsilon_{SG4} + \varepsilon_{R_3} - \varepsilon_{R_4} = \varepsilon_{SG3} - \varepsilon_{SG4} + 0 - 0 = \varepsilon_{SG3} - \varepsilon_{SG4} \tag{8.31}$$

$$= (\varepsilon_N + \varepsilon_M^{top}) - (\varepsilon_N + \varepsilon_M^{bottom}) = \varepsilon_M^{top} - \varepsilon_M^{bottom} = \varepsilon_M^{top} - (-\varepsilon_M^{top}) \tag{8.32}$$

$$= 2\varepsilon_M^{top} \tag{8.33}$$

where:

ε_i	The indicated strain.
ε_X	The strain from the strain gauge in position X in the Wheatstone-bridge.
ε_M^X	The strain in position X due to the moment.
ε_N^X	The strain in position X due a tensile force.

According to the Bernoulli-Euler theory of Beams ε_M^{top} is related to the applied load, P, as:

$$\sigma_M^{top} = -\frac{M\left(\frac{-h}{2}\right)}{I_z} \qquad \Rightarrow \tag{8.34}$$

$$\varepsilon_M^{top} = \frac{\sigma_M^{top}}{E} = \frac{M\frac{h}{2}}{EI_z} = \frac{P\,|(SG3)A|_x\,h}{2EI_z} \tag{8.35}$$

where:

σ_M^{top}	The stresses in the top of the shank due to the moment.
h	The height of the shank.
$\|(SG3)A\|_x$	The x-component of the vector from SG3 to point A.

Hence, the nominal applied load can be controlled by comparing the force indicated by the load transducer with equation (8.35) inverted combined with (8.33):

$$P = \frac{2EI_z\varepsilon_M^{top}}{|(SG3)A|_x\,h} = \frac{EI_z\varepsilon_i}{|(SG3)A|_x\,h} \tag{8.36}$$

8.4.2 Objective 2: Ensuring the Basic Assumptions

As stated above another objective, in order to have valid data, is to ensure that the basic assumptions about the load scenario are correct; or at least close to correct. In order to control

this aspect, a number of strain gauges are placed on the spanner at places where the loadings can be controlled. The possible loads on the spanner are shown in figure 8.11. Blue loads are desired as these stem from the applied load in the y-direction. These were controlled in objective 1. Red loads, however, are undesired. These are effects of a bad alignment in the setup, bad tolerances or a similar inexpediency in the experiment.

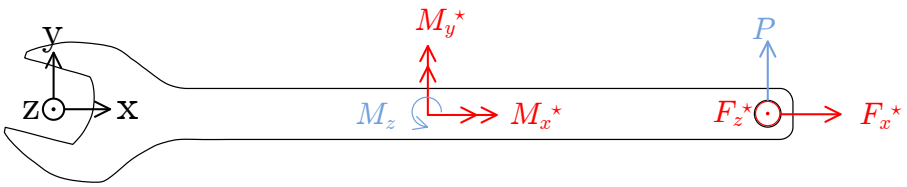

Figure 8.11: *Overview of the spanner with all possible loads. Blue loads are desired, whereas red loads are undesired. Undesired loads are also denoted with a *. Note that the loads are not necessarily placed where they would attack the spanner.*

The control of all undesired loads will be examined one by one in the following.

8.4.2.1 Tensile Force F_x^*

Whether the spanner is subjected to a tensile force is checked by two strain gauges measuring normal stresses in the shank area. SG1 and SG2 are connected to the Spider8 individually. Calculations similar to that for the SG3-SG4 bridge can be performed by inserting the individually measured strains into the Wheatstone bridge equation, resulting in a virtual half bridge. This gives:

$$\varepsilon_i = \varepsilon_1 - \varepsilon_2 + \varepsilon_3 - \varepsilon_4 = \varepsilon_{SG1} - 0 + \varepsilon_{SG2} - 0 = \varepsilon_{SG1} + \varepsilon_{SG2} \tag{8.37}$$

$$= (\varepsilon_N^{top} + \varepsilon_M^{top}) + (\varepsilon_N^{bottom} + \varepsilon_M^{bottom}) = (\varepsilon_N^{top} + \varepsilon_M^{top}) + (\varepsilon_N^{top} - \varepsilon_M^{top}) \tag{8.38}$$

$$= 2\varepsilon_N^{top} \tag{8.39}$$

and thus the tensile force F_x^* can be determined as:

$$F_x^* = A\sigma_N = AE\varepsilon_N^{top} = \frac{AE\varepsilon_i}{2} \tag{8.40}$$

where: A The area of a section cut in the shank.

The verification of the tensile force is associated with a greater uncertainty, since SG1 and SG2 are not coupled in the same bridge.

8.4.2.2 Bending Force F_z^* and Moment M_y^*

The presence of a bending force F_z^* is rather unlikely and would most likely result in a moment contribution to M_y^*. Therefore, only the presence of the moment M_y^* is examined. The presence of this moment is measured by the use of strain gauges SG6$^{0^\circ}$ and SG7$^{0^\circ}$ (the superscript $^{0^\circ}$ indicating the 0°-gauges in the two rosettes SG6 and SG7 with respect to the x-axis.). These two are coupled as R1 and R2 in a Wheatstone-bridge given the following indicated strain in the experiment:

$$\varepsilon_i = \varepsilon_1 - \varepsilon_2 + \varepsilon_3 - \varepsilon_4 = \varepsilon_{SG6^{0^\circ}} - \varepsilon_{SG7^{0^\circ}} + 0 - 0 = \varepsilon_{SG6^{0^\circ}} - \varepsilon_{SG7^{0^\circ}} \tag{8.41}$$

$$= (\varepsilon_N^a + \varepsilon_{M_y^*}^a) - (\varepsilon_N^b + \varepsilon_{M_y^*}^b) = (\varepsilon_N^a + \varepsilon_{M_y^*}^a) - (\varepsilon_N^a - \varepsilon_{M_y^*}^a) \tag{8.42}$$

$$= 2\varepsilon_{M_y^*}^a \tag{8.43}$$

where: ε_N^x The strain on side x due to a tensile force.
$\varepsilon_{M_y^*}^x$ The strain on side x due to the moment M_y^*.

According to the Bernoulli-Euler beam theory this can be converted into a moment M_y^* by the following calculations:

$$\sigma_{M_y^*}^a = -\frac{M_y^* \frac{t}{2}}{I_y} \quad \Rightarrow \tag{8.44}$$

$$\varepsilon_{M_y^*}^a = \frac{\sigma_{M_y^*}^a}{E} = -\frac{M_y^* \frac{t}{2}}{EI_y} \quad \Rightarrow \tag{8.45}$$

$$M_y^* = -\frac{2EI_y\varepsilon_{M_y^*}^a}{t} = -\frac{EI_y\varepsilon_i}{t} \tag{8.46}$$

where: t The thickness of the spanner.
$\sigma_{M_y^*}^x$ The stress on side x due to the moment M_y^*.

8.4.2.3 Torsional moment M_x^*

A moment contribution around the x-axis would correspond to having torsion in the shank. Thus introducing shear strains near the surface of the shank. These are measured using the two rosettes SG6 and SG7; particularly $SG6^{45^\circ}$, $SG6^{-45^\circ}$, $SG7^{-45^\circ}$ and $SG7^{45^\circ}$. If coupled correct a full-bridge with these four gauges gives the double readout-signal of the shear strains. According to the theory of elasticity the strain of each of the four gauges can be expressed by equation 5.39:

$$\varepsilon_{SG6^{45^\circ}} = \varepsilon_{ij}n_i n_j = \frac{1}{2}\varepsilon_1^a + \varepsilon_{12}^a + \frac{1}{2}\varepsilon_2^a \tag{8.47}$$

$$\varepsilon_{SG6^{-45^\circ}} = \varepsilon_{ij}n_i n_j = \frac{1}{2}\varepsilon_1^a - \varepsilon_{12}^a + \frac{1}{2}\varepsilon_2^a \tag{8.48}$$

$$\varepsilon_{SG7^{-45^\circ}} = \varepsilon_{ij}n_i n_j = \frac{1}{2}\varepsilon_1^b - \varepsilon_{12}^b + \frac{1}{2}\varepsilon_2^b \tag{8.49}$$

$$\varepsilon_{SG7^{45^\circ}} = \varepsilon_{ij}n_i n_j = \frac{1}{2}\varepsilon_1^b + \varepsilon_{12}^b + \frac{1}{2}\varepsilon_2^b \tag{8.50}$$

where: ε_1^x The first principal strain at side x.
ε_2^x The second principal strain at side x.
ε_{12}^x The 12-component of the strain tensor at side x.

Coupling the these gauges into a Wheatstone-bridge as R1, R2, R3, and R4, respectively, the indicated strain from the experiment yields:

$$\varepsilon_i = \varepsilon_1 - \varepsilon_2 + \varepsilon_3 - \varepsilon_4 = \varepsilon_{SG6^{45^\circ}} - \varepsilon_{SG6^{-45^\circ}} + \varepsilon_{SG7^{-45^\circ}} - \varepsilon_{SG7^{45^\circ}} \tag{8.51}$$

$$= (\frac{1}{2}\varepsilon_1^a + \varepsilon_{12}^a + \frac{1}{2}\varepsilon_2^a) - (\frac{1}{2}\varepsilon_1^a - \varepsilon_{12}^a + \frac{1}{2}\varepsilon_2^a) + (\frac{1}{2}\varepsilon_1^b - \varepsilon_{12}^b + \frac{1}{2}\varepsilon_2^b) - (\frac{1}{2}\varepsilon_1^b + \varepsilon_{12}^b + \frac{1}{2}\varepsilon_2^b) \tag{8.52}$$

$$= 2\varepsilon_{12}^a - 2\varepsilon_{12}^b = 2(\varepsilon_{12,M_x^*}^a + \varepsilon_{12,V}^a) - 2(\varepsilon_{12,M_x^*}^b + \varepsilon_{12,V}^b) \tag{8.53}$$

$$= 2(\varepsilon_{12,M_x^*}^a + \varepsilon_{12,V}^a) - 2(-\varepsilon_{12,M_x^*}^a + \varepsilon_{12,V}^a) = 4\varepsilon_{12,M_x^*}^a \tag{8.54}$$

$$= 2\gamma_{xy,M_x^*} \tag{8.55}$$

where: $\varepsilon^{y}_{12,V}$ The tensor shear strain due to the shear force V at side y.

$\varepsilon^{y}_{12,M^*_x}$ The tensor shear strain due to the torsional moment M^*_x at side y.

γ_{xy,M^*_x} The engineering shear strain due to the torsional moment M^*_x.

This indicated strain can according to Ugural and Fenster be converted into a torsional moment M^*_x as [5, p.255]:

$$\tau_{xy} = \frac{M^*_x}{\alpha_{M^*_x} b w^2} \tag{8.56}$$

where: τ_{xy} The shear stress in the shank due to torsion.

$\alpha_{M^*_x}$ Constant determined by a and b.

b Height of the spanner.

w Width of the spanner.

8.4.2.4 Bending moment M^*_x

A bending moment around the x-axis can occur if the spanner-nut setup is very unfortunate, that is if the are imperfections due to bad tolerances. This situation is illustrated in figure 8.12

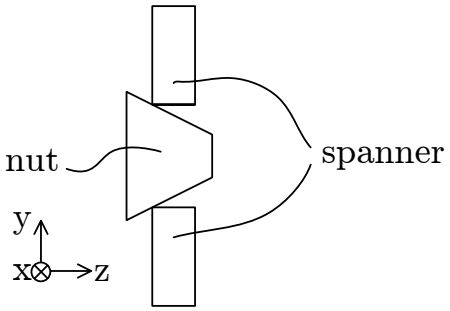

Figure 8.12: *End-view of an unfortunate spanner-nut setup due to the tolerances of the spanner and nut. The misalignment of lines is wildly exaggerated in order to clarify the problem.*

The appearance of this moment is checked by use of SG11$^{90^\circ}$ and SG12. These gauges could be coupled as R1 and R2 in a Wheatstone-bridge to give the double readout-signal. However, this would alter the usefulness of strain rosette SG11. This is clarified in section 8.4.4. Hence the two gauges are not coupled. Instead the results of the two separate gauges are just compared. The two gauges are expected to show the following strains:

$$\varepsilon_{SG11^{90^\circ}} = \varepsilon_{N_y} + \varepsilon^{a}_{M^*_x} \tag{8.57}$$

$$\varepsilon_{SG12} = \varepsilon_{N_y} + \varepsilon^{b}_{M^*_x} = \varepsilon_{N_y} - \varepsilon^{a}_{M^*_x} \tag{8.58}$$

Hence it is clear that if the two gauges do not indicate similar strains, a bending moment M^*_x must be present. It should be noted that since no known theory is applicable in this region the strains cannot be converted into a corresponding moment. However, it is worth checking anyway if the two strains are within the same range.

8.4.3 Objective 3: Obtain information about the jaws

When it is ensured that the nominal loads and the basic assumptions are all okay, the retrieval of new information can begin. Thus, the third objective of the strain gauge experiment is to obtain information about the strains in the jaws, in order to compare this to the results of the analytic analysis of the jaws.
Three strain gauges are used for obtaining information about the jaws. Two gauges, SG9 and SG10, are placed on the lower jaw as the analytic results of this jaw is believed to be most accurate. Hence comparison is possible.
Regarding the upper jaw the analytic results are more questionably and hence comparison with any strain gauge measurements is doubtful. Therefore only one strain gauge, SG8, is placed on the upper jaw.

8.4.4 Objective 4: Obtain Information about the Strain State in the Unknown Section

The fourth objective of the strain gauge experiment is to obtain information about the strain state in the unknown section (3) from figure 6.1. In order to get a complete description of the strain state somewhere in this region, a strain rosette has been placed in the region. The indicated values of the three gauges are interpreted as:

$$\varepsilon^{0^\circ} = \varepsilon_{ij} n_i n_j = \varepsilon_1 \tag{8.59}$$

$$\varepsilon^{45^\circ} = \varepsilon_{ij} n_i n_j = \frac{1}{2}\varepsilon_1 + \varepsilon_{12} + \frac{1}{2}\varepsilon_2 \tag{8.60}$$

$$\varepsilon^{90^\circ} = \varepsilon_{ij} n_i n_j = \varepsilon_2 \tag{8.61}$$

Hence ε_1, ε_2 and ε_{12} can be determined and later compared to results of the Finite Element Analysis.

The strip gauge SG13 also provides information about this section of the spanner. The strip gauge is oriented in the x-direction. SG13 consists of five single gauges which are individually connected to the Spider8 amplifier.

8.5 Results and Data Processing of Strain Gauge Measurement

In the following section the collected data from the strain gauge measurements are presented. First all results along with their respective uncertainties are presented to give an overview. Afterwards the objectives from section 8.4 are examined. The recorded data from the measurements is located in appendix C.2.

The strain gauge measurements are carried out as described in the preceding sections of this chapter and chapter 7. In order to minimise the effects of electrical disturbances eg. from fluorescent lamps etc. which are supplied with 50-60Hz alternating current, a sampling rate of 100Hz have been used through all the experiments. Figures 8.13 and 8.14 show the spanner with the strain gauges attached, bridge circuits and the measuring amplifier.
In coherence with the calculated estimates from chapter 6 the experiments have been performed with a maximum load of 100N. To ensure that the results used in the post processing only contain strains from a load of 100N all data with loads below 100N and above 101N have been removed.

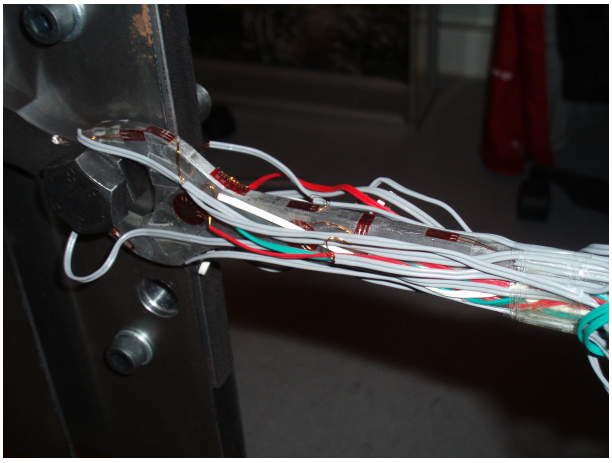

Figure 8.13: *Close up of spanner with strain gauges.*

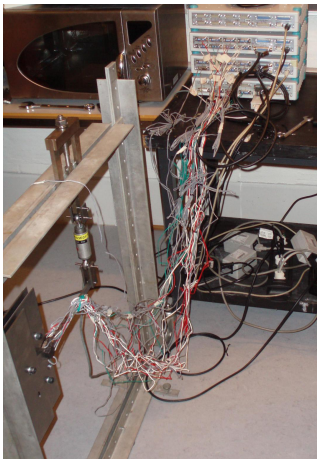

Figure 8.14: *Actual measurement setup.*

In table 8.2 the results based on three experiments are shown. Each bridge circuit is shown together with the arrangement of the strain gauges, gauge factor k, average measured strain $\overline{\varepsilon}_i$, and the associated uncertainties $\frac{s(\overline{\varepsilon}_i)}{\overline{\varepsilon}_i}$.

Bridge circuit	**Type**	**R1**	**R2**	**R3**	**R4**	**k**	$\overline{\varepsilon}_i\ /\mu$	$\frac{s(\overline{\varepsilon}_i)}{\overline{\varepsilon}_i}$**/%**
Simple quarter	Linear gauge	SG1	R_C	R_C	R_C	2.1	290	1.3
Simple quarter	Linear gauge	SG2	R_C	R_C	R_C	2.1	-268	1.2
Half	Linear gauges	SG3	SG4	R_C	R_C	2.12	742	0.7
Simple quarter	Linear gauge	SG5	R_C	R_C	R_C	2.1	93	0.8
Half	Strain rosettes	$SG6^{0^\circ}$	$SG7^{0^\circ}$	R_C	R_C	2.12	-5	18.6
Full	Strain rosettes	$SG6^{45^\circ}$	$SG6^{-45^\circ}$	$SG7^{45^\circ}$	$SG7^{-45^\circ}$	2.12	-3	8.5
Simple quarter	Linear gauge	SG8	R_C	R_C	R_C	2.1	-651	2.0*
Simple quarter	Linear gauge	SG9	R_C	R_C	R_C	2.1	-962	2.2*
Simple quarter	Linear gauge	SG10	R_C	R_C	R_C	2.1	-1264	3.9*
Simple quarter	Strain rosette	$SG11^{0^\circ}$	R_C	R_C	R_C	2.12	215	2.0*
Simple quarter	Strain rosette	$SG11^{45^\circ}$	R_C	R_C	R_C	2.12	-44	2.0*
Simple quarter	Strain rosette	$SG11^{90^\circ}$	R_C	R_C	R_C	2.12	-85	1.4*
Simple quarter	Linear gauge	SG12	R_C	R_C	R_C	2.1	-59	1.3*
Simple quarter	Strip-gauge	SG13.1	R_C	R_C	R_C	2.1	-560	1.5*
Simple quarter	Strip-gauge	SG13.2	R_C	R_C	R_C	2.1	-516	1.5*
Simple quarter	Strip-gauge	SG13.3	R_C	R_C	R_C	2.1	-599	1.2*
Simple quarter	Strip-gauge	SG13.4	R_C	R_C	R_C	2,1	-442	1.4*
Simple quarter	Strip-gauge	SG13.5	R_C	R_C	R_C	2.1	-437	1.4*

Table 8.2: *Results from the experiment.∗ represents values where the largest sample standard deviation has been determined between average values. R_C indicates completion resistances in the Wheatstone-bridge.*

The average strains $\overline{\varepsilon}_i$ have been calculated using the three data sets, where grease was used on the jaws and nut. This issue is explained later in this chapter. The relative uncertainties $\frac{s(\overline{\varepsilon}_i)}{\overline{\varepsilon}_i}$

are calculated for each strain gauge using

$$\frac{s(\varepsilon_i)}{\varepsilon_i} = \sqrt{\sum\left((s_{r,sys})^2\right) + \sum\left((s_{r,nonsys})^2\right)} \tag{8.62}$$

$$\frac{s(\varepsilon_i)}{\varepsilon_i} = \sqrt{\left(\frac{s(k_i)}{k_i}\right)^2 + \left(\frac{s(\alpha_i)}{\overline{\varepsilon}_i}\right)^2 + \left(\frac{s(d_i)}{\overline{\varepsilon}_i}\right)^2} \tag{8.63}$$

where:

$s_{r,sys}$	The relative uncertainty due to systematic errors.
$s_{r,nonsys}$	The relative uncertainty due to nonsystematic uncertainties. This includes among other things the uncertainty on the load transducer and the uncertainty on the applied loads.
$\frac{s(k_i)}{k_i}$	Relative uncertainty for the k-factor for SG_i.
$\frac{s(\alpha_i)}{\overline{\varepsilon}_i}$	Relative uncertainty due to angular misplacement of SG_i.
$\frac{s(d_i)}{\overline{\varepsilon}_i}$	Relative uncertainty due to all nonsystematic uncertainties associated with each strain gauge.

Note that the uncertainty due to angular misplacement only is calculated for quarter bridges.
The sample standard deviation associated with each strain gauge has been estimated using two methods where the method resulting in the largest sample standard deviation has been selected for use in the calculations. This is considered to be a conservative approach.
The first method uses the largest difference between two data points within each of the data sets. This is illustrated in figure 8.15 by the two red lines. If the difference between the two red lines is called T_1 then the tolerance t_1 is $\pm\frac{1}{2}T_1$. So the sample standard deviation is $\frac{1}{2}t_1$.

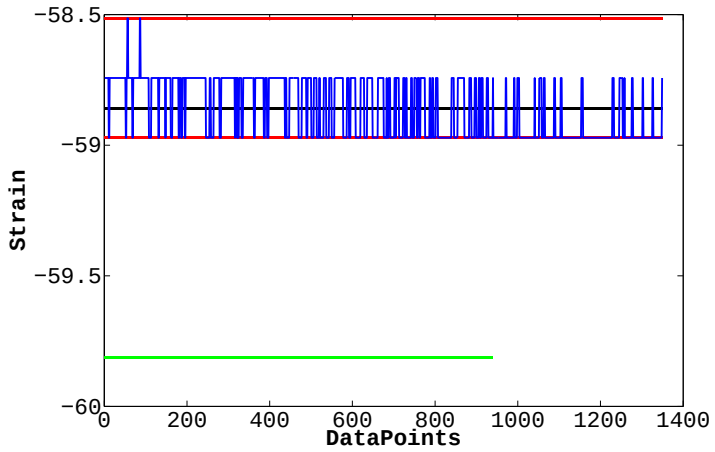

Figure 8.15: *Sample standard deviation selection for SG12. Blue: Measured strains, Red: Largest difference between measured strains, Black: Average value of measured strains, Green: Average value from different data set.*

The second method uses the largest difference of the average values between all of the data sets and determines from this the sample standard deviation. This is done by the same approach as for the first method but using the difference between the black and green line in figure 8.15. The methods are distinguished in table 8.2 by the added $*$ to the relative uncertainties, where $*$ represents values where the largest sample standard deviation has been determined by the second method. Figure 8.15 shows the specific case for SG12. Here the largest sample standard deviation was found between two average values.

8.5.1 Effects of Friction

As mentioned in section 7.1.5, friction can have some influence on the boundary conditions. The experiments have been performed three times with and without grease on the jaws and nut. The data from these experiments are compared in order to determine the effects of friction on the system. Figure 8.16 shows two measurements for SG10, with and without grease applied. The location of SG10 is seen in figure 8.10.

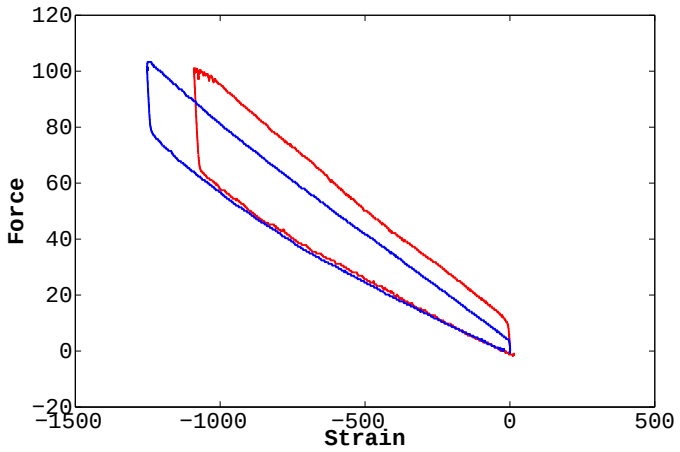

Figure 8.16: *Force strain plot for SG10. Blue: Measurement with grease, Red: Measurement without grease*

As seen on figure 8.16 both measurements display a linear relation between the applied force and resulting strain during loading from $0N$ to $100N$. When unloading both curves display a discontinuity. The red curve, where grease was not applied, jumps from $100N$ down to around $65N$, but at nearly constant strain. Afterwards the strains continue down a slight parabolic curve as the load is reduced and reaches a value of zero when the load is removed. The blue curve, where grease was applied, shows the same tendency but the force only jumps from $100N$ down to around $80N$ before it begins to vary down a curve with the same parabolic shape as for the red curve. The phenomenon is believed to be caused by friction between the jaw and the nut. This explains why the discontinuity is of less value when grease is applied. It is also noted that the measurement with grease applied reaches a higher absolute strain value. This indicates that trying to lower the magnitude of the friction force with grease causes a greater force normal to the jaws and resulting in greater bending strains in the jaw. It can thus be concluded that the presence of friction between the jaws and nut can result in lower absolute measured strain values. Based on this assumption the measurements where grease has been applied are used in the following.
Figure 8.17 shows measurements for strain gauges SG13.1, SG13.3, and SG13.5. It is noted that the effects resulting from friction reduces as the distance from the jaws is increased, and are reduced to a minimum at SG13.5 which displays a linear tendency. It is thus assumed that friction between the jaws and nut does not effect the strain gauges located at the shank.

8.5.2 Data Processing: Objective 1

In the following results associated with the objectives from section 8.4 are presented. Firstly the relative uncertainty is determined whereafter the final result is presented. The uncertainties

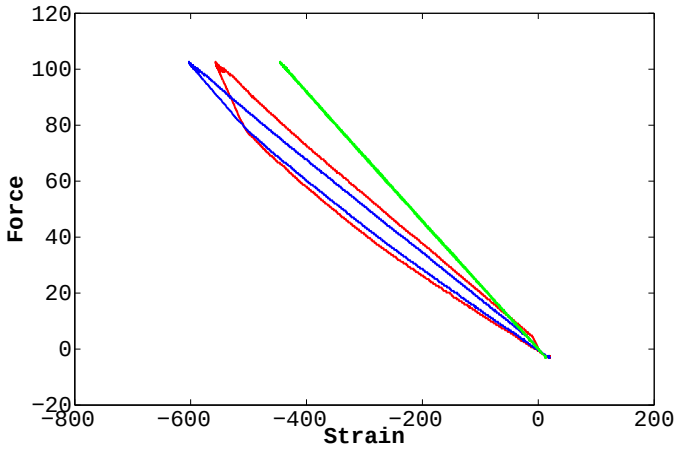

Figure 8.17: *Force strain plot for SG13.1, SG13.3, and SG13.5. Red: SG13.1, Blue:SG13.3, Green: SG13.5.*

associated with the dimensions and Poisson's ratio are neglected due to their relative small values.
Objective 1 is to determine if the applied load has the expected effect on the spanner in a well-known region. Using expression (8.36) and the collected data from table 8.2, the following results are obtained:

$$P_m = \frac{E\, I_z \bar{\varepsilon}_{SG3,4}}{|(SG3)A|_x\, h} \tag{8.64}$$

The relative uncertainty associated with $\bar{\varepsilon}_{SG3,4}$ is determined by:

$$\frac{s(\bar{\varepsilon}_{SG3,4})}{\bar{\varepsilon}_{SG3,4}} = \sqrt{2 \cdot \left(\frac{s(k)}{k}\right)^2 + \left(\frac{s(d_{SG3,4})}{d_{SG3,4}}\right)^2} \tag{8.65}$$

$$= \sqrt{2\,(0.5\%)^2 + \left(\frac{1.09\mu}{742\mu}\,100\%\right)^2} = 0.72\% \tag{8.66}$$

The relative uncertainty associated with the measured force P_m is determined by:

$$\frac{s(P_m)}{P_m} = \sqrt{\left(\frac{s(\bar{\varepsilon}_{SG3,4})}{\bar{\varepsilon}_{SG3,4}}\right)^2 + \left(\frac{s(E)}{E}\right)^2} = \sqrt{(0.72\%)^2 + (0.74\%)^2} = 1.03\% \tag{8.67}$$

Thus the measured force P_m can be determined as:

$$P_m = \frac{209GPa \cdot 2047mm^4 \cdot 742\mu}{181.5mm \cdot 17mm} = 103N;\; s(P_m) = 1.1N \tag{8.68}$$

It can be concluded the the applied load is within the uncertainties associated with the measured load. Thus there is coherence between the applied load and the measured load on the spanner.

8.5.3 Data Processing: Objective 2

The second objective is to ensure that the basic assumptions about the load condition are met. The undesired load are shown as red loads and denoted with a * on figure 8.11.

8.5.3.1 Tensile Force F_x^*

The tensile force F_x^* is controlled by measuring the normal stresses in the shank. The tensile force is estimated by:

$$F_x^* = \frac{AE\overline{\varepsilon}}{2} = \frac{b\,w\,E\left(\overline{\varepsilon}_{SG1} + \overline{\varepsilon}_{SG2}\right)}{2} \tag{8.69}$$

The relative uncertainties associated with $\overline{\varepsilon}_{SG1}$ are determined by:

$$\frac{s(\overline{\varepsilon}_{SG1})}{\overline{\varepsilon}_{SG1}} = \sqrt{2\left(\frac{s(k)}{k}\right)^2 + +2\left(\frac{s(d_{SG1})}{\overline{\varepsilon}_{SG1}}\right)^2 + \left(\frac{s(\alpha_{SG1})}{\overline{\varepsilon}_{SG1}}\right)^2} \tag{8.70}$$

Note that the factor 2 is present due to the uncertainties encumbered with the angular misplacement calculation performed below. The location of each strain gauge is associated with some uncertainties due to the measuring equipment used to place the gauge at the desired point. It is assumed that the strain gauges can have an angular misplacement of two degrees relative to the desired orientation. The relative uncertainties caused by angular misplacement for SG1 are determined in the following. Figure 8.18 illustrates the problem.

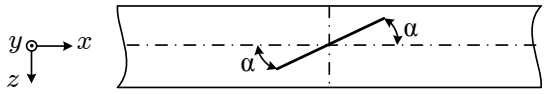

Figure 8.18: *Strain gauge where the angle α indicates the offset.*

If it is assumed that the strain gauge is tilted at the angle α, then the measured strain does not represent the desired measurement. For tension the desired measurement can be estimated by:

$$\varepsilon_i = \cos(\alpha)\,\varepsilon_D - \sin(\alpha)\,\varepsilon_D\,\nu \qquad \Rightarrow \tag{8.71}$$

$$\varepsilon_D = \frac{\varepsilon_i}{\cos(\alpha) - \sin(\alpha)\,\nu} \tag{8.72}$$

where:

	ε_i	Measured strain.
	ε_D	Desired strain measurement.
	ν	Poisson's ratio.
	α	Tilted angle of strain gauge.

The error can thus be estimated by:

$$\tilde{\alpha}_i = \varepsilon_D - \varepsilon_i = \frac{\varepsilon_i}{\cos(\alpha) - \sin(\alpha)\,\nu} - \varepsilon_i \tag{8.73}$$

where: $\tilde{\alpha}_i$ Estimated error due to angular misplacement for strain gauge *i*.

For SG1 the error estimate becomes:

$$s\left(\tilde{\alpha}_{SG1}\right) = \frac{290\mu}{\cos\left(2°\right) - \sin\left(2°\right)\cdot 0.28} - 290\mu = 3.0\mu \tag{8.74}$$

The relative uncertainties for $\overline{\varepsilon}_{SG1}$ thus become:

$$\frac{s(\overline{\varepsilon}_{SG1})}{\overline{\varepsilon}_{SG1}} = \sqrt{2\cdot(0.5\%)^2 + 2\cdot(0.14\%)^2 + \left(\frac{3.0\mu}{290\mu}100\%\right)^2} = 1.27\% \tag{8.75}$$

Using the same approach the relative uncertainties for $\overline{\varepsilon}_{SG2}$ is calculated to:

$$\frac{s(\overline{\varepsilon}_{SG2})}{\overline{\varepsilon}_{SG2}} = \sqrt{2\cdot(0.5\%)^2 + 2\cdot(0.17\%)^2 + \left(\frac{2.4\mu}{-268\mu}100\%\right)^2} = 1.17\% \tag{8.76}$$

If SG1 and SG2 are not placed directly above one another there will be a difference in the measured strain caused by the difference in moment contribution. This difference will have a significant influence on the result when calculating the normal strain, which is expressed by the difference in strains between SG1 and SG2. The relative uncertainties caused by misplacement along the x-axis for SG1 is determined in the following. It is assumed that one of the strain gauges is misplaced by 1 mm. Figure 8.19 illustrates the problem.

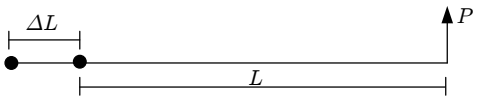

Figure 8.19: *Strain gauge placed an offset of ΔL away from its desired location.*

The increase of the moment arm is expressed by:

$$\frac{L+\Delta L}{L} = 1 + \frac{\Delta L}{L} \tag{8.77}$$

Calculation of the normal strains using SG1 and SG2 and adding the possible error associated with the moment contribution leads to:

$$\overline{\varepsilon}_{SG1} + \overline{\varepsilon}_{SG2} = \left(\varepsilon_N^{top} + \varepsilon_M^{top}\left(1 + \frac{\Delta L}{L}\right)\right) + \left(\varepsilon_N^{top} - \varepsilon_M^{top}\right) \tag{8.78}$$

$$= 2\varepsilon_N^{top} + \varepsilon_M^{top}\left(\frac{\Delta L}{L}\right) \tag{8.79}$$

$$= 2\varepsilon_N^{top} + \frac{\left(\overline{\varepsilon}_{SG1} - \overline{\varepsilon}_{SG2}\right)}{2}\left(\frac{\Delta L}{L}\right) \tag{8.80}$$

$$\tag{8.81}$$

The relative error can thus be expressed as:

$$L_n = \frac{\frac{\left(\overline{\varepsilon}_{SG1} - \overline{\varepsilon}_{SG2}\right)}{2}\left(\frac{\Delta L}{L}\right)}{\overline{\varepsilon}_{SG1} + \overline{\varepsilon}_{SG2}}100\% = \frac{\left(\overline{\varepsilon}_{SG1} - \overline{\varepsilon}_{SG2}\right)\frac{\Delta L}{L}}{2\left(\overline{\varepsilon}_{SG1} + \overline{\varepsilon}_{SG2}\right)}100\% \tag{8.82}$$

$$= \frac{\left(290\mu + 268\mu\right)\cdot\frac{1mm}{141.5mm}}{2\cdot\left(290\mu + (-268\mu)\right)}100\% = 9\% \tag{8.83}$$

Collecting all the uncertainties associated with expression (8.69) leads to:

$$\frac{s(F_x^*)}{F_x^*} = \sqrt{\left(\frac{1}{2}\frac{s(\overline{\varepsilon}_{SG1})}{\overline{\varepsilon}_{SG1}}\right)^2 + \left(\frac{1}{2}\frac{s(\overline{\varepsilon}_{SG2})}{\overline{\varepsilon}_{SG2}}\right)^2 + \left(\frac{s(E)}{E}\right)^2 + (L_n)^2} \tag{8.84}$$

$$= \sqrt{\left(\frac{1}{2}1.8\%\right)^2 + \left(\frac{1}{2}1.7\%\right)^2 + (0.74\%)^2 + (9\%)^2} = 9.1\% \tag{8.85}$$

The tensile force F_x^* can thus be calculated as:

$$F_x^* = \frac{b\,w\,E\left(\overline{\varepsilon}_{SG1} + \overline{\varepsilon}_{SG2}\right)}{2} \tag{8.86}$$

$$= \frac{17mm \cdot 5mm \cdot 209GPa \cdot (290\mu - 268\mu)}{2} = 195N; s(F_x^*) = 18N \tag{8.87}$$

As seen from expression (8.87), the tensile force exceeds the applied force by almost a factor of two, which indicates that the two strain gauges are not measuring the correct value. If all the uncertainties are added together to simulate a worst case scenario, the tensile force can be calculated to:

$$F_x^* = 17mm \cdot 5mm \cdot 209GPa \cdot (290\mu - 268\mu - 6\mu) = 88N \tag{8.88}$$

Even when all the uncertainties are collected so as to give an unlikely outcome, the result is still above what would be expected for the experiment. If the distance ΔL is increased to $3.1mm$, so a greater part of the moment contribution is accounted for, the tensile force reduces to zero N. This does by visual inspection not seem to be the case. If the two strain gauges are used to calculate the magnitude of the applied force the result is 99 N, with an uncertainty of 9 N. It is thus believed that the unrealistic magnitude of the tensile force must be the result of a small systematic error which can not be accounted for. Examples of such errors could be: Bad contact between a strain gauge and the test specimen, a soldering with increased resistance, or a bad stain gauge. The best way to eliminate such an error, is to redo the experiment with new strain gauges, wires, and test specimen. This option has not been chosen, because the other results seem credible due to the low associated uncertainties and good coherence with the expected results.

8.5.3.2 Bending Force F_z^* and Moment M_y^*

The presence of the bending moment M_y^* would result in an out of plane stress condition, which is not desired in the experiments. The moment is determined by:

$$M_y^* = -\frac{E\,I_y\,\overline{\varepsilon}_{SG6,7^{0\circ}}}{w} \tag{8.89}$$

The uncertainties concerning the measurement are expressed by:

$$\frac{s(\overline{\varepsilon}_{SG6,7^{0\circ}})}{\overline{\varepsilon}_{SG6,7^{0\circ}}} = \sqrt{2\left(\frac{s(k)}{k}\right)^2 + \left(\frac{s(d_{SG6,7^{0\circ}})}{\overline{\varepsilon}_{SG6,7^{0\circ}}}\right)^2} \tag{8.90}$$

$$= \sqrt{2 \cdot (0.5\%)^2 + \left(\frac{0.85\mu}{-4.6\mu}\,100\%\right)^2} = 18.49\% \tag{8.91}$$

The collected uncertainties associated with the bending moment is expressed by:

$$\frac{s(M_y^*)}{M_y^*} = \sqrt{\left(\frac{s(\overline{\varepsilon}_{SG6,7^{0\circ}})}{\overline{\varepsilon}_{SG6,7^{0\circ}}}\right)^2 + \left(\frac{s(E)}{E}\right)^2} = \sqrt{(18.49\%)^2 + (0.74\%)^2} = 18.5\% \tag{8.92}$$

The magnitude of the bending moment is determined as:

$$M_y^* = -\frac{E\,I_y\,\overline{\varepsilon}_{SG6,7^{0\circ}}}{w} = -\frac{209GPa \cdot 177mm^4 - 4.6\mu}{5mm} = 34Nmm; s(M_y^*) = 6.3Nmm \tag{8.93}$$

The force which causes the moment is determined as:

$$F_z^* = \frac{M_y^*}{|(SG6)A|_x} = \frac{34Nmm}{181.5mm} = 0.2N; s(F_z^*) = 0.04N \tag{8.94}$$

where: $|(SG6)A|_x$ The x-component of the vector from SG6 to point A.

As can be seen from the above result the force out of plane can be regarded as zero. Thus ensuring the basic assumption of in plane stress throughout the experiments.

8.5.3.3 Torsional moment M_x^*

The presents of the torsional moment M_x^* is indicated by SG6$^{45^\circ}$, SG6$^{-45^\circ}$, SG7$^{-45^\circ}$ and SG7$^{45^\circ}$, which are coupled in a full bridge. The uncertainties related with the measurement are described by:

$$\frac{s\left(\overline{\varepsilon}_{SG6,7^{\pm45^\circ}}\right)}{\overline{\varepsilon}_{SG6,7^{\pm45^\circ}}} = \sqrt{4\left(\frac{s(k)}{k}\right)^2 + \left(\frac{s(d_{SG6,7^{\pm45^\circ}})}{\overline{\varepsilon}_{SG6,7^{\pm45^\circ}}}\right)^2} \tag{8.95}$$

$$= \sqrt{4\cdot(0.5\%)^2 + \left(\frac{0.28\mu}{-3.4\mu}100\%\right)^2} = 8.3\% \tag{8.96}$$

The collected uncertainties associated with the torsional moment are expressed by:

$$\frac{s(M_x^*)}{M_x^*} = \sqrt{\left(\frac{1}{4}\frac{s\left(\overline{\varepsilon}_{SG6,7^{\pm45^\circ}}\right)}{\overline{\varepsilon}_{SG6,7^{\pm45^\circ}}}\%\right)^2 + \left(\frac{1}{2}\frac{s(E)}{E}\%\right)^2} \tag{8.97}$$

$$= \sqrt{\left(\frac{1}{4}8.3\%\right)^2 + \left(\frac{1}{2}0.74\%\right)^2} = 2.1\% \tag{8.98}$$

The torsional moment can be estimated by:

$$M_x^* = \frac{1}{2}\overline{\varepsilon}_{SG6,7^{\pm45^\circ}}\frac{E}{2(1+\nu)}\alpha_{M_x^*}\,b\,w^2 \tag{8.99}$$

$$= \frac{1}{2} - 3.4\mu\frac{209GPa}{2\cdot(1+0.28)}0.274\cdot17mm\cdot(5mm)^2 = -16Nmm; s(M_x^*) = 0.3Nmm \tag{8.100}$$

Due to the relatively small magnitude of the torsion the effects are neglected and the torsion assumed to be zero.

8.5.3.4 Bending moment M_x^*

The strains measured by SG11$^{90^\circ}$ and SG12 are compared to check for the existence of a bending moment around the x-axis. The associated uncertainties are expressed by:

$$\frac{s(\overline{\varepsilon}_{SG11^{90^\circ}})}{\overline{\varepsilon}_{SG11^{90^\circ}}} = \sqrt{2\left(\frac{s(k)}{k}\right)^2 + 2\left(\frac{s(d_{SG11^{90^\circ}})}{\overline{\varepsilon}_{SG11^{90^\circ}}}\right)^2 + \left(\frac{s(\alpha_{SG11^{90^\circ}})}{\overline{\varepsilon}_{SG11^{90^\circ}}}\right)^2} \tag{8.101}$$

$$= \sqrt{2\cdot(0.5\%)^2 + 2\cdot\left(\frac{0.5\mu}{-85\mu}100\%\right)^2 + \left(\frac{0.8\mu}{-85\mu}100\%\right)^2} = 1.44\% \tag{8.102}$$

$$\tag{8.103}$$

And for SG12

$$\frac{s(\overline{\varepsilon}_{SG12})}{\overline{\varepsilon}_{SG12}} = \sqrt{2\cdot(0.5\%)^2 + 2\cdot\left(\frac{0.3\mu}{-59\mu}100\%\right)^2 + \left(\frac{0.5\mu}{-59\mu}100\%\right)^2} = 1.32\% \tag{8.104}$$

Subtracting the measured strains for $SG11^{90^\circ}$ from SG12 results in the strains which would indicate a moment about the x-axis.

$$\varepsilon_{M_x^*} = \frac{1}{2}\left(\overline{\varepsilon}_{SG11^{90^\circ}} - \overline{\varepsilon}_{SG12}\right) \tag{8.105}$$

$$= \frac{1}{2}\left(-85\mu - (-59\mu)\right) = -13\mu; s(\varepsilon_{M_x^*}) = 0.17\mu \tag{8.106}$$

$$\tag{8.107}$$

Due to the relative small magnitude of the measured strain the moment M_x^* is considered negligible.

8.5.4 Data Processing: Objective 3 and 4

Based on the results from objectives one and two the experiment meets the requirements consented with in plane loading and plane stress. Thus the information collected from the strain gauges mounted on the jaws and in region three, are assumed to be valid. The results from these strain gauges are listed in table 8.2.
Using the strains obtained from the rosette in region three, the associated strain tensor is determined.

$$\varepsilon_{11} = \overline{\varepsilon}_{SG11^{0^\circ}} = 215\mu; s(\varepsilon_{11}) = 5\mu \tag{8.108}$$

$$\varepsilon_{12} = \overline{\varepsilon}_{SG11^{45^\circ}} - \frac{1}{2}\left(\overline{\varepsilon}_{SG11^{0^\circ}} + \overline{\varepsilon}_{SG11^{90^\circ}}\right) = -109\mu; s(\varepsilon_{12}) = -2\mu \tag{8.109}$$

$$\varepsilon_{22} = \overline{\varepsilon}_{SG11^{90^\circ}} = -85\mu; s(\varepsilon_{22}) = -1.6\mu \tag{8.110}$$

Thus the strain tensor becomes:

$$\varepsilon_{SG11} = \begin{pmatrix} 215 & -109 \\ -109 & -85 \end{pmatrix} \tag{8.111}$$

Chapter

9

Measurements by Digital Image Correlation

Measurements have also been conducted using Digital Image Correlation (DIC). In this chapter first a brief introduction to the underlying theory is given. Next, results from the actual DIC measurements are presented.

9.1 Theory of DIC

Digital Image Correlation is a technique to translate images of a deformed structure into displacements and strains. DIC is based on pictures taken of a structure in both undeformed and deformed state. Such pictures can be treated using DIC-methods to give displacements and strains. Thus the fundamentals of DIC is basically some advanced mathematics that can treat the data obtained from images of a structure into engineering quantities, which then can be used for structural analysis of the specific part.
In this section an overview of the experimental setup is given together with a very short introduction to the underlying theory of the method. The section is based on Sutton and Chu [13, 14, 15]. It should be noted that since two of these references are more than 20 years old, the technique must indisputably have developed considerably since. It is, however, beyond the scope of this text to account for these developments.

9.1.1 Experimental Setup

Before the experiment can be conducted the specimen up for examination must be attached a random speckle. This is done by spray painting the specimen with what seems to be a random speckle of very small spots. Whether the hereby obtained speckle is sufficiently random can later be determined by the experimental equipment.
The principle of the experimental setup is sketched in figure 9.1. The specimen under examination is illuminated with one or more light sources. The deformations of the specimen during load is captured with a camera. The images from the camera are digitalised in a *digitiser* before these are sent to a computer where all data acquisitioning is performed [14]. Of course nowadays the analog camera connected to a digitiser can be replaced by a digital camera connected directly to the computer.
One very common expansion of the basic experiment is to use more cameraes in order to capture more degrees of freedom of the specimen. E. g. the use of two cameraes can be used to capture displacements in 3D. Two cameras are placed in different angles to the specimen to get

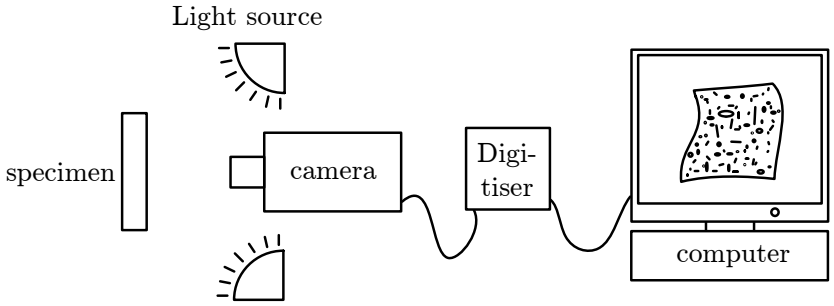

Figure 9.1: *Overview of the setup of a DIC experiment.*

two 2D images of each speckle. Since the speckles are all different they can be recognised in the two images and thereby the 3D displacement can be calculated.

9.1.2 Brief Introduction to the Underlying Theory

When the images from the camera have been digitalised, the intensity of light over the specimen is converted into a graylevel representation. That is, a number for each pixel indicating how dark the pixel is. The transformation of a random speckle into a pixelised graylevel representation is illustrated in figure 9.2.

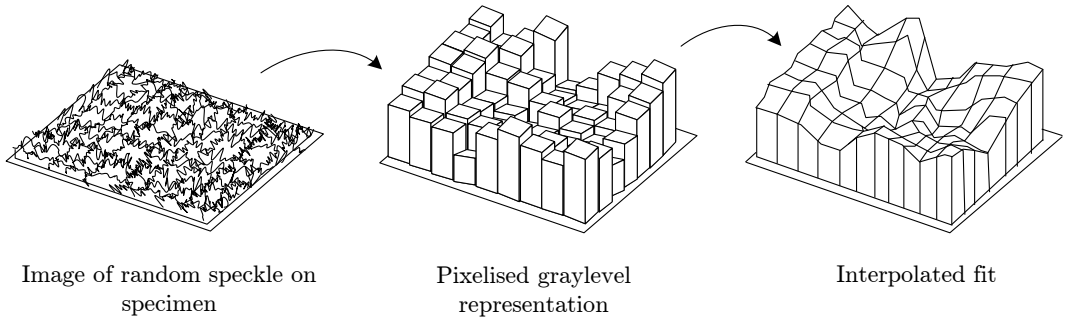

Figure 9.2: *Illustration of how the random speckle on the specimen is converted into a pixelised graylevel representation, which then is interpolated using interpolation functions.*

Since this discrete form of data is not the most advantageous form for the analysis, it is desired to construct a more useful model of the intensity pattern. This is done by interpolating between the discrete values using interpolation functions—that is, polynomials of some desired order. The resulting intensity pattern after this interpolation is also sketched in figure 9.2. These fitting routines are done for all obtained images. The fitted intensity images are all stored in the computer. Suppose in the following that a two-dimensional intensity fit for the undeformed object is stored in array $\bar{\bar{A}}$ in the computer and a two-dimensional intensity fit for the same object in deformed state is stored in array $\bar{\bar{B}}$ in the computer.
In order to process the obtained intensity fits, one must first assume a mathematical relationship between these fits and the actual object deformation. It is here assumed that small subsets of array $\bar{\bar{B}}$ are related to small subsets of array $\bar{\bar{A}}$ by a homogeneous linear mapping, and that this mapping is the same as the mapping which applies to the deformation of the object surface which originally omitted the intensity pattern [13]. The assumed mapping is illustrated in figure 9.3.

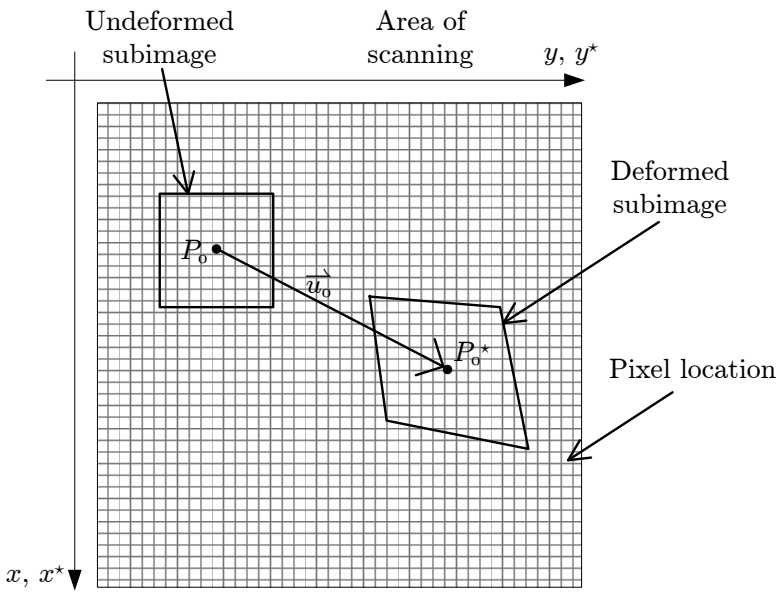

Figure 9.3: *Illustration of the homogeneous linear mapping that relates small subsets from the deformed subimage $\bar{\bar{B}}$ to small subsets from the undeformed subimage $\bar{\bar{A}}$.*

All that now remains for the analysis is the actual computation of these mapping parameters. With the assumed mapping the deformed position $\vec{x}^*$ of an arbitrary point $\vec{x}$ is given by:

$$(\vec{x}^*)_i = (\vec{x})_i + (\vec{u})_i + \frac{\partial(u_i(\vec{x}))}{\partial x_j} dx_j \qquad i,j = 1,2 \tag{9.1}$$

where:

$\vec{x}^*$	The deformed position vector.
$\vec{u}$	The vector displacement field.
$\frac{\partial(u_i(\vec{x}))}{\partial x_j}$	The deformation gradient at point $\vec{x}$.
i,j	Indices refer to vector components.

In order to determine the displacement field and the deformation gradient a small subset from the undeformed image is chosen, centred at P_0. This small subset is then moved and distorted homogeneously cf. equation 9.1. Next it is compared with the deformed array $\bar{\bar{B}}(\vec{x})$. The deformations which give the minimum difference in intensity is then considered as the mapping parameters. Analytically this corresponds to minimising the following correlation coefficient [13]:

$$C(u_i, \tfrac{\partial u_i}{\partial x_j}) = \int\int_{\Delta M} \left[\bar{\bar{A}}(\vec{x}) - \bar{\bar{B}}(\vec{x})\right]^2 d\vec{x} \qquad i,j = 1,2 \tag{9.2}$$

where:

$\bar{\bar{A}}(\vec{x})$	The digital form of the scalar intensity field of the deformed image.
ΔM	subset in deformed image.

This coefficient is typically minimised in the computer using some iterative process depending on the specific software.
It should be noted that a theorem of the theory of elasticity is that there exists a subset within any body whose deformations might be expressed as a homogeneous linear mapping. Thus, if the subset are set sufficiently small the method should be useful for both small and large deformations.

Hence by this approach the deformations of a body can be determined. By the use of a strain definition such as Lagrange's strain tensor cf. equation (5.26) the strains of the specimen can thus be determined.

9.1.3 Further Aspects to Consider

Above a brief introduction to the underlying theory of DIC was given. However, in practice a lot of other aspects might influence the results. Parameters such as random noise, uneven lightning, and non-random speckles on the specimen might very well influence the results significantly. None of these effects can be allowed for using the above methods. Advanced DIC-equipment is, however, capable of taking some of these effects into account. A description of such techniques can be found in Sutton et al. [15]. However, the theory of these techniques reach beyond the scope of this text. Hence, such techniques are just used when found readily available in the used software without further elaborations.

9.2 DIC Results

Digital Image Correlation was used in this project as a supplement to strain gauge measurements in the purpose of validation FEA. The concerned areas were the two jaws and the transition between the straight shank and the fork end. In this project the optical measuring system ARAMIS has been used. The optical measuring experiments have been done with the same spanner model that was used during the strain gauge measurements. The areas subjected to ARAMIS analysis were stripped for strain gauges and painted white with a black random pattern of small spots as exemplified in figure 9.4.

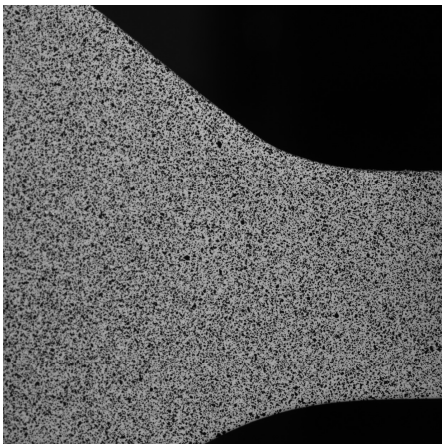

Figure 9.4: *The pattern in the measuring area has to be random, and the spots should not be too large. This illustration shows the transition between the shank and the fork end.*

The spanner was set up in the test rig and 100N wes applied. The ARAMIS system measured the strains in the concerned areas, and wrote the results in form of colour plots where the stains in the model were displayed. In order to compare the results of DIC with other results that are known to be reliable, an ANSYS model was set up using QM6 elements. In order to compare the ARAMIS results with ANSYS results the colour scale needed to be the same. In ANSYS it is possible to define both the number of colour levels and the value of them, but any strain values outside a user defined scale is coloured grey. To ease the comparison of plots, the boundary colours of the ANSYS plots were filled out to the edges. That way the grey zones were coloured, but the boundaries where this retouching has been done were marked with black lines. Thus

it is possible to see where the boundary colours would continue to be intensified, but at the same time keep the same scale as the ARAMIS plots. It was believed that if the results from both methods were plotted with the same strain scale, the result would look like each other and the credibility of the FEA would still be intact.

In general DIC has shown to be unable to give shear strains since these are simply too small to measure while in the elastic region. Hence when results are presented in the following, no shear strains are shown.
The results from the ARAMIS measurements contained some distortion. This was minimised by defining a larger number of points to calculate and plot the average of these. Thus the results look smoother, and the accuracy is not considered to be lower than a plot with noticeable noise. Below the results from ARAMIS are presented together with the ANSYS results with the same colour levels and scale. The results from the transition area are compared in figure 9.5 and 9.6.

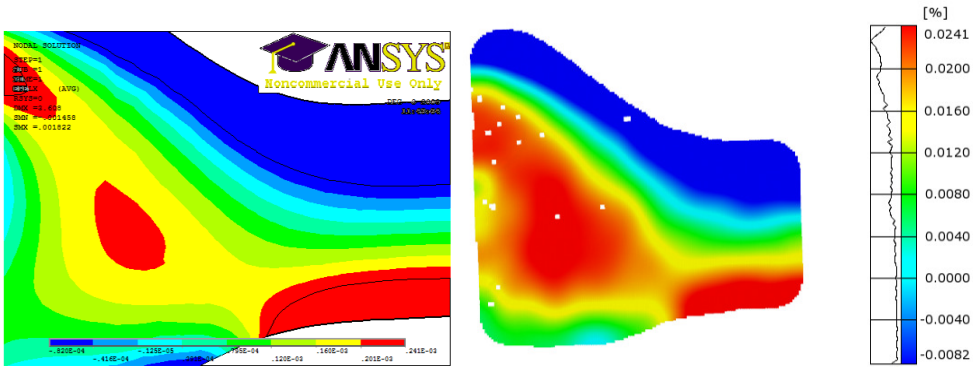

Figure 9.5: *The ANSYS result (left) and the ARAMIS result (right) for the transition between the shank and the fork end with respect to the strain in horisontal (X) direction.*

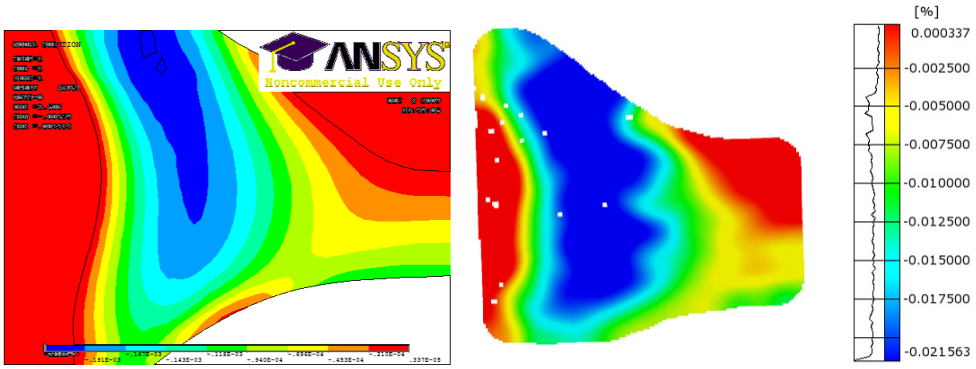

Figure 9.6: *The ANSYS result (left) and the ARAMIS result (right) for the transition between the shank and the fork end with respect to the strain in vertical (Y) direction.*

Figure 9.5 shows that ANSYS and ARAMIS have got very similar results for horisontal strain. The blue compression area in top of the spanner together with the red extended areas in the bottom of the shank and in the centre of the fork section are all clearly recognizable in both plots. The green lines, which are close to neutral, parts the compression and extension in the same way in both plots. In figure 9.6 it is shown that the vertical strain results from ANSYS and ARAMIS match satisfactory. Both plots have got the major extension zones in top of the shank and in the left area of the fork section, and the major compression zone in the centre of the

transition area spreading from the top. The rising and decreasing intensity of the surrounding strains also look convincingly equal.

The results from the upper jaw are compared in figure 9.7 and 9.8.

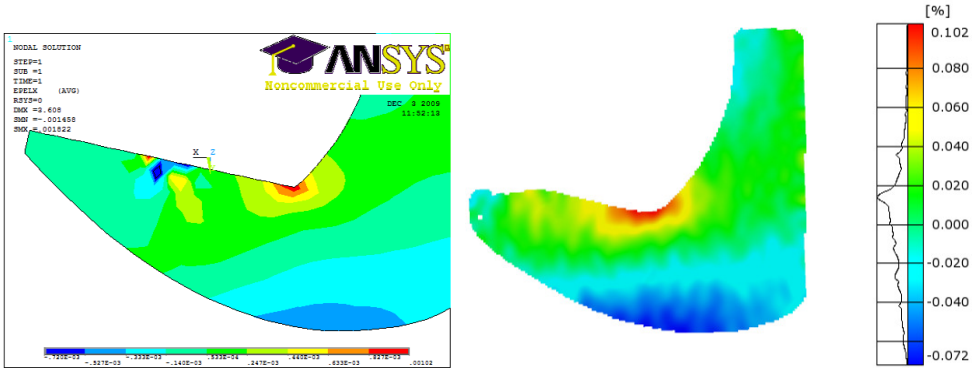

Figure 9.7: *The ANSYS result (left) and the ARAMIS result (right) for the upper jaw with respect to the strain in horisontal (X) direction. Please note that the upper jaw is at the bottom because the spanner is mounted upside down in the test rig.*

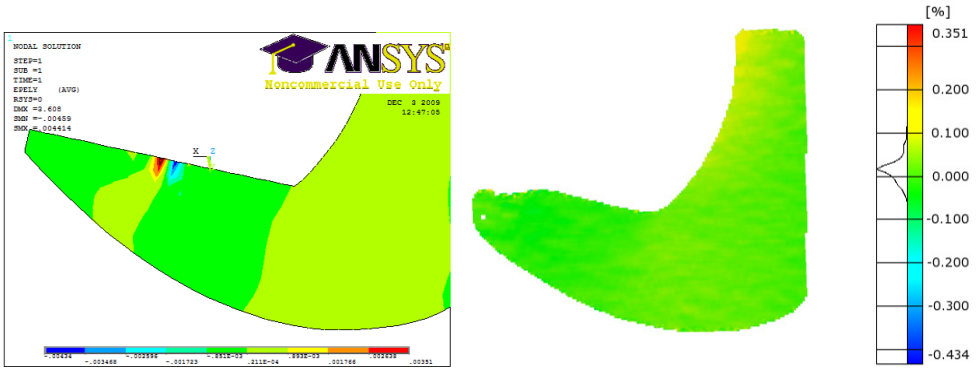

Figure 9.8: *The ANSYS result (left) and the ARAMIS result (right) for the upper jaw with respect to the strain in vertical (Y) direction. Please note that the upper jaw is at the bottom because the spanner is mounted upside down in the test rig.*

In figure 9.7 and 9.8 one major difference stands out. The ANSYS plot yields large strains in the contact area between the jaw and the nut. This is because the constraints that have been modelled are not completely equivalent to the real life. As seen in the plots this makes some local differences, but apart form a small area around the constraints the jaw plots from ANSYS and ARAMIS are very similar. Figure 9.7 shows some extension around the inner edge and corner of the jaw which stretches further to the right into the body. An area of compression can be seen along the outer edge of the jaw. Figure 9.8 expose very small strains, but there is a tendency to some extension along the edge between the jaws in both plots.

The results from the lower jaw are compared in figure 9.9 and 9.10.

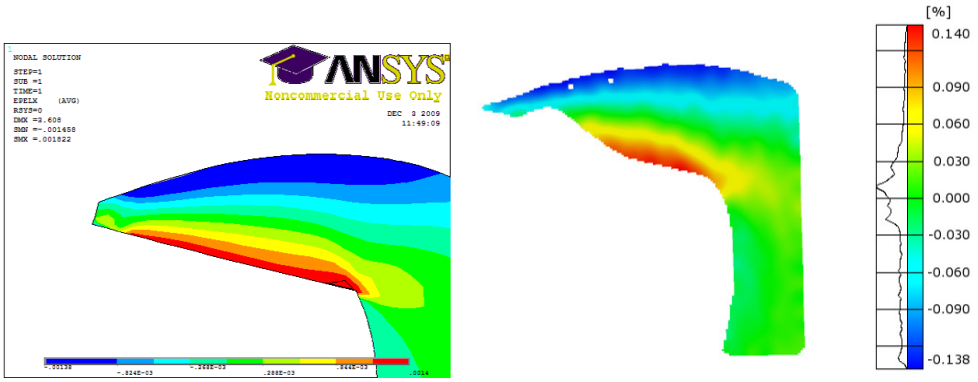

Figure 9.9: *The ANSYS result (left) and the ARAMIS result (right) for the lower jaw with respect to the strain in horisontal (X) direction. Please note that the lower jaw is at the top because the spanner is mounted upside down in the test rig.*

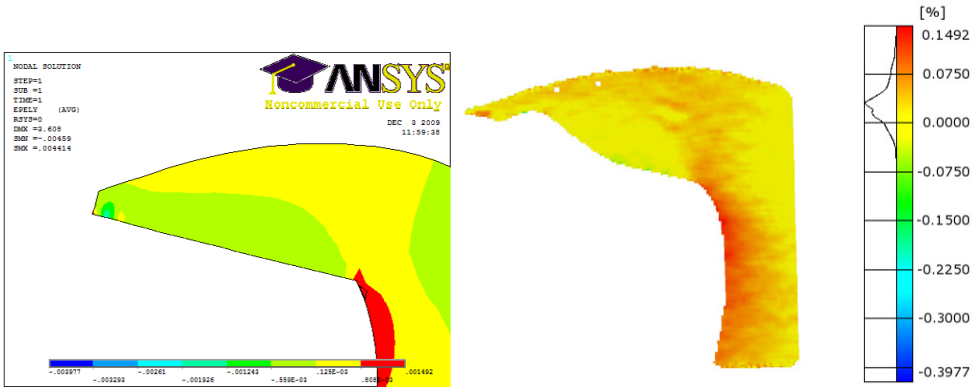

Figure 9.10: *The ANSYS result (left) and the ARAMIS result (right) for the lower jaw with respect to the strain in vertical (Y) direction. Please note that the lower jaw is at the bottom because the spanner is mounted upside down in the test rig.*

During the DIC experiments a bolt head on the test rig blocked the view of some of the inner edge of the jaw. However, what could be seen by the camera can still be compared. In figure 9.9 it can be seen that the major extension occurs along the inner edge of the jaw and is propagated further into the spanner body. The major blue compression zone lies along the outer edge, and there is a tendency to a small compression along the edge between the jaws. This distribution of strain can be seen clearly in both the ANSYS and the ARAMIS plots. Figure 9.10 also shows satisfactory equality between the two plots. As seen for the upper jaw in figure 9.8, the lower jaw also experiences very small vertical strains except from a zone that stretches along the edge between the jaws and straight over to the outer edge.

One test was also executed with a larger force than the initial test force. Figure 9.11 and 9.12 compares the ANSYS and ARAMIS results from the lower jaw affected by a test force of 180N.

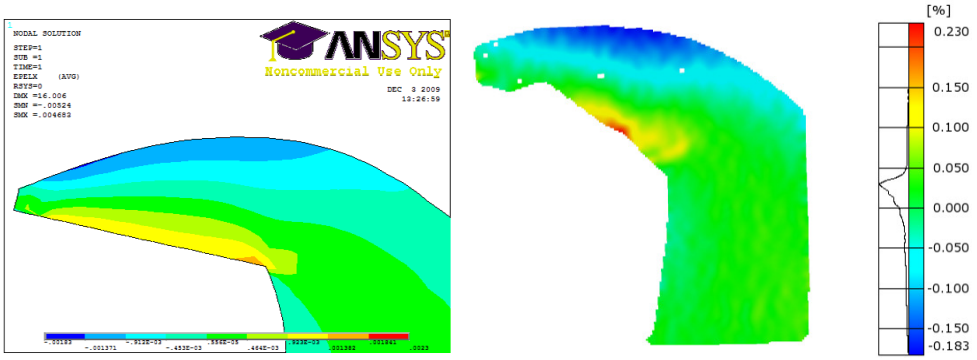

Figure 9.11: *The ANSYS result (left) and the ARAMIS result (right) for the lower jaw at 180N with respect to the strain in horisontal (X) direction. Please note that the lower jaw is at the top because the spanner is mounted upside down in the test rig.*

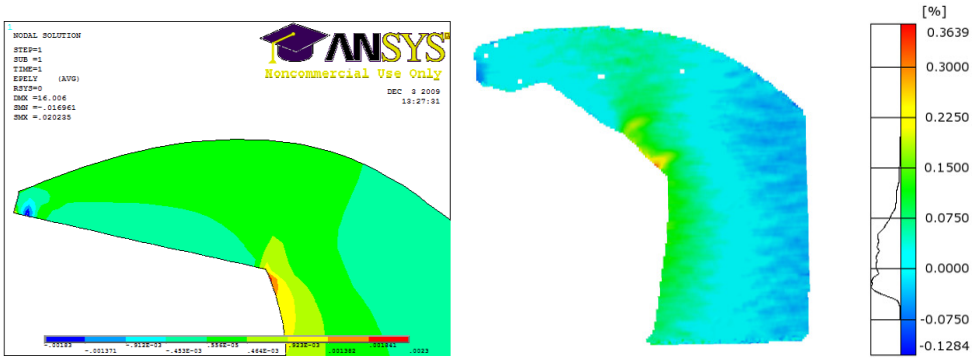

Figure 9.12: *The ANSYS result (left) and the ARAMIS result (right) for the lower jaw at 180N with respect to the strain in vertical (Y) direction. Please note that the lower jaw is at the bottom because the spanner is mounted upside down in the test rig.*

Figure 9.11 and 9.12 show the strains in the lower jaw when the spanner was subjected to a force of 180N. It can be seen that also with a larger force the plot from ANSYS and ARAMIS are very close to each other. The strain distribution is clearly the same as the distribution at 100N shown in figure 9.9 and 9.10, but the strain values are larger.

None of the plots above have any fundamental deviations from each other like considerable strain in opposite directions, large value differences etc. Based on the comparisons between the different plots above it can be concluded that in this project the ANSYS results and the ARAMIS results have got substantial equality.

Chapter

10

Finite Element Theory

In order to perform an FE analysis of the spanner it is important to outline the fundamental theory of finite elements. This is done considering application in structural mechanics of linear behaviour. Other areas of application are not of interest in this text. The principal of variational methods is addressed leading to the approximate Rayleigh-Ritz method and thereby formulating the FE form for linear structural mechanics. Subsequently the bilinear Q4 element and the Q4 isoparametric element are dealt with addressing pros and cons leading to methods that compensate for certain deficiencies. Next the approach for determining strains and stresses is presented. In closing the FEA program DMS7FEA is described and the the approach of FE analysis using reduced integration with hour glass control compared to commercial code.

The following content of this chapter is mainly derived in accordance to Shames and Dym [7] and Cook, Malkus, Plesha, and Witt [16].

10.1 Extremisation using The Variational Method

Many problems in structural mechanics can be formulated by differential equations by application of Newton's laws or theory of elasticity when dealing with a continuum, e.g. equations of motion of a multi body system or the equilibrium equations for a continuum subject to loading. However these formulations of differential equations can be difficult to obtain for complex structures or continuums. Another formulation technique requires introduction of the concept *functionals*. A functional is defined as an integral expression of a function depending on one or more variables and possibly their derivatives of first or higher order. An example of a functional I is

$$I = \int_{x_1}^{x_2} F(x, y, y')\,dx \tag{10.1}$$

The purpose of formulating a problem in structural mechanics as a functional is to determine the function y which makes the functional I extreme. I.e. I obtains a numerical value for every function that is put under the integral but only a minimum or maximum value is obtained by y. Given that y is twice differentiable extremising I corresponds to solving the same problem formulated by a differential equation. By calculus of variations as set forth by Shames and Dym the condition which is required for y to make I extreme is given by the Euler-Lagrange differential equation [7, p. 73]

$$\frac{\partial F}{\partial y} - \frac{d}{dx}\left(\frac{\partial F}{\partial y'}\right) = 0\,, \quad x_1 < x < x_2 \tag{10.2}$$

As formulated by Olhoff this differential equation is satisfied by the C^2 continuous function y with boundary conditions $y(x_1) = y_{x_1}$ and $y(x_2) = y_{x_2}$ which makes the functional I extreme [17, p. 6]. So it can be stated that for a structural mechanics problem involving a continuum the Euler-Lagrange equation is the governing differential equation, e.i. the equilibrium equation, if y extremises I.

If the boundary conditions $y(x_1) = y_{x_1}$ and $y(x_2) = y_{x_2}$ are not prescribed then the natural boundary conditions must be satisfied. For the functional given in (10.1) the natural boundary conditions are given by

$$\left(\frac{\partial F}{\partial y'}\right)_{x=x_1} = 0\,, \quad \left(\frac{\partial F}{\partial y'}\right)_{x=x_2} = 0 \tag{10.3}$$

The formulation of the functional provides an alternative method for solving linear structural problems involving a continuum. Instead of formulating the problem directly by a differential equation it can be solved by expressing e.g. the potential energy of an elastic body as a functional. As described in the preceding extremising the potential energy of the body formulated as a functional will yield equilibrium. From the state of equilibrium information such as deformation due to loading can be obtained. When solving a problem by the approach of extremising a functional, what is obtained is an analytical solution which is determined in an averaged sense. This is why the concept allowable *variation* of y described by Shames and Dym can be introduced [7]. So the solution satisfies the boundary conditions $y(x_1) = y_{x_1}$ and $y(x_2) = y_{x_2}$ if prescribed and fulfills the natural boundary conditions of equation (10.3) in an averaged sense and vice versa. A functional implicitly containing the governing differential equation is said to be expressed in *weak form*. The problem directly expressed by a governing differential equation is said to be of *strong form*. The Rayleigh-Ritz method has originated from the formulation technique of functionals.

10.2 The Rayleigh-Ritz Method

The Rayleigh-Ritz method is developed from the idea of extremising a functional. When solving a problem by the approach of extremising a functional an analytical solution is obtained. In contrast the Rayleigh-Ritz method gives an approximate solution. For a continuum of complex geometry with infinitely many d.o.f. it can be difficult, if not impossible, to formulate the integral expression of the functional. This is a motivation for introducing an approximate method such as the Rayleigh-Ritz method. The idea, when trying to solve structural mechanics problems, is to formulate an expression for the potential energy of an elastic continuum, not as a functional but instead as an approximate expression. This is done by approximating the displacement field that expresses the potential energy of the body as described by Robert D. Cook, David S. Malkus, Michael E. Plesha, and Robert J. Witt [16, p. 146]

$$u = \sum_{i=1}^{l} a_i f_i\,, \quad v = \sum_{i=l+1}^{m} a_i f_i\,, \quad w = \sum_{i=m+1}^{n} a_i f_i \tag{10.4}$$

where:

u, v, w	The displacement fields in the x-, y-, and z-direction respectively.
a_i	The generalised d.o.f. or generalised coordinates.
f_i	The function used to approximate the displacement field.

The functions f_i must satisfy essential boundary conditions and ensure compatibility. f_i need not satisfy natural boundary conditions but doing so yields a more accurate approximation as

	Bar	**Beam in bending**
Differential equation	$AEu_{,xx}+q=0$	$EIv_{,xxxx}-q=0$
$2m$, $m-1$, $2m-1$	2, 0, 1	4, 1, 3
essential B.C.	On u only	On v and $v_{,x}$
nonessential B.C.	On $\sigma_x = Eu_{,x}$	On $M = EIv_{,xx}$ and $V = EIv_{,xxx}$

Table 10.1: *Table outlining the essential and nonessential boundary conditions.*

stated by Robert D. Cook, David S. Malkus, Michael E. Plesha, and Robert J. Witt [16, p. 147]. It is important to underline that the potential energy is no longer formulated as a functional but as a function of the approximated displacement field. That is if the potential energy is sought extremised, the partial derivative with respect to a_i is set equal to zero. If the total potential energy is Π_p, then stationarity of Π_p requires

$$\frac{\partial \Pi_p}{\partial a_i} = 0, \quad a_i = 1, 2, ..., n \tag{10.5}$$

What is obtained is an approximate model with a finite number of d.o.f. expressed by algebraic equations and no differential equations need to be solved. In contrast to the method of functionals there is no averaged solution to all infinitely many points in the structure but only in the finite number of d.o.f.

The displacement functions u, v, and w must as mentioned be admissible, which means that they must fulfill essential boundary conditions. This leads to a definition on type of boundary conditions (B.C.). There are two categories of B.C., *essential* and *nonessential* B.C. The *nonessential* also referred to as *natural* B.C. The definition states that $2m$ is the highest order of derivative of the dependent variable, here the displacements u, v, and w, in the governing differential equation. The *essential* B.C. involve the $m-1$ derivative down to the derivative of order zero. Derivatives of order m up to $2m-1$ are *nonessential* B.C. Table 10.1 gives two examples of an axially loaded bar and a beam in bending as by Robert D. Cook, David S. Malkus, Michael E. Plesha, and Robert J. Witt [16, p. 152].
In order to derive the algebraic equations, which are solved in the FE form of the Rayleigh-Ritz method, attention is brought upon the total potential energy of an elastic body.

10.2.1 Total Potential Energy of an Elastic Body

The total strain energy within an elastic body is given as

$$U_e = \int_V U_0 dV = \frac{1}{2}\int_V \vec{\sigma}^T \vec{\varepsilon} dV = \frac{1}{2}\int_V \vec{\varepsilon}^T \bar{\bar{E}}\, \vec{\varepsilon} dV \tag{10.6}$$

where:

U_e	Total strain energy in an elastic body.
U_0	The strain energy density.
$\vec{\sigma}$	The stress vector transposed containing six stress components.
$\vec{\varepsilon}$	The strain vector containing six strain components.
$\bar{\bar{E}}$	The constitutive matrix. Symmetric for isotropic materials.

This is true if initial stresses and strains are neglected. The total potential energy of an elas-

tic body under conservative loads is

$$\Pi_p = U_e + \Omega \tag{10.7}$$

where: Ω Total potential of applied loads.

For a conservative system where the work done by external and internal forces are path independent the total potential energy of an elastic body is given by

$$\Pi_p = \frac{1}{2}\int_V \vec{\varepsilon}^T \bar{\bar{E}} \vec{\varepsilon} dV - \int_V \vec{u}^T \vec{F} dV - \int_S \vec{u}^T \vec{\Phi} dS - \vec{D}^T \vec{P} \tag{10.8}$$

where: $\vec{F}$ Body forces applied to the elastic body.

$\vec{\Phi}$ Surface tractions applied to the body.

$\vec{P}$ The external applied force(s).

$\vec{u}$ The displacements due to body forces and surface tractions.

$\vec{D}$ Displacements due to the external applied force(s).

The first integral term accounts for work done by internal forces in the elastic body. The last three terms account for potential lost to do work as the body deforms. That is the forces $\vec{F}$, $\vec{\Phi}$, and $\vec{P}$ lose potential to do work as the body deforms by $\vec{u}$ and $\vec{D}$. The sign convention of the minus sign in equation (10.8) is valid when the force acts in the positive direction of the coordinate axis and the deformation is in that direction. In a time independent structural mechanics problem the force is considered to act at full magnitude at the instance of a given deformation. Thus giving equation 10.8 for the total potential energy.

10.2.2 Application of The Rayleigh-Ritz Method in FEA of Structural Mechanics

If stationarity is required of the total potential energy, equation (10.5) is applied on expression (10.8). The task of demanding stationarity using the Rayleigh-Ritz method is to approximate displacements that will satisfy equation (10.5) in an approximated sense. Since the Rayleigh-Ritz formulation implicitly contains the equilibrium equations this corresponds to approximating equilibrium. This becomes clear when demanding stationarity of equation (10.8). This is shown at the end of this section.

Discretisation of an Elastic Body

Approximation of the displacement field for the entire elastic body can be difficult for complex structures. This raises the demand of discretisation of a continuum into a finite number of elements. Such a discritisation is illustrated in figure 10.1. The elements geometry are defined by nodes.

Approximation for the displacement field of a single element is within more reasonable limits but still compatibility within the body has to be fulfilled and thus compatibility between elements needs to be ensured. What is done in displacement based FE analysis is interpolation between nodal value displacements. That is displacements in a single element are found by interpolation functions as

$$\vec{u} = \bar{\bar{N}}\vec{d} = \bar{\bar{N}}\,[u_1\ v_1\ w_1,\ u_2\ v_2\ w_2,\ ....u_n\ v_n\ w_n]^T \tag{10.9}$$

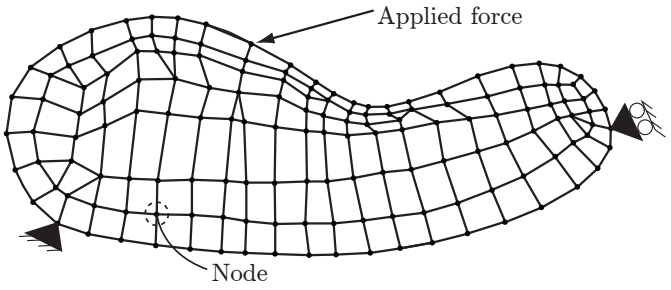

Figure 10.1: *A continuum divided into finite elements defined by nodes.*

where: $\vec{u}$ The displacements sought.

$\bar{\bar{N}}$ Interpolation functions.

n Number of nodes in the element.

The strain vector of a single element can by the definition from the theory of elasticity be written as

$$\vec{\epsilon} = \bar{\bar{\partial}}\vec{u} = \bar{\bar{\partial}}\bar{\bar{N}}\vec{d} = \bar{\bar{B}}\vec{d} \tag{10.10}$$

where: $\bar{\bar{B}}$ The strain-displacement matrix.

$\bar{\bar{\partial}}$ Matrix containing partial derivative operator.

The strain-displacement matrix $\bar{\bar{B}}$ contains the partial derivatives of the interpolation functions $\bar{\bar{N}}$. The symmetric stiffness matrix for a single element is given by

$$\bar{\bar{k}} = \int_{V_e} \bar{\bar{B}}^T \bar{\bar{E}} \bar{\bar{B}} dV \tag{10.11}$$

where: $\bar{\bar{k}}$ The stiffness matrix of the element.

$\bar{\bar{E}}$ The constitutive matrix.

From equation (10.10) it is seen that the stiffness matrix $\bar{\bar{k}}$ has the units $\frac{N}{m}$ as expected.

Setting Up The Algebraic Equations Approximating The Entire Body

As expressions for displacements, strains, and stiffness matrix for a single element are available, the algebraic set of equations describing the discretised elastic body can be derived. The total potential energy of the discretised elastic body can in accordance to equation (10.8) be written as stated in Robert D. Cook, David S. Malkus, Michael E. Plesha, and Robert J. Witt [16, p. 159]

$$\Pi_p = \sum_{i=1}^{N_{els}} \int_V \frac{1}{2} \vec{\epsilon}^T \bar{\bar{E}} \vec{\epsilon} dV - \sum_{i=1}^{N_{els}} \int_V \vec{u}^T \vec{F} dV - \sum_{i=1}^{N_{els}} \int_S \vec{u}^T \vec{\Phi} dS - \vec{D}^T \vec{P} \tag{10.12}$$

The integration span every single element and are summarised to give the total potential energy. By substitution of equations (10.9), (10.10), and (10.11) into (10.12) and introducing the force vector $\vec{r}_{ei}$ the total potential energy can be expressed as

$$\Pi_p = \frac{1}{2} \sum_{i=1}^{N_{els}} \vec{d}_i^T \bar{\bar{k}}_i \vec{d}_i - \sum_{i=1}^{N_{els}} \vec{d}_i^T \vec{r}_{ei} - \vec{D}^T \vec{P} \tag{10.13}$$

where: i Subscript denoting element i.

$\vec{r}_{ei}$ The force vector containing body forces and surface tractions.

In the absence of initial stresses and strains which are omitted in this derivation $\vec{r}_{ei}$ is given by

$$\vec{r}_{ei} = \int \bar{\bar{N}}^T \vec{F} dV + \int \bar{\bar{N}}^T \vec{\Phi} dS \tag{10.14}$$

Each element d.o.f. $\vec{d}_i$ is related to the global d.o.f. $\vec{D}$ by the transformation matrix $\bar{\bar{L}}_i$ consisting of only ones and zeroes.

$$\vec{d}_i = \bar{\bar{L}}_i \vec{D} \tag{10.15}$$

Substituting this relation into equation (10.13) gives the total potential energy expressed in global d.o.f.

$$\Pi_p = \frac{1}{2}\vec{D}^T \left(\sum_{i=1}^{N_{els}} \bar{\bar{L}}_i^T \bar{\bar{k}}_i \bar{\bar{L}}_i \right) \vec{D} - \vec{D}^T \sum_{i=1}^{N_{els}} \bar{\bar{L}}_i^T \vec{r}_{ei} - \vec{D}^T \vec{P} \tag{10.16}$$

$$= \frac{1}{2}\vec{D}^T \bar{\bar{K}} \vec{D} - \vec{D}^T \vec{R} \tag{10.17}$$

where: $\bar{\bar{K}}$ Global stiffness matrix.

$\vec{R}$ The global force vector containing applied loads $\vec{P}$ and element load vectors $\vec{r}_{ei}$.

Now recalling that the objective of the Rayleigh-Ritz method in structural mechanics is to demand stationarity of the function Π_p and this is achieved by partial differentiation with respect to displacements. If the algebraic equations in (10.13) are written in expanded form, it becomes clear that the elements of $\{D\}^T$ vanish upon differentiation.

$$\frac{\partial \Pi_p}{\partial D_i} = 0 \qquad \Rightarrow \tag{10.18}$$

$$\bar{\bar{K}}\vec{D} - \vec{R} = 0 \qquad \Rightarrow \tag{10.19}$$

$$\bar{\bar{K}}\vec{D} = \vec{R} \tag{10.20}$$

Demanding stationarity of the total potential energy gives the equilibrium equation of internal and external forces. This corresponds to the idea of variational methods, from which the Rayleigh-Ritz method originates, where the equilibrium equation is implicitly contained in the functional. The equilibrium equation for a problem formulated as a functional is obtained when the function, which yields stationarity of the functional, is put into the Euler-Lagrange equation of (10.2). In the Rayleigh-Ritz method the equilibrium equation is obtained from equation (10.18) or in general (10.5). This is a key difference between the approximate Rayleigh-Ritz approach and the analytical approach of calculus of variations using functionals.

Equations (10.9) through (10.20) provide the hands on algebraic equations which can be used to perform structural analysis of an elastic body. The main problem that is sought solved is the equilibrium equation (10.20) and equation (10.9) through (10.11) provide expressions that make the displacement based solution possible.

10.3 The Bilinear Rectangular Element (Q4)

The bilinear Q4 element is illustrated in figure10.2. It has four nodes, where each can move in the $x-$ and y-directions. The entire element thus has eight degrees of freedom. The associated displacement field is expressed by a set of complete first order functions cf. Cook, Malkus, Plesha, and Witt [16, p.97]

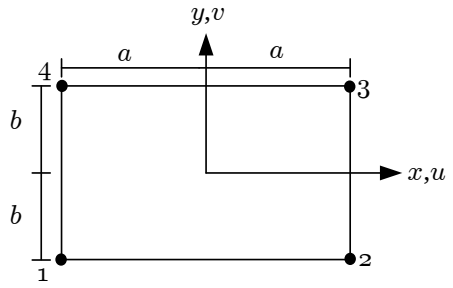

Figure 10.2: *Q4 Element with dimensions.*

$$u(x,y) = a_1 + a_2\,x + a_3\,y + a_4\,x\,y \tag{10.21}$$

$$v(x,y) = a_5 + a_6\,x + a_7\,y + a_8\,x\,y \tag{10.22}$$

where: $u(x,y)$ Displacement function in the x-direction.

$v(x,y)$ Displacement function in the y-direction.

a_i The generalised d.o.f. or generalised coordinates.

The displacement functions for the element can be formulated using matrix notation:

$$\vec{\Phi} = X\bar{Y}\,\vec{a} \tag{10.23}$$

$$\begin{bmatrix} u(x,y) \\ v(x,y) \end{bmatrix} = \begin{bmatrix} 1 & x & y & xy & 0 & 0 & 0 & 0 \\ 0 & 0 & 0 & 0 & 1 & x & y & xy \end{bmatrix} \begin{bmatrix} a_1 \\ a_2 \\ a_3 \\ a_4 \\ a_5 \\ a_6 \\ a_7 \\ a_8 \end{bmatrix} \tag{10.24}$$

The constants a_i are problem related, due the difference in shape and size of each element in a model. It is thus favorable to formulate the displacement functions in a more general way. This can be done by introducing a set of interpolation functions between each node in the element. Formulating a relation between the constants a_i and the nodal displacements can be accomplished by using the A-Matrix method, and thus making it possible to determine a set of functions which can interpolate values between each node cf. Cook, Malkus, Plesha, and Witt [16, p.84].

$$\vec{\Phi}_e = \bar{\bar{A}}\vec{a} \tag{10.25}$$

where: $\vec{\Phi}_e$ Nodal displacement vector.

$\bar{\bar{A}}$ Matrix containing nodal coordinates.

The $\bar{\bar{A}}$ matrix is formulated using the displacement variables from (10.24), so the interpolation is of the same order as the displacement functions. The coordinates for each node in the element are substituted in to the functions, thus ensuring unity at each individual node. Using the coordinates from figure 10.2 gives the following description.

$$\vec{\Phi}_e = \begin{bmatrix} u_1 \\ v_1 \\ u_2 \\ v_2 \\ u_3 \\ v_3 \\ u_4 \\ v_4 \end{bmatrix} = \begin{bmatrix} 1 & -a & -b & ab & 0 & 0 & 0 & 0 \\ 0 & 0 & 0 & 0 & 1 & -a & -b & ab \\ 1 & a & -b & -ab & 0 & 0 & 0 & 0 \\ 0 & 0 & 0 & 0 & 1 & a & -b & -ab \\ 1 & a & b & ab & 0 & 0 & 0 & 0 \\ 0 & 0 & 0 & 0 & 1 & a & b & ab \\ 1 & -a & b & -ab & 0 & 0 & 0 & 0 \\ 0 & 0 & 0 & 0 & 1 & -a & b & -ab \end{bmatrix} \begin{bmatrix} a_1 \\ a_2 \\ a_3 \\ a_4 \\ a_5 \\ a_6 \\ a_7 \\ a_8 \end{bmatrix} \tag{10.26}$$

Solving for the unknown constants a_i in expression (10.26) and substituting into equation (10.24) gives the following:

$$\vec{\Phi} = \bar{\bar{X}}\bar{\bar{Y}}\bar{\bar{A}}^{-1}\vec{\Phi}_e \tag{10.27}$$

$$= \bar{\bar{N}}\vec{\Phi}_e = \begin{bmatrix} N_1 & 0 & N_2 & 0 & N_3 & 0 & N_4 & 0 \\ 0 & N_1 & 0 & N_2 & 0 & N_3 & 0 & N_4 \end{bmatrix} \vec{\Phi}_e \tag{10.28}$$

where: $\bar{\bar{N}}$ Matrix containing shape functions.

In explicit form the shape functions for the bilinear Q4 element are describes as:

$$N_1 = \frac{(a-x)(b-y)}{4ab} \qquad N_2 = \frac{(a+x)(b-y)}{4ab}$$
$$N_3 = \frac{(a+x)(b+y)}{4ab} \qquad N_4 = \frac{(a-x)(b+y)}{4ab} \tag{10.29}$$

The following general characteristics can be formulated for the shape functions [16, p.86]

- All shape functions are of the same order as the functions they are formulated from.
- Shape function N_i equates to one when $x = x_i$, and zero when $x = x_j$.
- Shape functions of order C^0 sum to unity $\sum N_i = 1$

10.3.1 Shape Defect

Figure 10.3 shows a Q4 element in its original and deformed shape. In the original configuration the face between node 1 and node 2 is tilted, where the remaining are parallel with the coordinate axes.
In the deformed shape node 1 experiences a displacement in the x-direction, while the remaining nodes are located in their original position. The displacement results in the values between node 1 and node 4 being interpolated parabolically. The parallel faces are untouched and thus interpolated linear between the nodes which is why the element is called bilinear. The tilted face is, however, interpolated parabolically between the nodes 2 and 3 due to the displacement of node 1. This tendency is considered to be a defect of the bilinear element. Figure 10.4 shows a series of interconnected bilinear Q4 elements in their original and deformed shape.
The node marked with a $*$ has experienced a displacement in the x-direction, that has resulted in gaps between the elements. This discontinuity violates the FEA formulation, which states

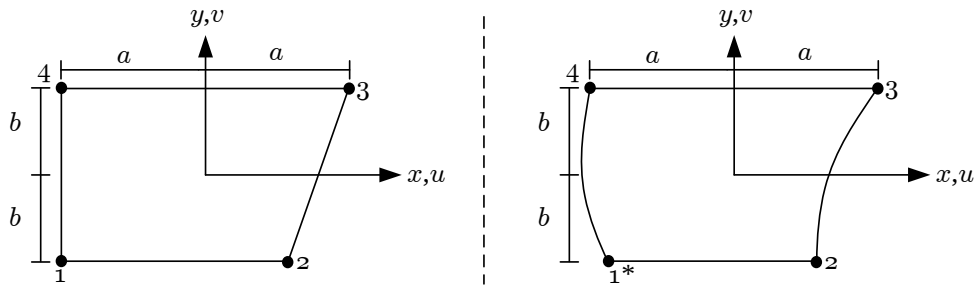

Figure 10.3: *Q4 Element with originally tilted face 2-3, where node 1 has been displaced in the x-direction*

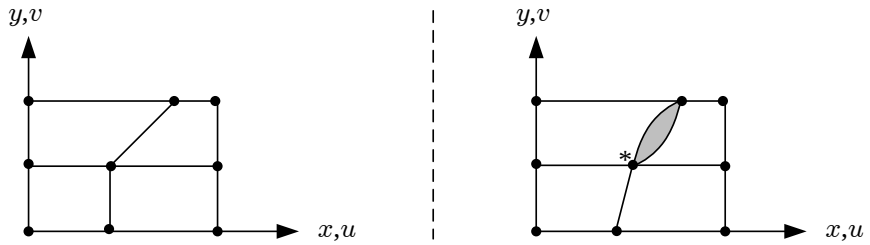

Figure 10.4: *Interconnected bilinear Q4 elements, shown in original and deformed shapes. Gaps in deformed shape marked with gray*

that elements must be compatible between each other. The defect has a softening effect on the model, which results in the model displaying larger displacement. However, since the Q4 element can be considered being a stiff element, the incompatibility between elements can result in more accurate displacements. Because defect has it origin in the method used to describe the element, is not restricted to bilinear Q4 elements alone, but also effect elements capable of replicating higher order displacement fields. Because of this the isoparametric method has been developed for formulating elements. Using the isoparametric method ensures that elements are compatible with each other. In section 10.4, the Q4 element is formulated using the isoparametric method.

10.3.2 Shear Locking

Another defect related to the Q4 element in general is shear locking, which is a phenomenon that occurs when the element is subjected to bending. Comparing a block of isentropic material subjected to pure bending with an element equivalent model where the moments have been replaced by two force couples. Figure 10.5 illustrates the situation.

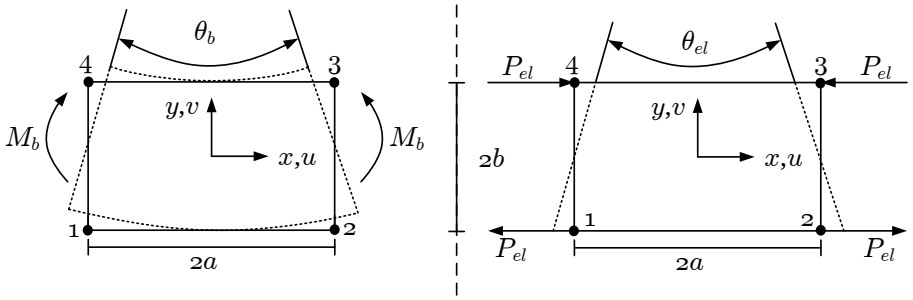

Figure 10.5: *Block of material in pure bending and Q4 element loaded as in pure bending. Deformed shapes indicated with dashed lines*

The strains in the material block are described by the following relations Cook, Malkus, Plesha, and Witt [16, p.99]:

$$\varepsilon_x = -\frac{\theta_b\, y}{2\,a} \qquad \varepsilon_y = \nu\,\frac{\theta_b\, y}{2\,a} \qquad \gamma_{xy} = 0 \tag{10.30}$$

The strains in the element model are described by the strain displacement matrix and the displacement vector:

$$\vec{\varepsilon} = \bar{\bar{B}}\vec{d} \tag{10.31}$$

Assuming that the angle θ_{el} is small, the displacement vector is described as:

$$\vec{d} = \begin{bmatrix} -\frac{b\theta_{el}}{2} & 0 & \frac{b\theta_{el}}{2} & 0 & -\frac{b\theta_{el}}{2} & 0 & \frac{b\theta_{el}}{2} & 0 \end{bmatrix}^T \tag{10.32}$$

By using the shape functions from (10.29), the strain-displacement matrix is defined as:

$$\bar{\bar{B}} = \bar{\bar{\partial}}\bar{\bar{N}} = \begin{bmatrix} \frac{\partial}{\partial x} & 0 \\ 0 & \frac{\partial}{\partial y} \\ \frac{\partial}{\partial x} & \frac{\partial}{\partial y} \end{bmatrix} \bar{\bar{N}} = \begin{bmatrix} \frac{\partial N_1}{\partial x} & 0 & \frac{\partial N_2}{\partial x} & 0 & \frac{\partial N_3}{\partial y} & 0 & \frac{\partial N_4}{\partial y} & 0 \\ 0 & \frac{\partial N_1}{\partial y} & 0 & \frac{\partial N_2}{\partial y} & 0 & \frac{\partial N_3}{\partial y} & 0 & \frac{\partial N_4}{\partial y} \\ \frac{\partial N_1}{\partial y} & \frac{\partial N_1}{\partial x} & \frac{\partial N_2}{\partial y} & \frac{\partial N_2}{\partial x} & \frac{\partial N_3}{\partial y} & \frac{\partial N_3}{\partial x} & \frac{\partial N_4}{\partial y} & \frac{\partial N_4}{\partial x} \end{bmatrix} \tag{10.33}$$

$$= \frac{1}{4ab}\begin{bmatrix} -(b-y) & 0 & (b-y) & 0 & (b+y) & 0 & -(b+y) & 0 \\ 0 & -(a-x) & 0 & -(a+x) & 0 & (a+x) & 0 & (a-x) \\ -(a-x) & -(b-y) & -(a+x) & (b-y) & (a+x) & (b+y) & (a-x) & -(b+y) \end{bmatrix} \tag{10.34}$$

Thus the strains can be evaluated for the element:

$$\vec{\varepsilon} = \begin{bmatrix} \varepsilon_x \\ \varepsilon_y \\ \gamma_{xy} \end{bmatrix} = \bar{\bar{B}}\vec{d} = \begin{bmatrix} -\frac{\theta_{el}\, y}{2a} \\ 0 \\ -\frac{\theta_{el}\, x}{2a} \end{bmatrix} \tag{10.35}$$

As can be seen by comparing expressions (10.30) and (10.35), the element displays the correct value for the normal strains ε_x and the ε_y strains are incorrect. However, the shear strains should not exist, but they vary linear along the x-axis of the element as seen in (10.35). The shear strains only display the correct value at the elements center. The shear strain absorbs strain energy from the element, which makes it more stiff and thus reducing the displacement of the element. By equating the work done by the moment and coupled forces, it can be shown that the effect of shear locking increases at the ratio $\frac{a}{b}$ increases, see Cook, Malkus, Plesha, and Witt [16, p.99]. The shear locking defect can, however, be compensated for by the use of reduced integration which is described in section 10.6.

10.4 Isoparametric Formulation of Q4

The bilinear Q4 element described in section 10.3 does only display compatibility between elements when the elements are rectangular. When dividing a continuum into elements, it is often not possible to do so only with rectangular elements. Thus another formulation is needed which enables the use of non rectangular elements when dividing the structure. This can be accomplished by the use of the isoparametric formulation method. Here an auxiliary, or natural coordinate system (ξ,η) is introduced onto the element. The coordinate axes from the (ξ,η) system bisects the mid points of the element sides, thus the coordinate axes do not necessarily intersect each other at right angles nor in the element centroid. The element is then mapped in (ξ,η) such that it forms a rectangle. This is illustrated in figure 10.6.

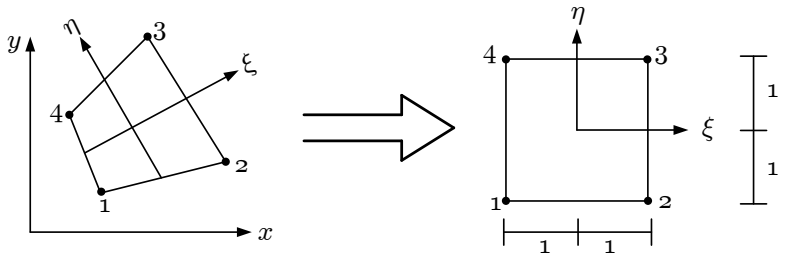

Figure 10.6: *Non rectangular element in Cartesian coordinate system* (x, y)*, mapped onto auxiliary coordinate system* (ξ, η).

Performing the interpolation between the nodes in the auxiliary coordinate system, ensures that the element sides are interpolated linearly, and thus makes it compatible with neighbouring elements. The shape functions for the Q4 element described in section 10.3, can be reformulated to fit the auxiliary reference system. This is done by replacing the lengths a, b with the unit lengths from the auxiliary system, and replacing variables x, y with ξ and η, respectively. The shape functions for the isoparametric element thus become:

$$N_1 = \frac{1}{4}(1-\xi)(1-\eta) \qquad N_2 = \frac{1}{4}(1+\xi)(1-\eta)$$
$$N_3 = \frac{1}{4}(1+\xi)(1+\eta) \qquad N_4 = \frac{1}{4}(1-\xi)(1+\eta) \tag{10.36}$$

Use of the isoparametric formulation ensures compatibility between elements, however, the Q4 element is still sensitive to shear locking. The formulation is also associated with coordinate transformation between the two coordinate systems, when calculating the stiffness matrix $\bar{\bar{k}}$ for each element in a model. The calculation of the stiffness matrix for the isoparametric Q4 element is described in the following.

10.4.1 The Element Stiffness Matrix

The stiffness matrix for the general bilinear rectangular Q4 element, is calculated using the following expression, see Cook, Malkus, Plesha, and Witt [16, p.208]:

$$\bar{\bar{k}} = \int\int \bar{\bar{B}}^T \bar{\bar{E}} \bar{\bar{B}} t \, dx \, dy \tag{10.37}$$

where:

	$\bar{\bar{k}}$	Element stiffness matrix.
	$\bar{\bar{B}}$	Strain-displacement matrix.
	$\bar{\bar{E}}$	Constitutive matrix.
	t	Element thickness.

However, when using the isoparametric formulation the shape functions in $\bar{\bar{N}}$ are not explicit functions of x, y but of ξ, η. Thus the differentiation of $\bar{\bar{N}}$ can not be performed directly with regards to x, y. It is though possible to relate the x, y coordinates to ξ, η through the correlation

shown below, see Mouritsen [18]:

$$x = \sum_{i=1}^{4} N_i x_i = N_1 x_1 + N_2 x_2 + N_3 x_3 + N_4 x_4 \tag{10.38}$$

$$y = \sum_{i=1}^{4} N_i y_i = N_1 y_1 + N_2 y_2 + N_3 y_3 + N_4 y_4 \tag{10.39}$$

where: x_i x-coordinate for node i.

y_i y-coordinate for node i.

Thus the shape functions are implicit functions of x, y, which can be shown as:

$$N_i(\xi,\eta) = N_i\left((x(\xi,\eta)),(y(\xi,\eta))\right) \tag{10.40}$$

Hence differentiating the shape functions with regards to ξ,η and applying the chain rule leads to:

$$\frac{\partial N_i}{\partial \xi} = \frac{\partial N_i}{\partial x}\frac{\partial x}{\partial \xi} + \frac{\partial N_i}{\partial y}\frac{\partial y}{\partial \xi} \tag{10.41}$$

$$\frac{\partial N_i}{\partial \eta} = \frac{\partial N_i}{\partial x}\frac{\partial x}{\partial \eta} + \frac{\partial N_i}{\partial y}\frac{\partial y}{\partial \eta} \tag{10.42}$$

Which can be reformulated as:

$$\begin{bmatrix} \frac{\partial N_i}{\partial \xi} \\ \frac{\partial N_i}{\partial \eta} \end{bmatrix} = \begin{bmatrix} \frac{\partial x}{\partial \xi} & \frac{\partial y}{\partial \xi} \\ \frac{\partial x}{\partial \eta} & \frac{\partial y}{\partial \eta} \end{bmatrix} \begin{bmatrix} \frac{\partial N_i}{\partial x} \\ \frac{\partial N_i}{\partial y} \end{bmatrix} \tag{10.43}$$

$$= \bar{\bar{J}} \begin{bmatrix} \frac{\partial N_i}{\partial x} \\ \frac{\partial N_i}{\partial y} \end{bmatrix} \tag{10.44}$$

where: $\bar{\bar{J}}$ Jacobian matrix.

For the isoparametric Q4 element, the Jacobian is defined as:

$$\bar{\bar{J}} = \frac{1}{4}\begin{bmatrix} -(1-\eta) & (1-\eta) & (1+\eta) & -(1+\eta) \\ -(1-\xi) & -(1+\xi) & (1+\xi) & (1-\xi) \end{bmatrix} \begin{bmatrix} x_1 & y_1 \\ x_2 & y_2 \\ x_3 & y_3 \\ x_4 & y_4 \end{bmatrix} = \begin{bmatrix} J_{11} & J_{12} \\ J_{21} & J_{22} \end{bmatrix} \tag{10.45}$$

It is thus possible to formulate the partial derivatives of $\bar{\bar{N}}$ with respect to x, y, by inverting the Jacobian matrix in expression (10.45).

$$\begin{bmatrix} \frac{\partial N_i}{\partial x} \\ \frac{\partial N_i}{\partial y} \end{bmatrix} = \bar{\bar{J}}^{-1} \begin{bmatrix} \frac{\partial N_i}{\partial \xi} \\ \frac{\partial N_i}{\partial \eta} \end{bmatrix} = \frac{1}{|J|} \begin{bmatrix} J_{22}\frac{\partial N_i}{\partial \xi} - J_{12}\frac{\partial N_i}{\partial \eta} \\ -J_{21}\frac{\partial N_i}{\partial \xi} + J_{11}\frac{\partial N_i}{\partial \eta} \end{bmatrix} \tag{10.46}$$

where: $|J|$ Determinant of the Jacobian matrix.

The strain-displacement matrix can thus be formulated by substituting the above values for the partial derivatives into expression (10.33), which completes the coordinate transformation. Consequently the element stiffness matrix in expression (10.37) can be calculated. The

integrals now contain functions of ξ and η due to the presence of the Jacobian matrix and its determinant, which further complicates solving the integrals. It is thus favourable to solve the integrals in the natural coordinate system, where the element geometry is likewise more simple. The integrals can be reformulated as follows [16, p.208]:

$$\bar{\bar{k}} = \int\int \bar{\bar{B}}^T \bar{\bar{E}} \bar{\bar{B}} t \, dx \, dy = \int_{-1}^{1}\int_{-1}^{1} \bar{\bar{B}}^T \bar{\bar{E}} \bar{\bar{B}} |J| \, t \, d\xi \, d\eta \tag{10.47}$$

Because the above expression contains functions of ξ and η in both the numerator and denominator, the integrals can seldom be solved analytically. Thus numerical integration is often utilised for solving the problem. The use of Gauss quadrature is explained in section 10.5. The accuracy of the coordinate transformation from the Cartesian- to the natural coordinate system depends on the element geometry. If the element is distorted in proportion to the square element in the natural coordinate system, the accuracy declines. The problem is related to the Jacobian determinant, which for planar elements acts as scalar ratio between the area of the element from x, y to ξ, η coordinates, Mouritsen [18].

10.5 Gauss Quadrature

Evaluating the integrals in expression (10.47) is done numerically due the complexity of expression. The integration can be done using several numerical methods, such as the trapezoidal rule or Simpsons's rule etc. These methods can provide good accurate results, but they are all time consuming compared to other quadrature methods. In finite elements the Gaussian quadrature is often used due to the combination of its simplicity, accuracy and speed. When integrating a function using Gauss quadrature, specific points are evaluated and the results are afterwards multiplied with associated weight factors. The location of the points and size of the weights depend on the order of the function, which can be see in table 10.2. The principal is likewise illustrated for a one dimensional problem in figure 10.7.

Gauss order: n	Degree of precision	Sampling point location(s)	Weight factor(s):W
1	1	0.0	2.0
2	3	$\pm 1/\sqrt{3}$	1.0
3	5	$\pm\sqrt{0.6}$ ‖0.0	5/9‖8/9

Table 10.2: *Location of sampling point(s) and associated weight factor(s) for Gauss quadrature in the interval $\xi = -1$ to $\xi = 1$.*

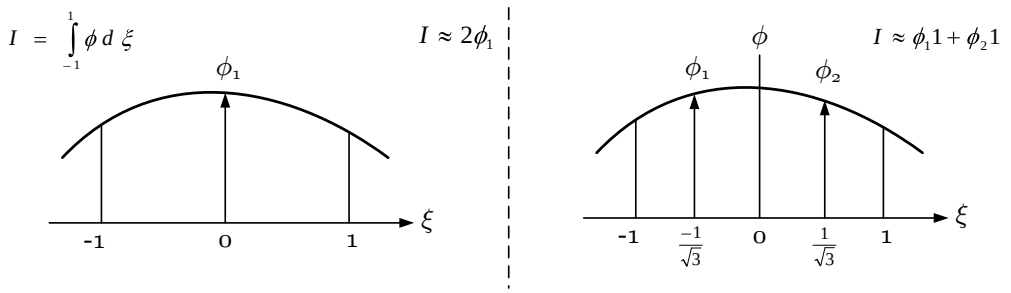

Figure 10.7: *Function ϕ integrated using first- and second order Gauss quadrature.*

In the case of the Q4 element, the integral in expression (10.47) is two dimensional, which

requires the use of the Gaussian product rule, which is shown in the following:

$$\int_{-1}^{1}\int_{-1}^{1}\phi(\xi,\eta)\,d\xi d\eta \approx \sum_i\sum_j W_i W_j \phi(\xi_i,\eta_j) \tag{10.48}$$

Because the integral expression for the Q4 element contains squares of ξ and η, a Gauss order of $n = 2$ must be used to obtain the exact integral value. This is also known as full integration. When selecting a Gauss order lower than the required order to obtain the exact integral, a reduced integration is performed. If the element is non-rectangular, a full integration Gauss order does not yield the exact integral value, due to the Jacobian determinant not being a constant value, which make expression (10.47) contain ratios of polynomials of ξ and η. It is thus important to ensure that the elements are as rectangular as possible. However, since the Q4 element is considered being a stiff element, and that the FEM formulation it self being a conservative approximation, the inaccuracy associated with the numerical integration typically softens the model. This phenomenon is utilised with reduced integration. The problems associated with reduced integration are discussed in section 10.6.

10.6 Reduced Integration

When using elements with geometries as rectangles or parallelograms, numerical integration of the element stiffness matrix can provide exact results. Using full integration non-distorted elements are integrated exactly and no zero energy modes are introduced. But the elements becomes too stiff since the displacement field is an conservative approximation. In the case of the Q4 element, the model is even stiffer, due to the element not being able to represent curved faces. To soften the element reduced integration can be used which also reduces the computational time. Reduced integration is defined as a gauss order lower than the full integration order. As an example a four node element only uses one Gauss point instead of four when applying reduced integration.
However when using reduced integration zero energy modes are introduced. A four node element has eight independent displacement modes as shown in figure 10.8.

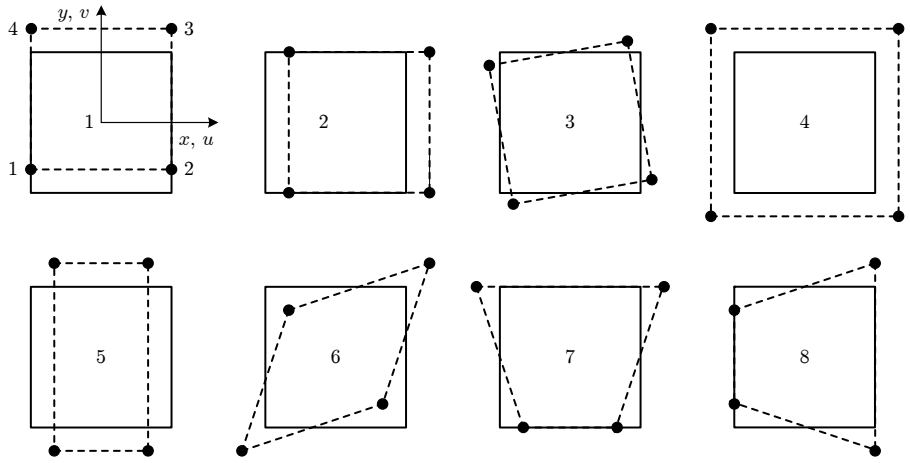

Figure 10.8: *Independent displacement modes of a four node element.*

Mode 1-3 are rigid body modes which exhibit no strain energy regardless of the number off Gauss points. Modes 4-6 are constant strain modes. Mode 7 and 8 are bending modes. When using reduced integration, modes 7 and 8 display no strain energy, and thus offer no resistance to the applied loads. They are thus called spurious modes, or hourglass modes due to their

geometric resemblance. Also for the four node element, these modes are communicable between elements, thus activating the modes in neighbouring elements. Compensation for these spurious modes can be achieved by the use hourglass control.

10.6.1 Hourglass Control

The following is based on Lund [19, pp.86-89]. When the stiffness matrix of a four node element is integrated by reduced integration, the spurious bending modes become a problem. To accommodate the associated problems, the stiffness matrices for mode 7 and 8 can be added to the element stiffness matrix $\bar{\bar{k}}$. Thus giving the element the ability to resist the bending modes. Reviewing figure 10.8, an arbitrary combination of the modes influence on the strains in the x-direction can be formulated as:

$$\vec{d}_x = a_2\vec{d_x}2 + a_3\vec{d_x}3 + a_4\vec{d_x}4 + a_5\vec{d_x}5 + a_6\vec{d_x}6 + a_7\vec{d_x}7 \tag{10.49}$$

$$= a_2\begin{bmatrix}1\\1\\1\\1\end{bmatrix} + a_3\begin{bmatrix}1\\1\\-1\\-1\end{bmatrix} + a_4\begin{bmatrix}-1\\1\\1\\-1\end{bmatrix} + a_5\begin{bmatrix}1\\-1\\-1\\1\end{bmatrix} + a_6\begin{bmatrix}-1\\-1\\1\\1\end{bmatrix} + a_7\begin{bmatrix}1\\-1\\1\\-1\end{bmatrix} \tag{10.50}$$

where: a_i Constant associated with mode i.

$\vec{d}_{xi}$ Displacement vector for mode i.

By the following it can be seen that mode seven is orthogonal to the other modes displacement in the x-direction

$$\vec{d}_{x7}^{\,T}\vec{d}_{xn} = 0\,, \quad n = 2,3,4,5,6 \tag{10.51}$$

Constructing a stiffness matrix from $\vec{d}_{x7}$ and $\vec{d}_{x7}^{\,T}$ will result in a matrix which only contributes to stiffness for mode seven. The stiffness matrix for mode seven is constructed as

$$\bar{\bar{k}}_7 = a_7\vec{d}_{x7}a_7\vec{d}_{x7}^{\,T} = (a_7)^2\begin{bmatrix}1\\-1\\1\\-1\end{bmatrix}\begin{bmatrix}1 & -1 & 1 & -1\end{bmatrix} = (a_7)^2\,\bar{\bar{k}}_{7,1} \tag{10.52}$$

where: $\bar{\bar{k}}_7$ Stiffness matrix for mode seven.

$\bar{\bar{k}}_{7,1}$ Stiffness matrix for mode seven containing only ± 1.

That $\bar{\bar{k}}_7$ only contributes to stiffness for mode seven can be seen from (10.51) and is formulated as

$$\bar{\bar{k}}_7\vec{d}_{xn} = 0\,, \quad n = 2,3,4,5,6 \tag{10.53}$$

The constant a_7 can be determined so the amount of strain energy absorbed by bending mode seven is equal to the energy of a rectangular solid in pure bending. An element subject to bending mode seven and a rectangular solid in pure bending are shown in figure 10.9. The displacement in the x-direction is $\bar{u}$.
The strain energy in a rectangular solid in pure bending is given as [19, p.109]

$$U_m = \frac{1}{2}\vec{d}^{\,T}\bar{\bar{k}}\vec{d} = \frac{2}{3}E\bar{u}^2\frac{b_m}{a_m}\,t \tag{10.54}$$

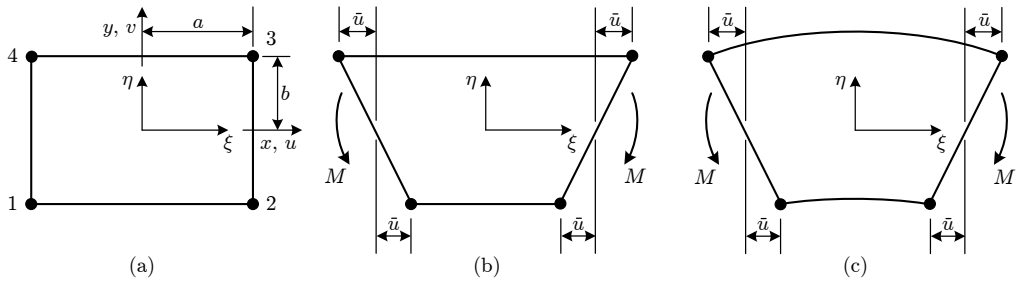

Figure 10.9: *A rectangular element subject to bending (left) and the exact mode for a rectangle in pure bending (right).*

where: a_m Half the length of a rectangular solid in global coordinates.

b_m Half the height of a rectangular solid in global coordinates.

$\bar{u}$ Displacement in the x-direction due to bending.

The strain energy which can be absorbed by the $\bar{\bar{k}}_7$ stiffness matrix is

$$U_7 = \frac{1}{2}\vec{d_u}^{\,T}\bar{\bar{k}}_7\vec{d_u} = \frac{1}{2}\bar{u}\{d_x\}_7^T(a_7)^2\bar{\bar{k}}_{7,1}\bar{u}\{d_x\}_7 \tag{10.55}$$

where: $\vec{d_u}$ The displacement vector for $\bar{u}$ in the x-direction.

In order for $\bar{\bar{k}}_7$ to be able to absorb the correct amount of energy the elastic work is set equal to the strain energy in bending.

$$U_7 = U_m \quad \Rightarrow \tag{10.56}$$

$$\frac{1}{2}\bar{u}\vec{d}_{x7}^{\,T}(a_7)^2\bar{\bar{k}}_{7,1}\bar{u}\vec{d}_{x7} = \frac{2}{3}E\bar{u}^2\frac{b_m}{a_m}t \quad \Rightarrow \tag{10.57}$$

$$\frac{1}{2}\vec{d}_{x7}^{\,T}(a_7)^2\bar{\bar{k}}_{7,1}\vec{d}_{x7} = \frac{2}{3}E\frac{b_m}{a_m}t \quad \Rightarrow \tag{10.58}$$

$$\frac{1}{2}(a_7)^2 16 = \frac{2}{3}E\frac{b_m}{a_m}t \quad \Rightarrow \tag{10.59}$$

$$(a_7)^2 = \frac{1}{12}E\frac{b_m}{a_m}t \tag{10.60}$$

Thus the value for a_7 gives $\bar{\bar{k}}_7$ the stiffness, so as the strain energy associated with bending mode 7 can be accounted for. Similar calculations can be performed for bending mode 8 where the displacements are in the y-direction and the relation $\frac{b_m}{a_m}$ becomes $\frac{a_m}{b_m}$. The idea is to give the stiffness matrix, calculated by reduced integration, stiffness towards spurious modes seven and eight. The final element stiffness matrix using reduced integration with hourglass control then becomes

$$\bar{\bar{k}} = \bar{\bar{k}}_{re} + \bar{\bar{k}}_7 + \bar{\bar{k}}_8 \tag{10.61}$$

where: $\bar{\bar{k}}_{re}$ Element stiffness matrix calculated with reduced integration.

Because the constants a_7 and a_8 are formulated using the element's global coordinates, the accuracy of their values decay if the element is non-rectangular. Thus for distorted elements, the added stiffness introduced by the hourglass stabilisation becomes a poor approximation.

When using reduced integration combined with the hourglass control method, the shear locking effect is removed from the Q4 element, while maintaining the ability to represent bending in the element.

10.6.1.1 Example Integration Methods

Based on the Finite Element Analysis the deflection for a cantilever beam can be computed. The deflection is computed with full integration, reduced integration and reduced integration with hourglass control. The deflection can be calculated analytically based on Bernoulli-Euler beam theory. The computed deflections can be compared to the analytically calculated deflection. The beam is shown in figure 10.10.

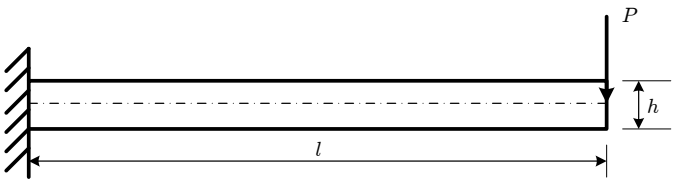

Figure 10.10: *A cantilever beam subject to a transverse load.*

The deflection calculated with Bernoulli-Euler beam theory is

$$v_{max} = \frac{PL^3}{3EI} = \frac{Pl^3}{3E\frac{bh^3}{12}} = \frac{-100\,N \cdot (600\,mm)^3}{3 \cdot 210{,}000\frac{N}{mm^2} \cdot \frac{10\,mm \cdot (50\,mm)^3}{12}} = -0.329\,mm \tag{10.62}$$

where:

	P	The force applied to the beam.
	l	The length of the beam.
	E	Modulus of elasticity.
	b	The width of the beam.
	h	The height of the beam.

The results from the finite element analysis are listed in table 10.3.

Method	Bernoulli-Euler	Q4, Full	Q4, Reduced	Q4, Reduced hourglass control
Displacement / mm	-0.329	-0.242	-0.441	-0.330
Deviation from B.E.	- -	26 %	34 %	0.3 %

Table 10.3: *Deflection of cantilever beam calculated using various methods. B.E. is short for Bernoulli-Euler.*

The full integration method makes the beam too stiff and deviates with 26 %. However, with mesh refinement the result approaches the analytic solution. The reduced integration makes the beam too soft because of the zero energy modes and deviates with 34 %. The hourglass control compensates for the zero energy mode and the displacement obtained from the reduced integration with hourglass control deviates with 0.3 %.

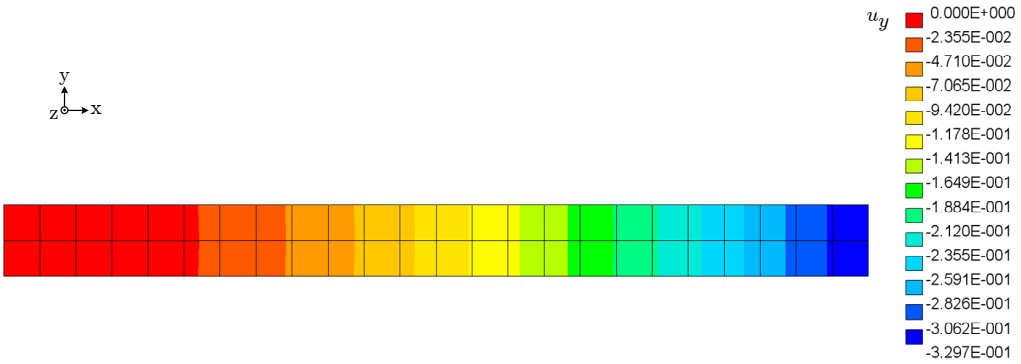

Figure 10.11: *Deflection of a beam computed with reduced integration with hourglass control.*

The deflection computed with reduced integration and hourglass control is shown in figure 10.11.

10.7 Element and Nodal Stresses

The stresses in an element can both be estimated within the element or in the nodes. In the following an approach to estimate the stresses is given. The stress vector is given by Hooke's law, assuming that the model is linear elastic. Hooke's law is given by:

$$\vec{\sigma} = \bar{\bar{E}}\vec{\varepsilon} \tag{10.63}$$

where:
- $\vec{\sigma}$ The stress vector.
- $\bar{\bar{E}}$ The constitutive matrix.
- $\vec{\varepsilon}$ The strain vector.

Given that there are no initial stresses or strains, the stresses in the FEA can by formulated as

$$\vec{\sigma} = \bar{\bar{E}}\bar{\bar{B}}\vec{d} \tag{10.64}$$

For plane stress ($\sigma_z = \tau_{yz} = \tau_{zx} = 0$) and isotropic materials the constitutive matrix is expressed as

$$\bar{\bar{E}} = \frac{E}{1-\nu^2}\begin{bmatrix} 1 & \nu & 0 \\ \nu & 1 & 0 \\ 0 & 0 & \frac{1-\nu}{2} \end{bmatrix} \tag{10.65}$$

The constitutive matrix is symmetric for isotropic materials.

When the Q4 element is bent, the element shows spurious shear stresses at the nodes as described in section 10.3.2. In the lower order Gauss points, the stresses are most accurate. These points are called super convergent, since the stresses may be most comparable to the computed displacement here. To find the stresses at the nodes the stresses calculated within the element are extrapolated. This is done by formulating a new coordinate system defined by the dimensionless coordinates r and s. The new coordinates are proportional to ξ and η so that for a second order Gauss rule they are

$$r = \sqrt{3}\xi \quad \text{and} \quad s = \sqrt{3}\eta \tag{10.66}$$

The coordinates for e.g Gauss point 3 in figure 10.12 then becomes $(1,1)$ in the rs coordinate system instead of $(\sqrt{3},\sqrt{3})$ in the $\xi\eta$ coordinate system. For reduced integration the Gauss point is $(0,0)$ which is located in the centre of the element. Stresses at an arbitrary point P in

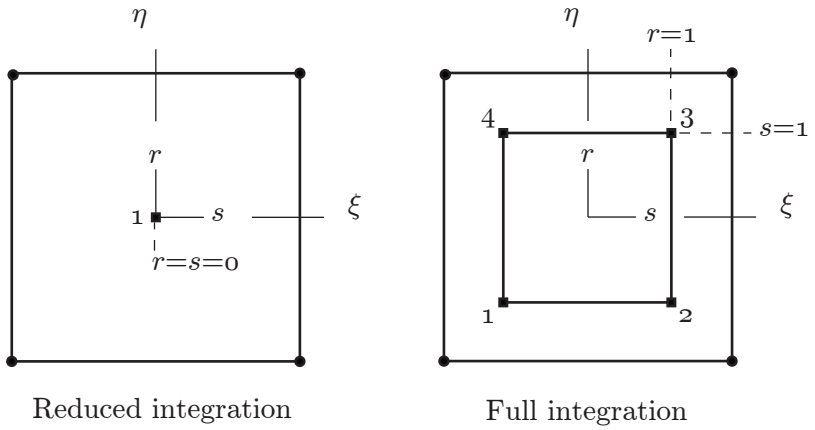

Figure 10.12: *The r s coordinate system shown on an isoparametric bilinear element with one Gauss point (left) and four Gauss points (right).*

the element is calculated by use of the shape functions N_i in the new coordinate system as

$$\sigma_P = \Sigma N_i \sigma_i \quad \text{for} \quad i = 1,2,3,4 \tag{10.67}$$

and:

$$\begin{aligned} N_1 &= \frac{1}{4}(1-r)(1-r) & N_2 &= \frac{1}{4}(1+s)(1-r) \\ N_3 &= \frac{1}{4}(1+s)(1+r) & N_4 &= \frac{1}{4}(1-s)(1+r) \end{aligned} \tag{10.68}$$

where: σ_i σ_x, σ_y or τ_{xy}.

r The ξ coordinate to the Gauss point.

s The η coordinate to the Gauss point.

From equation (10.67) it can be seen that extrapolation from a single Gauss point results in $\Sigma N_i = 1$ so the stresses in the four nodes are the same as in the single Gauss point.

Strains can be extrapolated within the element with the same approach as for stresses.

10.8 DMS7FEA

The subjects described in the preceding sections of this chapter have been incorporated into the finite element program DMS7FEA. *The program has been developed by Erik Lund at Aalborg University. The program uses model input files from e.g. ANSYS or CosmosWorks, where the mesh, load and boundary conditions have been predefined. The output from DMS7FEA is interpreted by FEPlot, which also has been developed at Aalborg University. Essential subroutines in DMS7FEA have been removed. The removed subroutines calculated the element stiffness matrix and element stresses. In the following a brief presentation of the program is given and pseudo code for the stiffness matrix calculation is shown. Afterwards the spanner element model is presented, where the mesh and boundary conditions are described. Finally results from the model*

Initialise the weight factors W_i and W_j and Gauss sampling points from the Gauss order n
Loop over number of gauss points n in the ξ direction ($i = 1$ to n) Loop over number of gauss points n in the η direction ($j = 1$ to n) Call subroutine that calculates $[B]$ and $\|J\|$ and Call subroutine that assembles $[E]$ and get element thickness t Calculate product $W_i W_j [B]^T [E][B]\|J\|t$ and add to the element stiffness matrix $[k]$ End loops
if reduced integration is enabled, and Q4 elements are used add stiffness matrices $[k]_7$ and $[k]_8$ to $[k]$

Table 10.4: *Pseudo code for computing the element stiffness matrix.*

are presented.

Figure 10.13 shows the implemented subroutines on element level. The displacements are solved on a global level, credited by Erik Lund.

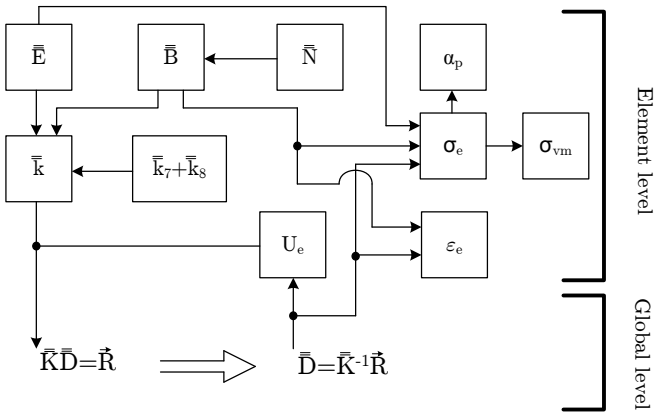

Figure 10.13: *Diagram of implemented subroutine calculations in DMS7FEA.*

The element stiffness matrix, $\bar{\bar{k}}$ is calculated using the constitutive matrix $\bar{\bar{E}}$, strain-displacement matrix $\bar{\bar{B}}$, and if hourglass stabilisation is enabled the bending mode stiffness matrices $\bar{\bar{k}}_7$ and $\bar{\bar{k}}_8$. The subroutine for the determining the stiffness matrix is illustrated in table 10.4. Each element stiffness matrix is then added to the global stiffness matrix $\bar{\bar{K}}$. When all the stiffness matrices for all the elements have been calculated, the system of equations are solved, and the displacements of element nodes are obtained. Based on the displacements, element stresses, σ_e, strains, ε_e and specific strain energy density, U_e are calculated. From the element stresses, principle angles, α_p, and the von Mises reference stresses,σ_{vm}, are determined.

10.8.1 Spanner Model Mesh

The element model of the spanner has been made in ANSYS, using planar QM6 elements where the internal d.o.f have been excluded, such that the element becomes an isoparametric Q4 el-

ement. As mentioned in section 10.4 the isoparametric Q4 element is sensitive to distortion. To ensure that the elements used in the discretisation are as rectangular as possible, the mesh has been created manually in ANSYS. The mesh is shown in figure 10.14. The red lines indicate

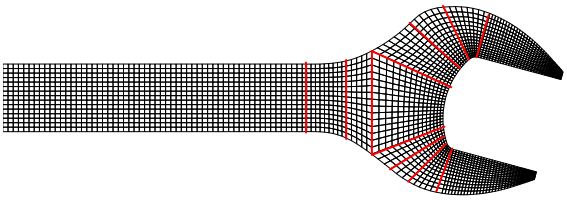

Figure 10.14: *Spanner model with element mesh.*

separation lines, used to control the number of elements along each line. Here 15 elements have been used along each of these lines in order to keep the elements as rectangular as possible. The number of elements in the shank, up to the first red line is 150 by 15. The total number of elements in the head of the spanner is 1845. As mentioned, the mesh has been made with element shape as the main objective, however, several iterations have been made with fewer elements. The deviation between results obtained from earlier revisions to the final mesh shown in figure 10.14 was negligible, thus the mesh shown in the figure has been used in the analysis. However, the number of elements in the jaws have been reduced from earlier versions. This has been done to reduce the strain energy density in elements on which the boundary conditions have been applied, so as to reduce energy peaks from the results.

10.8.2 Boundary conditions

The boundary conditions used in the estimates which have been sought replicated in the experiments are not possible to model in ANSYS if equilibrium is to be met. In order to ensure equilibrium an additional d.o.f. has to be constrained. As seen on figure 10.15 four boundary conditions defining the loads and constraints of the spanner have been modelled for the FEA.

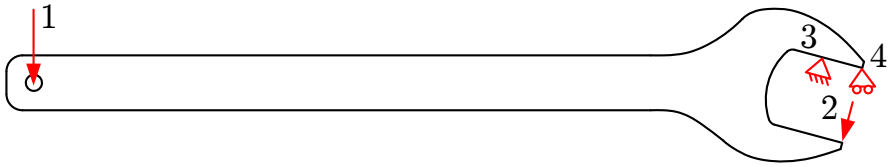

Figure 10.15: *The spanner shown with boundary conditions for the FEA.*

There are two alternations from the initial boundary conditions presented in section 6.2. The roller support on the lower jaw has been replaced by a force, which enables the jaws to move from one another. On the tip of the upper jaw a roller support has been modelled to satisfy equilibrium in ANSYS. The roller support has been moved to the tip in order to increase the moment arm and reduce the reaction force. This reduces local stress concentrations.
The boundary conditions are applied at the nodes of the elements which gives large stress concentrations in the nearest elements. The inaccurate stress distributions are local, hence they are considered to be of less importance. This is visible in the element around the third boundary condition in figure 10.17.

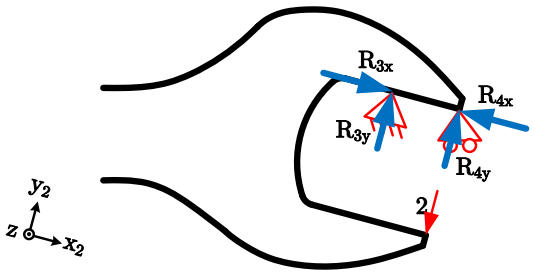

Figure 10.16: *Pin and roller support with reactions forces.*

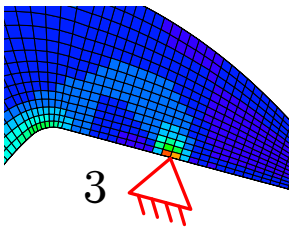

Figure 10.17: *FEA model with stress concentrations due to boundary conditions.*

10.9 Selection of Integration Method

DMS7FEA can calculate the element stiffness matrices for Q4 elements using either full integration (Q4F), reduced integration (Q4R), or reduced integration with hourglass control (Q4RH). Since three different methods of integration are present in the program it is needed to select one of these for future work. It is desired to choose the method which gives the most accurate results in a loading scenario dominated by bending. As point of reference an ANSYS model with Q8 elements is used. The results from an ANSYS Q8 model are believed to be reliable. Hence, selected results from DMS7FEA are compared to results from ANSYS in order to estimate their correctness. The spanner model is used for the comparison, where the same mesh layout has been used for the analysis using DMS7FEA and ANSYS.

In the comparison, different sampling locations have been used. The sampling locations on the spanner body correspond to the locations of the strain gauges described in section 8.4. Thus location number 1 corresponds to the location of strain gauge $SG1$ etc. The specific locations are shown in figure 8.10. Four locations have been selected for the analysis comparison. These are location 10, 8, 9, and 4. At location 4 the mesh consists of small non-distorted rectangular elements. Also the strain level at this location is in general of small magnitude compared to the other locations. Thus all the integration methods are expected to give accurate strain results with small deviations at this location.

The locations are according to the estimated calculations and strain gauge measurements dominated by bending, which the Q4 element does not represent with great accuracy. It is thus expected that the results obtained by the three different integration methods will deviate from the results calculated from ANSYS using the Q8 element. In the following the calculated strains and displacements are presented, and the results are commented. Each result is shown in micro strains and is associated with a percentage, which is the specific result's deviation from the result calculated in ANSYS.

10.9.1 Strain in the x-Direction

Table 10.5 shows the calculated ε_{11} normal strains.

Location	Q4F		Q4R		Q4RH		AnsysQ8
	ε/μ	$s(\varepsilon)$	ε/μ	$s(\varepsilon)$	ε/μ	$s(\varepsilon)$	ε/μ
10	-1162	3%	-1144	4%	-1169	2%	-1197
8	-370	11%	-370	11%	-354	15%	-417
9	-1173	0.2%	-1179	0.3%	-1178	0.2%	-1175
4	-329	7%	-332	6%	-329	7%	-353
Average deviation:		**5%**		**6%**		**6%**	

Table 10.5: *Calculated strains in the x-direction with deviation from AnsysQ8.*

The results deviate on average with about 6% from the ANSYS results, where the largest individual deviation is 15% at location 8 using Q4RH. However, the other integration methods also have their maximum deviation at this location. The large deviation at location 8 can possibly be explained by the location being in a transitional area (an area where the gradient of the stress field is quite large) where the strains begin to grow in magnitude which is shown in figure 10.18.

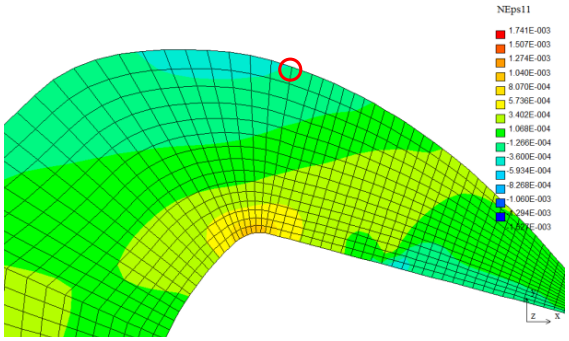

Figure 10.18: ε_{11} *obtained from DMS7FEA using Q4RH. Node value for location 8 marked with a red circle.*

At this location ANSYS interpolates the strain differently than DMS7FEA, which calculates the strains in the elements centre using one Gauss point and assigns this value to the nodes. Due to the small deviation between the different methods, their accuracy is considered similar.

10.9.2 Shear Strains

Table 10.6 shows the calculated ε_{12}, note that the strains are not represented as engineering strains but as tensor strains.
As expected the calculated shear strains are in general less accurate than the results obtained from ANSYS, with average deviations between 8 – 13%. However, the results calculated in the shank at location 4 nearly represent the correct value of zero strains. The deviation between Q4F and Q4RH is considered negligible, whereas the Q4R method in general shows larger deviations.

10.9.3 Strain in the y-Direction

Table 10.7 shows the calculated ε_{22}.

Location	Q4F		Q4R		Q4RH		AnsysQ8
	ε/μ	$s(\varepsilon)$	ε/μ	$s(\varepsilon)$	ε/μ	$s(\varepsilon)$	ε/μ
10	257	19%	255	19%	249	21%	316
8	178	4%	215	16%	172	7%	185
9	49	2%	51	2%	49	3%	50
4	1.2		0.6		1.2		0.1
Average deviation:		**8%**		**13%**		**10%**	

Table 10.6: *Calculated shear strains with deviation from AnsysQ8. Note that the percentage deviation has been removed from location 4 due to the magnitudes.*

Location	Q4F		Q4R		Q4RH		AnsysQ8
	ε/μ	$s(\varepsilon)$	ε/μ	$s(\varepsilon)$	ε/μ	$s(\varepsilon)$	ε/μ
10	318	10%	306	6%	304	5%	289
8	70	2%	97	36%	65	9%	72
9	361	1%	359	1%	362	0.3%	363
4	92	7%	96	3%	92	7%	99
Average deviation:		**5%**		**12%**		**5%**	

Table 10.7: *Calculated strains in the y-direction with deviation from AnsysQ8.*

As seen from the results, the Q4R integration method yields an average deviation twice as large compared to the other integration methods. The deviation between Q4F and Q4RH is again considered as negligible, and both methods yield accurate results.

10.9.4 Displacement in the x-Direction

Table 10.8 shows the calculated displacements in the x-direction.

Location	Q4F		Q4R	Q4RH		AnsysQ8
	ε/μ	$s(\varepsilon)$	ε/μ	ε/μ	$s(\varepsilon)$	ε/μ
10	-0.0889	9%	-71945	-0.0801	2%	-0.0814
8	-0.0121	18%	0.2623	-0.0150	2%	-0.0147
9	-0.0908	5%	-71945	-0.0822	5%	-0.0864
4	-0.0263	9%	0.0408	-0.0216	10%	-0.0241
Average deviation:		**10%**			**5%**	

Table 10.8: *Calculated displacement in the x-direction with deviation from AnsysQ8.*

As seen from the results, the displacements calculated using only reduced integration reach values more than 250 times larger than the length of the entire spanner. This phenomenon occurs as a result of the spurious modes 7 and 8 associated with reduced integration. As explained in section 10.6, these modes are communicable between elements, thus elements subjected to a spurious mode triggers the effect in neighbouring elements. Because the spanner is dominated by bending, the effect is magnified due to the elements not being able to resist bending. However, as seen from the results in the above tables, the calculated strains are within a reasonable limit of accuracy. This is because the Gauss point used for calculating the strains is placed in the elements centre and thereby does not register the spurious effects [16, p.225]. The results obtained by Q4RH clearly show the effect of the hourglass control. The added stiffness

which resist the spurious bending modes, results in the method displaying the most accurate displacements.

10.9.5 Displacement in the y-Direction

Table 10.9 shows the calculated displacements in the y-direction.

Location	**Q4F**		**Q4R**	**Q4RH**		**AnsysQ8**
	ε/μ	$s(\varepsilon)$	ε/μ	ε/μ	$s(\varepsilon)$	ε/μ
10	-0.0369	4%	-268490	-0.0415	17%	-0.0354
8	-0.0132	15%	0.1704	-0.0153	2%	-0.0155
9	-0.0571	6%	-268490	-0.0607	0%	-0.0608
4	0.0272	74%	0.6424	0.0104	33%	0.0156
Average deviation:		**25%**			**13%**	

Table 10.9: *Calculated displacement in the y-direction with deviation from AnsysQ8.*

Again the effect of the spurious bending modes associated with the reduced integration is clear. As with the results from the displacement in the x-direction, the results obtained with hourglass control show twice the accuracy compared to full integration.

10.9.6 Closure

Throughout the above, the three different types of element stiffness integration have been evaluated. Results show that strains calculated using Q4F and Q4RH both deviate from the ANSYS model with an average of 6%, whereas the Q4R method deviates with an average of 9%. It can thus not be clarified on the basis of the calculated strain, if fully integrated elements give more accurate results than elements integrated using reduced integration with hourglass control. However, the calculated displacements show that Q4RH elements were twice as accurate as elements with full integration. In chapter 3 the requirements for the optimised spanner are listed. These requirements are based on degree of deformation, thus displacement accuracy is essential for the element model. On this basis reduced integration with hourglass control is selected as the integration method used for the result comparison and optimisation.

10.10 Results of DMS7FEA

DMS7FEA produces a variety of results for stress- and deformation analysis of the spanner. A few of these were presented in the preceding section. However, one of the advantages of FEA over other methods is that it also gives a complete description of strains and stresses in the entire model. In this section a small selection of plots of larger sections of the spanner are presented in order to give a glimpse on the holistic understanding of the load state which the FEA provides.
Strains and displacements from DMS7FEA have been used in sections 10.9 and 11.1 for comparison purposes. To represent the stresses determined, the principal stresses and the von Mises stresses are shown in figure 10.19 and 10.20, respectively. In order to make interesting areas more visible only a magnification of the spanner-head is shown instead of the entire model.

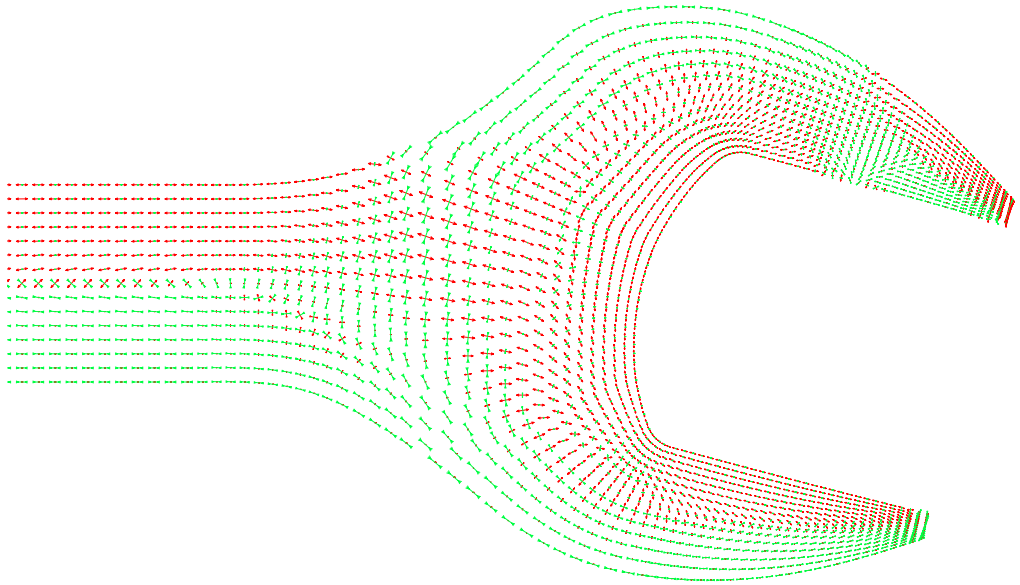

Figure 10.19: *Principal stresses of the spanner-head. Red arrows indicate tension and green arrows indicate compression. The contours of the elements are omitted to make the small arrows clearer.*

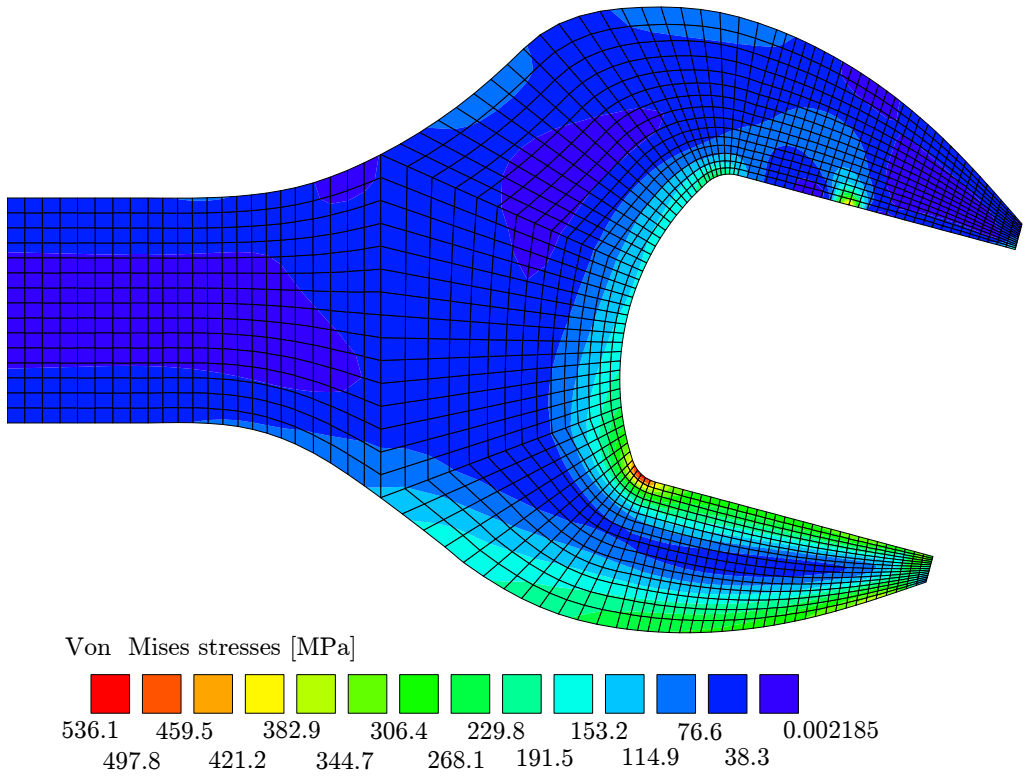

Figure 10.20: *Von Mises stresses in the spanner-head.*

Chapter

11

Validation of Finite Element Analysis

In the above chapters a total of four different methods have been applied to determine the strain level in the spanner model due to the subjected load. In accordance with the described design process in chapter 4, the results from the different methods are compared in the following. Thus determining if there exists a good coherence between the estimated and measured results, and ultimately determine the credibility of the FEA program.

11.1 Results Comparison

Below the results from the initial estimates, strain gauge measurement, digital image correlation, and finite element analysis are compared and interpreted. The locations used for the comparison are numbered according to the locations of the strain gauges as in section 10.9. In order to compare results from the different methods it is necessary to use the same units and coordinate system. In the results below the coordinate system shown in figure 8.10 was applied. Each result is displayed with an associated percentage deviation with regards to the strain gauge measurement for that particular location. The DIC measurements were made on the fork end of the spanner and are only represented in the position of SG11 and SG12. The stresses calculated for the shank and jaws in section 6.1 and 6.2 have been converted to strain using in Hooke's law for a plane stress situation (5.159). There are no estimates for location 11 and 12 due to no known solutions to the geometry of the area.

11.1.1 Locations 1 and 2

In position 1 and 2 the objective of the strain gauges was to detect if a normal force was present during the measurement. The results showed that a normal force was present. However, the magnitude could not be determined. In order to compare the results from the estimated calculations and FEA the same conditions have to be applied in all tests. Since the estimates and the FEA do not indicate a normal force, the strain gauge results were subtracted from each other and divided by two so that they only show pure bending strain. The result from the amplifier yielded strains of 290μ and -268μ for positions 1 and 2, respectively. As seen in table 11.1 the results obtained using beam theory can be considered identical to the measured values. Thus indicating that the strain gauges give reliable results. The small deviation of the FEA results is believed mainly to be a consequence of the fact that the strains are determined only in the centre of the elements.

Location	SG		FEA		Estimates
	ε/μ	$s(\varepsilon)$	ε/μ	$s(\varepsilon)$	ε/μ
1	279	1%	260	7%	281
2	-279	1%	-260	7%	-281
Average deviation:		**1%**		**7%**	

Table 11.1: *Locations one and two are situated* 150*mm from the plane end of the spanner.*

11.1.2 Location 3 and 4

The strain gauges in position 3 and 4 were set up in a half bridge to measure bending moment.

Location	SG		FEA		Estimates
	ε/μ	$s(\varepsilon)$	ε/μ	$s(\varepsilon)$	ε/μ
3	371	3%	330	8%	360
4	-371	3%	-329	8%	-360
Average deviation:		**3%**		**8%**	

Table 11.2: *Locations three and four are situated* 190*mm from the plane end of the spanner.*

The results shown in table 11.2 provide the same conclusion as with the comparison of location 1 and 2, which was expected due to the shank being dominated by bending.

11.1.3 Location 5

In position 5 the Poisson's effect is measured. The boundary conditions in the estimated calculation and the FE analysis prescribe the identical in-plane loading, and are thus expected to yield similar results on the shank.

Location	SG		FEA		Estimates
	ε/μ	$s(\varepsilon)$	ε/μ	$s(\varepsilon)$	ε/μ
5	93	3%	83	8%	90

Table 11.3: *Location 5 is situated* 170*mm from the plane end of the spanner.*

As seen from table 11.3 the results obtained by measurements and estimated calculations yield nearly identical results. This indicates that the strain gauge measurements were performed with a close to in-plane loading scenario.

From the preceding it can be seen that the strain gauge measurements of the shank are in good coherence with the results from Bernoulli-Euler theory. This accuracy of the strain gauge measurements is hereby assumed to be general for the entire spanner. Therefore, in the following the strain gauge results are used as point of reference for comparison.

11.1.4 Location 8, 9, and 10

Locations 8 and 10 are placed on the outer contour of the top and lower jaws, respectively. Location 9 is placed on the face of the lower jaw, tilted at an angle of 27° with respect to the contact surface of the jaw and nut. The estimated strains stem from the wedge calculations, where $\sigma_{x,2}$ has been used for the upper and lower jaws. In the wedge model shear strains are

present, however, they are neglected. The results obtained from the triangular beam model in section 6.2.1.5 showed that the shear stresses are of negligible magnitude. The results from the analytic calculations, strain gauge measurements, and FEA are shown as in the x_2 coordinate system, which is tilted -15° from the primary coordinate system. Note that for location 9 no estimates are available and the strain direction is the direction of SG9. Their values are listed for comparison in table 11.4.

Location	**Estimates**		**FEA**		**SG**	
	$\varepsilon\,/\,\mu$	$s(\varepsilon)$	$\varepsilon\,/\,\mu$	$s(\varepsilon)$	$\varepsilon\,/\,\mu$	Coord. syst.
8	-674	4%	-240	63%	-650	(x_2, y_2)
9	—	—	-1,131	18%	-962	SG
10	-1,359	8%	-946	25%	-1,262	(x_2, y_2)
Average deviation:		**6%**		**35%**		

Table 11.4: *Locations 8,9, and 10 on the jaws. The table showing ε_{x_2} strains.*

As can be seen from table 11.4 the results obtained from the strain gauges and the analytic calculations deviate by 4-8% for location 8 and 10. The analytic calculations were not expected to give such accurate results. Especially at location 8 where the wedge models are considered less accurate, which is described in section 6.2.2.

The results obtained from the FEA analysis have an average deviation of 35%, where the largest deviation of 63% is at location 8. The large deviation between the FEA model and the remaining results are assumed to be a consequence of the relative coarse mesh at the boundary, combined with the inaccuracy associated with the strain interpolation. Thus the accuracy of the strains may be less than expected. Due to these uncertainties, the results obtained via the FEA model at this location may not be comparable with the results from the measurements and estimates.

11.1.5 Location 11 and 12

For the centre area of the fork the strains have been determined using FEA, DIC, and strain gauge measurements. No estimated calculations have been performed due to the complexity of the region. In position 11 there are two measured components, strain in the x-direction (11^{0°) and strain in the y-direction (11^{90°). The strain gauges in positions (11^{90°) and 12 yield the strain from bending without any torque strain. The DIC results used for location 11 and 12 were determined by creating a virtual strain gauge during the post processing of the measurements. This was done by measuring the position of the real strain gauge and marking a circular area around the point, where the average horizontal and vertical strains were calculated. This is illustrated in figure 11.1.

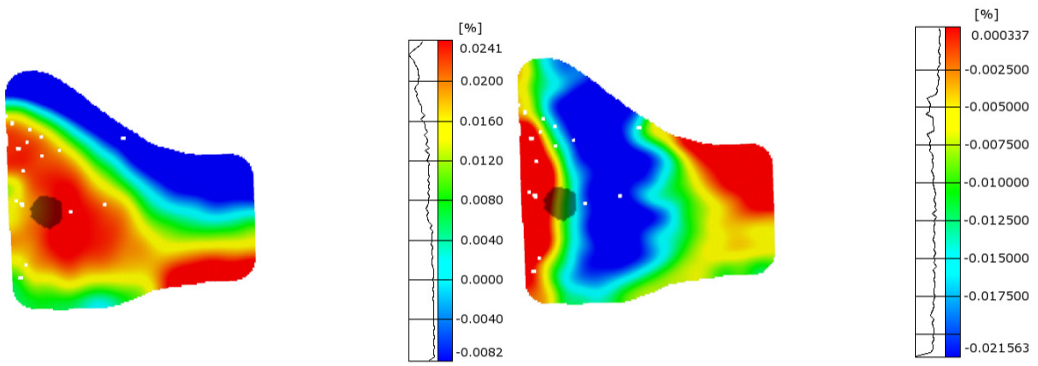

Figure 11.1: *A simple circular area was formed to serve as a virtual strain gauge, and average strains were calculated in horizontal direction (left) and vertical direction (right).*

Location	**DIC**		**FEA**		**SG**
	$\varepsilon\,/\mu$	$s(\varepsilon)$	$\varepsilon\,/\mu$	$s(\varepsilon)$	$\varepsilon\,/\mu$
11^{0°	223	4%	199	7%	215
11^{90° and 12	-67	7 %	-74	3%	-72
Average deviation :		**5%**		**5%**	

Table 11.5: *Locations 11 and 12 are situated* 225 *mm from the plane end of the spanner.*

The results for locations 11^{0°, 11^{90°, and 12 show good coherence between FEA calculations and DIC measurements. Due to poor distance measuring possibilities in ARAMIS, the results from these locations were initially considered to deviate more than shown in table 11.5.

11.2 Conclusions

Results from four different methods used to determine the strain levels in the spanner have been compared. The results show a good coherence at the selected locations. The complete list of locations and the different results are listed in table 11.6.

	1	2	3 and 4	5	8	9	10	11^{0°	11^{90° and 12
Strain gauge	279	−279	371	93	−650	−962	−1,262	215	−72
DIC	NA	NA	NA	NA	NA	NA	NA	223	−67
Estimate	281	−281	360	90	−674	− − −	−1,359	NA	NA
FEA	260	−260	330	83	−240	−1,131	−946	199	−74

Table 11.6: *Measurements used in the comparison. All results are in micro strain.*

In table 11.7 the average deviations from the different methods compared to the strain gauge results are listed. The table shows that results from the estimated calculations and DIC measurements are within an average limit of 6%. This proves the effectiveness of simple analytic calculations and the relatively new DIC method. However, it should be noted that results from the analytic calculation were not available at location 9. The average deviation of the finite element analysis reaches 16%. The explanation for this large deviation is unknown at present time. However, some possible contributory factors are the friction in the strain gauge elements and the boundary conditions of the upper jaw in the FEA.

In table 11.8 are shown the deviations of the different methods from the finite element analysis. Excluding the results obtained by FEA at location 8 reduces the average deviation to 27% for the solution from theory of elasticity and 8% for the solution from Bernoulli-Euler Beam Theory. Since DIC and strain gauges deviate 12% and 15%, respectively, the deviation of 27% is not believed to compromise the credibility of the finite element analysis. Furthermore, a deviation of 8% compared to the solution from Bernoulli-Euler theory substantiates the validity of the finite element analysis. For this reason an average deviation of 12% is believed to be representative for the finite element programs accuracy. This is supported by the programs ability to determine displacements with good accuracy compared to ANSYS using Q8 elements.

	B.E.	**T.E.**	**DIC**	**FEA**
Average deviation from SG results:	2%	6%	5%	16%

Table 11.7: *The average deviation from strain gauge results. B.E. is short for Bernoulli-Euler and T.E. is short for Theory of Elasticity.*

Excluding the results from location 8 from the comparison, the average deviations of the four methods compared to the results from the finite element analysis are listed in table 11.8.

	Strain gauge	**DIC**	**B.E.**	**T.E.**
Average deviation from FEA results:	12%	15%	8%	27%

Table 11.8: *The average deviation from FEA excluding results from location 8. B.E. is short for Bernoulli-Euler and T.E. is short for Theory of Elasticity.*

As seen from table 11.8 the strain gauges, DIC and the estimates yield very similar results. The results provided from the different methods are for three reasons considered to be highly satisfying:

- There has been used four different methods to measure or calculate strains in the spanner model. The measurements have been executed as thoroughly as possible, and the necessary simplifications in the calculations have been chosen carefully. The consequence of this is an average deviation of 9% compared to the strain gauge measurements.
- Results from the DIC and strain gauge measurements deviate on average from FEA by 12%.
- The DIC results from section 9.2 do not supply any direct numerical comparisons, but distribution of strains. As concluded they have got substantial equality. In addition, this chapter has presented numerical comparisons for location 11 and 12 to support the conclusion.

Based on the three points above, and provided that the actual deviation of the FEA is kept in mind, the combined results from the four methods are considered as a solid validation for the finite element analysis.

Chapter

12

Intuitive Optimisation of the Spanner

As stated in chapter 4 the last part of the design process is to optimise the spanner with respect to weight by use of the developed FEA-program DMS7FEA. By the end of the optimisation process a new model of the spanner, which utilises the material better, will be given. Furthermore this new model must meet the requirements set in chapter 3.

The optimisation process is carried out in the following two steps:

1. Optimise the geometry by moving around material in order to give a higher strength per unit material. This analysis is performed with an applied load of $100N$ as all preceding work.

2. When an improved geometry has been obtained, this geometry has to be dimensioned in order to meet the requirements from the thesis statement. In this part the applied load is raised to $1231.5N$, corresponding to a moment of $287Nm$ as stated in the thesis statement.

It is important to notice that the optimisation process is carried out by *intuitive optimisation* of the current model. In this process the geometry is changed based on intuition stemming from the examination of relevant plots. Thus the optimisation process is based on common sense of mechanics rather than a computers ability to determine optima by calculations. Hence the final model will not be *the most optimal* model, but rather a *better* model than the current.
The two optimisation steps is described in chronological order in the following.

12.1 Step 1: Optimisation of the Geometry

In order to succeed a optimisation process, the objectives of the process must be clarified before the process is started. For the optimisation process the following objectives have been formulated:

1. Remove poorly utilised material from the model without raising the largest von Mises stress found in the model.

2. Put on extra material in order to strengthen the model in appropriate areas.

As these objectives are not contradictory they can be carried out one at a time without problems. In the current optimisation process the two objectives are carried out chronologically. This iterative process is performed in coherence with assessment of the strain energy density and the principal stresses and their directions.

In order to realise which material is poorly exploited the strain energy density can be used. The average strain energy density for an element is calculated in DMS7FEA as

$$u_e = \frac{U_e}{V_e} = \frac{\frac{1}{2}\int_{V_e} \vec{\sigma}^T \vec{\varepsilon} dV}{V_e} = \frac{\frac{1}{2}\vec{d}^T \bar{\bar{k}} \vec{d}}{V_e} \tag{12.1}$$

where:

u_e	The average strain energy density of an element.
U_e	The strain energy of an element.
V_e	The volume of the element.
$\vec{d}$	The element displacement vector.
$\bar{\bar{k}}$	The element stiffness matrix.

The average strain energy density along with the principal stress directions give a good foundation for judging whether the design of a structure is good.
In order to fulfil the objectives of the optimisation process a few iterations are made, where for each iteration the average strain energy densities along with the principal stress directions are plotted and on this basis the geometry is changed. Plots of the average strain energy densities and the principal stress directions for the iterations are given in table 12.1 with a few comments for each design. The mesh used for the optimisation is a default mesh from ANSYS and is not modified to reduce distorted elements.

Table 12.1: *Iterations of the process of optimising the geometry of the spanner.*

Iteration No.	
0	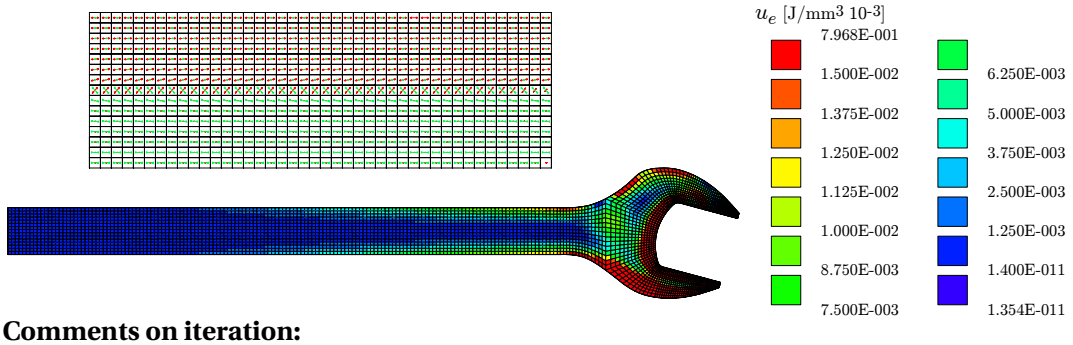 **Comments on iteration:** This is the basis of the optimisation process. It is seen from the strain energy densities that the material in the shank is poorer utilised than the material in the head of the spanner. Furthermore the principal stress directions show that the shank (as known) primarily is subjected to bending. Hence a next iteration could be to remove material from the centerline of the shank.

Continued on next page.

Table 12.1 – Continued from previous page

Iteration No.	
1	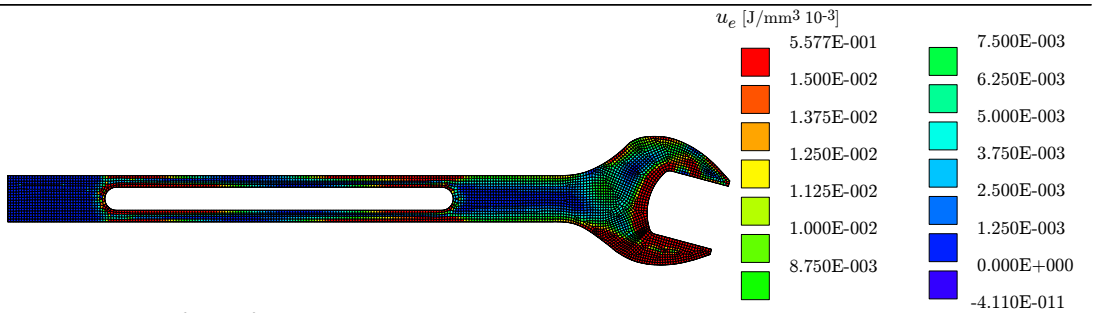 **Comments on iteration:** A big hole has been made in the middle of the shank. This has reduced the total weight of the spanner without causing problems. However, it is seen that there is still poorly utilised areas in the shank meaning that even more material can be removed.
2	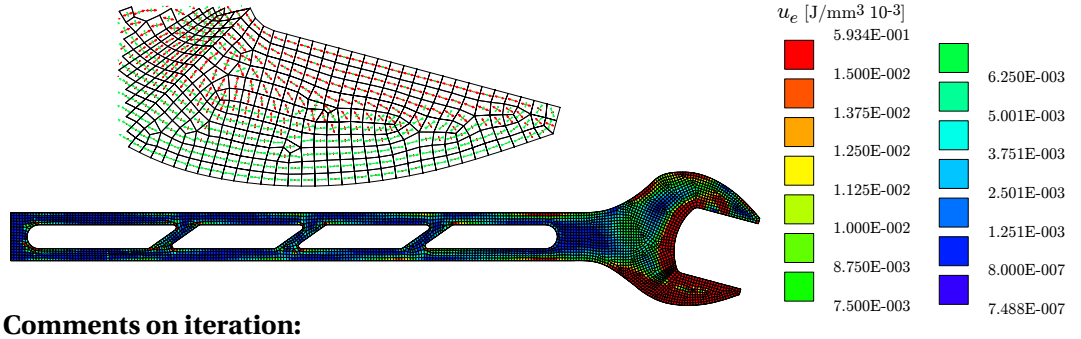 **Comments on iteration:** Most of the material in the centre of the shank has been removed. Only small bars of material is left between the top and the bottom of the shank to prevent the shank from collapsing. It should be noted that the 45°-angle of these bars is only present for esthetic reasons. It is not believed to have any positive effects on the structure. It is seen on the plots that the lower jaw is mainly loaded in bending. Furthermore corners inside the fork are highly loaded due to the stress concentrations. From this it is decided to enhance the jaws ability to carry bending by broadening them and to round the corners inside the fork. Furthermore the neck of the spanner is broadened while the hole in the centre of the shank is extended a little. Thus this next iteration is a combination of these two improvements.
3	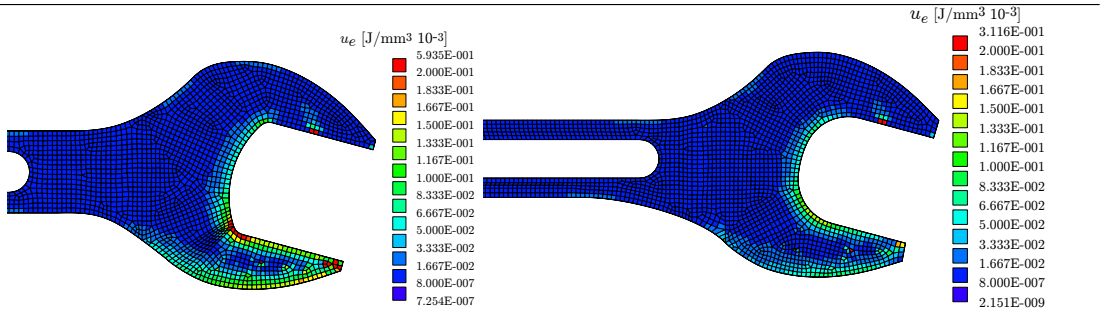

Continued on next page.

Table 12.1 – Continued from previous page

Iteration No.	
	Comments on iteration: The illustration shows the improvement of the spanner head in the third iteration. The one at the right is the new iteration. It is seen that as desired the strain energy density is more uniformly distributed. However, there is still a tendency that the material in the head is more utilised than the material in the shank. To reduce this effect it is desired to raise the thickness of the head. As the FEA-program DMS7FEA only operates with 2D-structures it is not possible to implement this completely. However, a slightly primitive solution has been found. The element thickness is simply raised for entire elements in elected regions of the spanner. The results of this approach are believed to be good for most of the structure. Only near the transition from one thickness to another the results are assumed to be misleading.
4	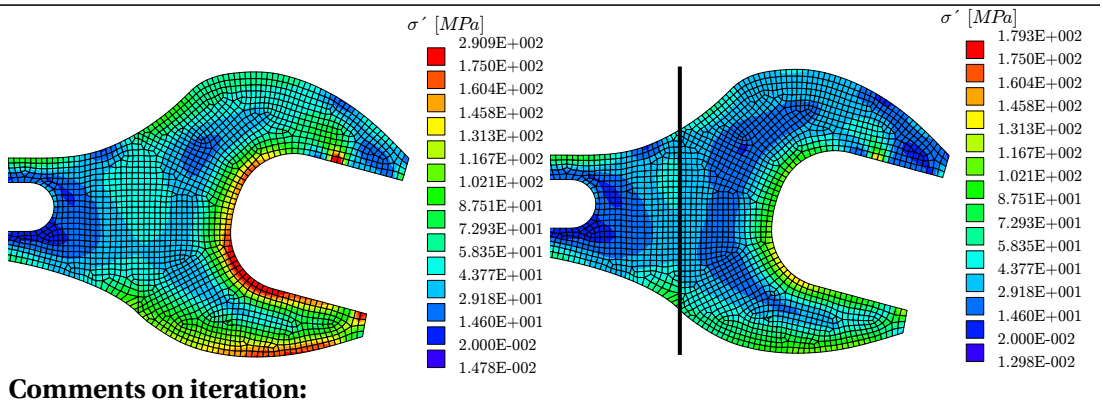 **Comments on iteration:** In this iteration the thickness of the head i set to $8mm$, whereas the thickness of the shank is still $5mm$. The left image shows the von Mises stresses in the previous iteration and the right image shows the von Mises stresses in the current iteration including a black line indicating where the thickness changes.

The design of iteration 4 is believed to be a better design than the original. Aided by the CAD-program used to draw the models, the volume of the original- and the new design can be determined to be

$$V_{original} = A_{original}\, t_{uniform} \tag{12.2}$$
$$= 4937.71mm^2 \cdot 5mm \tag{12.3}$$
$$= 24689mm^3 \tag{12.4}$$
$$V_{new} = A_{new,shank}\, t_{shank} + A_{new,head}\, t_{head} \tag{12.5}$$
$$= 2374.49mm^2 \cdot 5mm + 1286.35mm^2 \cdot 8mm \tag{12.6}$$
$$= 22163mm^3 \tag{12.7}$$

Thereby, it is seen that the new design uses less material than the old design, even though it shows a higher strength at the given loading scenario.

12.2 Step 2: Dimensioning the Optimised Geometry

Though the new spanner geometry provides a higher strength than the original, it is still not strong enough to meet the requirements set by the standard. According to the standard the

spanner must be able to withstand a moment of $287Nm$—corresponding to a force at point A of $1231.5N$—without showing significant deformations as described in the thesis statement. If this high load is applied to the spanner developed in the prior section yielding will occur in large parts of the head and the spanner will deform too much to meet the requirements. The exact yield strength of the produced spanner model is not known, but it is needed to strengthen the spanner further. This is done by raising the thickness in both regions. After some iterations it is reached that the spanner must have a thickness of $8mm$ in the shank and $12mm$ in the head. A plot of the von Mises stresses in this new spanner is shown in figure 12.1. It is seen that the most stressed area is still the lower jaw. If less than half the cross section of the lower jaw is allowed to yield the material of a new spanner would need to have a yield strength of around $400MPa$.

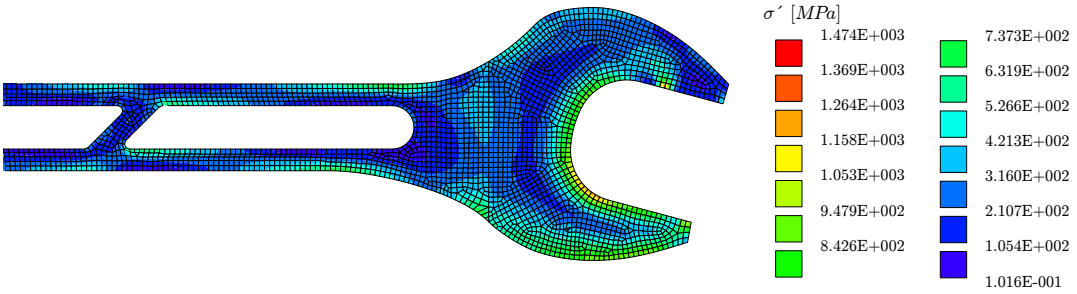

Figure 12.1: *The von Mises stresses in the new spanner design at a load of* $1231.5N$.

Some dimensions of the spanner are given in table 12.2 in order to document that the new spanner is kept within the requirements.

	$l\,/mm$	α	$a_2\,/mm$	$b_2\,/mm$
Required by standard:	min. 265	15°	max. 12	max. 56
Actual:	266	15°	12	49.8

Table 12.2: *Dimensions of the new spanner.*

As stated in the thesis statement the maximum deformation requirements for the spanner are:

1. The distance between the jaws two centre points, S_d, exceeds the tolerance limit of $24.36\,mm$.

2. The angel α between the shank and fork centerlines changes more than 1°.

Whether the new spanner design meets these two deformation requirements is documented by calculating the displacements at points S_1 and S_2 seen in figure 12.2.

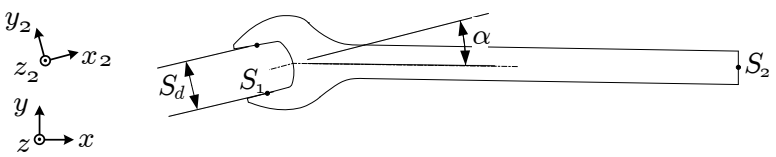

Figure 12.2: *Point* S_1 *and* S_2 *used for checking that the new model fulfils the requirements from the thesis statement.*

Because of the boundary conditions described in section 10.8.2 the fulfilment of requirement 1 can be checked simply by the displacement of point S_1 in the y_2-direction as this must not exceed $0.36mm$. The displacements in the x, y-coordinate system is found by use of the DMS7FEA and the displacement in the y_2-direction is calculated to be

$$u_{y_2} = u_x(S_1)\sin(15^\circ) + u_y(S_1)\cos(15^\circ) \tag{12.8}$$
$$= 0.15mm \cdot \sin(15^\circ) + 0.33mm \cdot \cos(15^\circ) \tag{12.9}$$
$$= 0.36mm \tag{12.10}$$

which is seen to fulfil the requirement.
The fulfilment of requirement 2 is checked by the displacement of point S_2 as the change in the angle α is simply determined from the vertical displacement of S_2. Hence the change in α is:

$$\Delta\alpha = \sin^{-1}\left(\frac{u_y(S_2)}{|OS_2|_x}\right) \tag{12.11}$$
$$= \sin^{-1}\left(\frac{3.90mm}{233mm}\right) \tag{12.12}$$
$$= 0.95^\circ \tag{12.13}$$

where: $|OS_2|_x$ The horizontal distance from the centre of the nut to point S_2.

Again the requirement is met.
Hence it can be concluded that the new design fulfils the requirements setup in the thesis statement.
In chapter 11 it was concluded that DMS7FEA deviates with about 12% of the actual strains. If this is to be accounted for in the optimisation process an iteration more is needed.

Chapter

13

Conclusions

In this project a spanner has been modelled and subjected to experimental, analytical and approximative methods to obtain the stress- and deformation situation. The objective of determining a design which satisfies quantitative requirements concerning the deformation of the geometry. The analytical methods consist of classic Bernoulli-Euler beam theory and selected solutions from the theory of elasticity. The experimental methods which have been used are the well proven strain gauge measurements and the relatively new method digital image correlation. For the approximative computation a finite element analysis program has been developed.

The estimates have been used to identify areas of interest for the experiments and to verify the results where the estimates were considered to be less accurate. The estimates also provided specific locations where the strain condition could be considered well known. Thus strain gauges were placed on these locations so as to verify the loading condition. During the strain gauge measurements a large normal force was registered. The reason for the registered force is unknown, but believed to be a systematic error. Redoing the strain gauge measurements can possibly eliminate this error.

The choice of integration method used in the finite element program was based on accuracy of calculated displacements, due to the requirements from the thesis statement concerning the amplitude of deformation. Here reduced integration with hourglass control provided the most accurate displacements.

Comparing the results from the different methods showed an average deviation of 7% with respect to the strain gauge measurements. Thus displaying a close coherence between the different methods. On this basis the finite element program has been verified with an average deviation of 12% with respect to the measured results. At location 8 the finite element analysis showed a deviation of 63% with respect to the measured strain gauge value. The reason for this large deviation is currently unknown.

The deviations of DIC from the strain gauge measurements and finite element analysis of 5% and 15% respectively, are based on only two measuring points. This does not do justice to the accuracy and usefulness of this method. In section 9.2 it was shown that the method provided a complete strain field description of the area captured in the image. The strain field was proven to give satisfying results for the finite area and thus supplementing the FE method for finding complete strain fields in complex areas where analytical methods can not be applied. It has not been examined which strain magnitudes that give good results in DIC. However, it is expected that the method gives the best results for large strains. This quantification should be done in

order to evaluate the applicability of the DIC results in this project.

The geometry of the spanner model has been changed by means of intuitive optimisation. Here a volume reduction of 10 % was achieved while increasing the strength of the spanner model. Increasing the load while satisfying the limits of deformation in coherence with the thesis statement resulted in a volume increase of 55 %. The optimised model is restricted by the material's yield strength, which needs to be 400 MPa in order to keep half of the cross section in the lower jaw below the yield limit. It is acknowledged that the choice of material is a main design objective, if the spanner was to be manufactured and put to actual use. However, it has been beyond the scope of this project.

Throughout the stress and deformation analysis of the spanner, it has been proven that it is possible to determine stress conditions using a variety of approaches. They range from classic Bernoulli-Euler beam theory to the more comprehensive finite element method. Based on the results it is concluded that even simple estimate calculations can provide highly accurate results. This project has shown that the finite element analysis is a powerful method for determining the complete stress- and strain field in a structure, but must be used with vigilance, general insight, and understanding of mechanics. The finite element method is a powerful tool in combination with analytical calculations, DIC and strain gauge measurements.

Bibliography

[1] Schneider S. DIN-VDE-Taschenbuch. 10th ed. VDE Verlag; 2009.

[2] Arne Kildegaard JS. Elasticitetsteori. 4th ed. Stegmann J, editor. Pontoppidanstræde 101, 9220 Aalborg Ø, Danmark: Institut for Maskinteknik, Aalborg Universitet; 2006.

[3] Irving H Shames FAC. Elastic and Inelastic Stress Analysis. Revised printing ed. Taylor & Francis Inc; 1997. ISBN: 9781560326861.

[4] Olhoff N. Noter til styrkelære II. 1st ed. Nils Koppels Allé 404, 2800 Kgs. Lyngby: Afdeling for faststofmekanik, Danmarks Tekniske Højskole;.

[5] Ansel C Ugural SKF. Advanved Strength and Applied Elasticity. 4th ed. Donovan P, editor. Upper Saddle River, New Jersey 07458, United States of America: Prentice Hall; 2003. ISBN: 0130473928.

[6] Gere JM. Mechanics of Materials. 6th ed. Thomson Canada Limited; 2006. ISBN: 0495073075.

[7] Irving H Shames CLD. Energy and Finite Element Methods in Structural Mechanics. Revised edition ed. Taylor & Francis Inc; 2003. ISBN: 0891169423.

[8] Hoffmann K. An Introduction to Measurements using Strain Gauges. Hottinger Baldwin Messtechnik GmbH, Darmstadt; 1989.

[9] Mouritsen OØ. Lectures on strain gauges;. Autumn 2009.

[10] Instruments N. Measuring Strain with Strain Gages;. http://zone.ni.com/devzone/cda/tut/p/id/3642. Visited on November 12th 2009.

[11] Standard D. Trækprøvning DS10110 D. 1st ed. Dansk Standard; 1949.

[12] Mouritsen OØ. Grundlæggende usikkerhedsvurdering ved måling med strain gages; 2009. Pdf-file.

[13] Sutton MA, Wolters WJ, Peters WH, Ranson WF, McNeill SR. Determination of Displacements Using an Improved Digital Image Correlation Method. Image and Vision Computing. 1983;1(3):133–139.

[14] Chu TC, Ranson WF, Sutton MA, Peters WH. Applications of Digital-Image-Correlation Techniques to Experimental Mechanics. Experimental Mechanics. 1985 September;p. 232–244.

[15] Sutton MA, et al. Image Correlation for Shape, Motion and Deformation Measurements: Basic Concepts, Theory and Applications. Springer Science + Business Media LLC; 2009.

[16] Robert D Cook MEPRJW David S Malkus. Concepts and Applications of Finite Element Analysis. 4th ed. Anderson W, editor. 111 River Street, Hoboken, NJ 07030: John Wiley & Sons, INC; 2002. ISBN: 9780471356059.

[17] Olhoff N. 2. Optimization using Calculus of Variations;. Notes for Ph.D. Course on Advanced Optimization.

[18] Mouritsen OØ. Note vedrørende beregning af stivhedsmatrice for plant 4-knuders isoparametrisk element;. http://www.me.aau.dk/intranet/lecture_notes.

[19] Lund E. Lecture notes for Finite Element Methods 3 (2009);. http://www.ime.aau.dk/notes/el/FEM3/FEM3.htm.

Nomenclature

Latin Letters

a_i	The generalised d.o.f. or generalised coordinates.
$\bar{\bar{A}}$	Matrix containing nodal coordinates.
$\bar{\bar{A}}(\vec{x})$	The digital form of the scalar intensity field of the deformed image.
A	Area.
b	Height of the spanner.
b	Width.
$\bar{\bar{B}}$	The strain-displacement matrix.
B_j	The body force.
C_r	The length of the polar cross section line at radius r.
$\vec{d}$	The element displacement vector.
dh	The perpendicular height from the surface abc to point P.
ds	Length of vector dx_i in the undeformed body.
ds^*	Length of vector dx_i^* in the deformed body.
$\vec{d}_u$	The displacement vector for $\bar{u}$ in the x-direction.
$\vec{d}_{xi}$	Displacement vector for mode i.
dx_k	The length, width, or height of the infinitesimal parallelepiped.
$\vec{D}$	Displacements due to the external applied force(s).
e	The alternating symbol.
E	Young's modulus.
$\bar{\bar{E}}$	The constitutive matrix.
f_i	The function used to approximate the displacement field.
$\vec{F}$	Body forces applied to the elastic body.
h	Height.
I	The moment of inertia.
$\bar{\bar{J}}$	Jacobian matrix.
$\|J\|$	Determinant of the Jacobian matrix.
$\bar{\bar{k}}$	The element stiffness matrix.

$\bar{\bar{K}}$	Global stiffness matrix.
K_i	Resultant force vector.
l	Length.
M	Moment.
n	Number of nodes in the element.
n	The number of samples.
n_i	ith component of the unit normal vector n.
n_j	jth component of the unit normal vector n.
$\bar{\bar{N}}$	Interpolation functions.
p_i	Volume load.
$\vec{P}$	The external applied force(s).
Q	The moment area.
Q_i	System of loads at point i.
r	The ξ coordinate to the Gauss point.
$\vec{r}_{ei}$	The force vector containing body forces and surface tractions.
R	Electrical resistance.
$\vec{R}$	The global force vector containing applied loads $\vec{P}$ and element load vectors $\vec{r}_{ei}$.
R_0	Initial resistance.
R_0	Reaction force at x equal to zero.
s	The η coordinate to the Gauss point.
s	The sample standard deviation.
s_r	The relative uncertainty.
$\frac{s}{\bar{\varepsilon}}$	Relative uncertainty.
t	Thickness.
T_i	Traction vector.
$\overset{j}{T}_i$	Traction on surface with unit normal n_j.
u	The displacement field in the x-direction.
U^*	Total complementary energy.
U_e	The strain energy of an element.
U_0	The strain energy density.
v	The displacement field in the y-direction.
V_e	The volume of the element.

V_o	Output voltage.
V_s	Supply voltage.
V_t	The internal shear force due to the transverse loading.
w	The displacement field in the z-direction.
w	Width of the spanner.
$\vec{x}^*$	The deformed position vector.
x_i	x-coordinate for node i.
$X_{dataset}$	The values measured and recorded in the experiment.
X_{line}	The values from the linear data fit.
y_i	y-coordinate for node i.
$\frac{\partial(u_i(\vec{x}))}{\partial x_j}$	The deformation gradient at point $\vec{x}$.

Greek Letters

α	Tilted angle of strain gauge.
$\tilde{\alpha_i}$	Estimated error due to angular misplacement for strain gauge i.
γ_{xy,M_x^*}	The engineering shear strain due to the torsional moment M_x^*.
ΔM	subset in deformed image.
ΔV	Volume element subjected to volume load.
ε	Strain.
λ	Lagrange multiplier.
ν	Poisson's ratio.
ρ	Resistivity.
σ	Stress.
τ_{xy}	The shear stress in the shank due to torsion.
$\vec{\Phi}$	Surface tractions applied to the body.
$\vec{\Phi}_e$	Nodal displacement vector.
Ω	Total potential of applied loads.

Appendix

A

Location of Strain Gauges

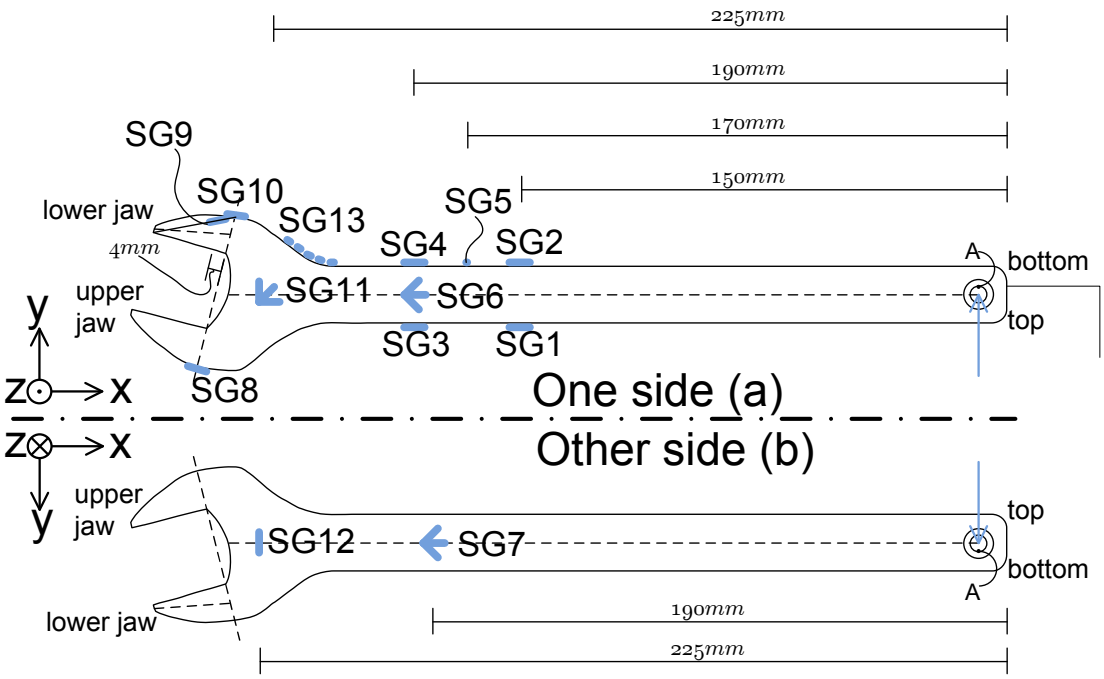

Figure A.1: *The locations of the strain gauges are also explained below.*

SG1**, SG**2**:** 150mm from the plain end.

SG5**:** 170mm from the plain end.

SG3**, SG**4**, SG**6**, SG**7**:** 190mm from the plain end.

SG11**, SG**12**:** 225mm from the plain edge.

SG8**, SG**10**:** There has been drawn a straight line through the inner ends of the jaws where the straight edges end. The strain gauges has been mounted at each end of the line on the top and bottom of the spanner, respectively.

SG9**:** On the lower jaw, a straight line has been drawn from the outer corner point of the grip edge to the mounting point for SG10. SG9 has been mounted on that line with a distance of four millimeters measured perpendicular to the line drawn for SG8 and SG10.

Appendix

B

Spanner Overview

Til Dobbeltside

Appendix

C

Appendix CD-ROM